Doctoral Thesis

Computational Modeling of Transient Multi-Phase Flow in the Nozzle and Mold of Continuous Steel Slab Casting with Electro-Magnetic Braking (EMBr)

Seong-Mook Cho

Department of Materials Science and Engineering

Pohang University of Science and Technology

2014

Acknowledgements

I respectfully express great gratitude to my advisers, Prof. Seon-Hyo Kim and Prof. Brian G. Thomas for their continuous guidance on the thesis research during my doctoral study. I also appreciate Prof. Seon-Hyo Kim, Prof. Brian G. Thomas, Prof. Sang-Joon Kim, Prof. Jung-Wook Cho, and Dr. Joong-Kil Park for the thesis evaluation.

I would like to thank Dr. Ho-Jung Shin for discussing about the plant measurements and inspiring me to do the thesis research.

The author thanks POSCO for their assistance in collecting plant data and financial support, and Mr. Yong-Jin Kim, POSCO for help with the plant measurements. Support from the National Science Foundation (Grant No. CMMI 11-30882) and the Continuous Casting Consortium, University of Illinois at Urbana-Champaign, USA is also acknowledged.

Special thanks to my senior and fellow researchers at the Clean Steel & Non-Ferrous Metals Processing Laboratory, POSTECH (Dr. Jeong-Do Seo, Dr. Sung-Koo Jo, Dr. Ho-Jung Shin, Dr. Sun-Hong Park, Dr. Min-Oh Suk, Dr. Go-Gi Lee, Dr. Soo-Young Seo, Dr. Chang-Woo Seo, Dr. Chang-Ha Kwak, Yong-Byung Lee, Hyun-Chul Kim, Jun-Sung Park, Hyun-Na Bae, Hyoung-Jun Lee, See-Yeong Park, Myung-Duk Seo, Dae-Woo Yoon, and Seung-Ho Shin) and at the Metals Processing Simulation Laboratory, UIUC (Dr. Rajneesh Chaudhary, Rui Liu, A.S.M. Jonayat, Lance Hibbeler,

Dr. Kun Xu, Matthew Zappulla, Ramnik Singh, Prathiba Duvvuri, Aravind Murali, Bryan Petrus, Kai Jin, Yonghui Li, and Hyun-Jin Yang) for making my work enjoyable.

I would also like to thank my friends (Dr. Ji-Yong Park, Sung-Ki Lee, Dr. Ah-Young Ji, and Jong-Lo Park) for making my stay at UIUC memorable.

Most of all, I sincerely thank my family, especially my parents and brothers. Without their continuous support and encouragement, this work would not have been possible.

ABSTRACT

This thesis develops computational model of transient multi-phase fluid flow with static magnetic field using Large Eddy Simulation (LES) model coupled with Lagrangian Discrete Phase Model (DPM) and Magneto-Hydro-Dynamics (MHD) equations to quantify the transient two-phase (molten steel-argon gas) flow in the nozzle and mold of continuous steel slab casting with double-ruler Electro-Magnetic Braking (EMBr). The two-phase model is validated by performing plant measurements which visualize and quantify the transient fluid flow phenomena at the surface in the mold during the nominally steady-state casting. The validated model is then used to analyze time-averaged and time-dependent two-phase flow structure in the nozzle and mold with and without EMBr.

A mean bubble size of argon gas in molten steel pool is first calculated for the Lagrangian DPM using the two-stage analytical model of bubble formation by Bai and Thomas and the empirical model of the active site at the refractory of an Upper Tundish Nozzle (UTN) by Lee et al. An average bubble size was determined by coupling these two models and extrapolating the air-water results to the real caster involving argon and molten steel.

The calculated mean bubble size of argon gas is then used for computational modeling of transient two-phase flow in the nozzle and mold during nominally steady-state casting conditions using LES coupled with the DPM. The predicted flow field is validated with the measured one at the surface in the mold by a nail board dipping test

which quantifies surface level, surface velocity, flow direction, and slag depth at different times. The surface level of the molten steel fluctuates due to sloshing and shows greater fluctuations near the nozzle. The slag level fluctuates with time according to the lifting force of the molten steel motion below. Surface flow shows a classic double roll pattern, with transient cross-flow between the Inside Radius (IR) and the Outside Radius (OR), and varies with fluctuations up to ~50% of the average velocity magnitude. The LES results suggest that these transient phenomena at the surface are induced by up-and-down jet wobbling caused by a transient swirl in the slide-gate nozzle. The jet wobbling influences the transient argon gas distribution and the location of jet impingement on the Narrow Face (NF), resulting in variations in surface level and velocity. A power-spectrum analysis of the predicted jet velocity reveals strong peaks at several characteristic frequencies from 0.5-2 Hz (0.5-2 sec).

Afterwards, plant measurements and computational models of transient flow, with and without electromagnetic fields, are applied to investigate the effect of double-ruler EMBr on transient phenomena in the nozzle and mold region during nominally-steady steel slab casting. The effect of applying a static magnetic field on stabilizing the transient flow is investigated by modeling a double-ruler EMBr system, under the conditions where measurements were obtained. A Reynolds Averaged Navier-Stokes (RANS) computational model, using the standard $k-\varepsilon$ model, is employed with a magnetic field distribution extrapolated from measurements. The magnetic field decreases velocity fluctuations and deflects the jet flow downward in the mold, resulting in a flatter surface level and slower surface flow, with slightly better stability. The effect of EMBr on the surface level and surface velocity, including the effect of

the real conducting steel shell, falls between the cases, assuming perfectly-conducting and insulating walls. Measurements using an eddy current sensor and nail boards were performed to quantify the effect of EMBr on the level and velocity at the mold surface. Power spectrum analysis of the surface level variations measured by the sensor revealed a frequency peak at ~0.03 Hz (~35 seconds), both with and without the EMBr. With EMBr, the surface level is more stable, with lower amplitude fluctuations, and higher frequency sloshing. The EMBr also produces ~20 % lower surface velocity, with ~60 % less velocity variations. The motion of the slag-steel interface level causes mainly lifting rather than displacement of the molten slag layer near the SEN.

Transient two-phase fluid flow with double-ruler EMBr is then modeled using the LES model coupled with both the DPM and MHD equations. Two cases, including two-phase flow with and without EMBr, are calculated and compared to quantify the effect of EMBr on transient molten steel-argon gas flow. The model shows very good agreement of time-averaged surface velocity, surface level, and their fluctuations with the measurements obtained with the nail board dipping test. This confirms that the model can capture and predict transient flow phenomena in the nozzle and mold of a real caster. The validated model allows quantitation of the transient molten steel-argon gas flow phenomena influenced by EMBr by analyzing time-averaged and time-dependent results in the nozzle and mold; these could not be visualized by the plant measurements. The mean and instantaneous flow field, turbulent kinetic energy, and Root Mean Square (RMS) velocity fluctuations in the nozzle and mold are quantified. Molten steel-argon gas flow shows high turbulent kinetic energy, which induces higher velocity fluctuation along the casting direction,

in the nozzle bottom region. The jet flow of steel-argon gas in the mold shows high velocity fluctuation with high frequency in all directions at the surface. On the other hand, smaller velocity fluctuation with lower frequency appears in the deep region of the mold. The EMBr effects on the two-phase flows deflect the jet flow downward, deep into the mold cavity, with smaller velocity fluctuation, resulting in a slower surface flow with higher stability in all directions. Argon gas distribution is also affected by the EMBr. Without EMBr, most argon bubbles float up to the surface by upper-recirculation flow. However, the jet flow deflected downward by the EMBr maintains many of these bubbles in the region 600~1200 mm from the mold top, and near the NF.

Table of Contents

List of Tables

List of Figures

Chapter 1: Introduction

1.1. Transient Fluid Flow Phenomena in Continuous Casting of Steel Slab

1.2. Objectives and Contributions of the Current Work

1.3. Tables and Figures

1.4. References

Chapter 2: Calculation of the Initial Bubble Size of Argon Gas in the Nozzle of Continuous Steel Slab Casting

2.1. Introduction

2.2. Bubble Volume Flow Rate

2.3. Bubble Active Site Model

2.4. Bubble Formation Model

2.5. Initial Bubble Size in Slide-Gate System of Continuous Casting

2.6. Initial Bubble Size in Stopper-Rod System of 1/3 Scale Water Model of Continuous Casting

2.7. Summary and Conclusions

2.8. Tables and Figures

2.9. References

Chapter 3: Modeling of Transient Two-Phase Fluid Flow in the Nozzle and Mold of Continuous Steel Slab Casting & Plant Measurements

3.1. Introduction

3.2. Plant Experiments

3.3. Plant Measurement Results

3.4. Computational Models

3.5. Model Results and Discussion

3.6. Summary and Conclusions

3.7. Table and Figures

3.8. References

Chapter 4: Effect of Double-Ruler Electro-Magnetic Braking (EMBr) on Transient Fluid Flow in the Nozzle and Mold of Continuous Steel Slab Casting

4.1. Introduction

4.2. External Magnetic Field Distribution

4.3. Computational Model

4.4. Model Results

4.5. Model Validation

4.6. Measurement Results

4.7. Summary and Conclusions

4.8. Table and Figures

4.9. References

Chapter 5: Modeling of Transient Two-Phase Fluid Flow in the Nozzle and Mold of Continuous Steel Slab Casting with Electro-Magnetic Braking (EMBr)

5.1. Introduction

5.2. Plant Measurements

5.3. Computational Model

5.4. Model Validation

5.5. Time-Averaged Results

5.6. Transient Results

5.7. Summary and Conclusions

5.8. Tables and Figures

5.9. References

Chapter 6: Conclusions and Future Scope

6.1. Calculation of the Initial Bubble Size of Argon Gas in the Nozzle of Continuous Steel Slab Casting

6.2. Modeling of Transient Two-Phase Fluid Flow in the Nozzle and Mold of Continuous Steel Slab Casting & Plant Measurements

6.3. Effect of Double-Ruler Electro-Magnetic Braking (EMBr) on Transient Fluid Flow in the Nozzle and Mold of Continuous Steel Slab Casting

6.4. Modeling of Transient Two-Phase Fluid Flow in the Nozzle and Mold of Continuous Steel Slab Casting with Electro-Magnetic Braking (EMBr) & Model Validation

6.5. Overall Conclusions

6.6. Future Scope

List of Tables

Table 2.1. Conditions of argon gas injection

Table 2.2. Comparison of bubble size between prediction and measurement

Table 3.1. Caster dimensions and process conditions

Table 4.1. Process parameters

Table 5.1. Coefficient of slag motion at the surface regions without and with EMBr

List of Figures

Fig. 1.1. Flow phenomena in the mold of steel slab continuous caster

Fig.2.1. Schematic of continuous caster with slide-gate system

Fig.2.2. UTN refractory [ref.18]: (a) pores, (b) surface coating layer, and (c) chemical experiment of the coating layer

Fig.2.3. Extrapolating graph of the number of active sites [ref.18]

Fig.2.4. Schematic of initial bubble formation: (a) expansion stage and (b) elongation stage

Fig.2.5. Schematic of 1/3 Scale Water Model

Fig.2.6. Geometry of Stopper-rod in the Water Model

Fig.2.7. Snapshot of Initial Bubble Behavior at Stopper-rod Tip

Fig.2.8. Relation between Argon Gas Volume Flow Rate and Bubbling Frequency

Fig.2.9. Relation between Argon Gas Volume Flow Rate and Bubble Size

Fig. 3.1. (a) Schematic of slide-gate in steel slab continuous casting and (b) slide-gate middle plate on SEN

Fig. 3.2. Photos of the nail board: (a) top view, (c) front view and schematics of the nail board: (b) top view, (d) NF view

Fig.3.3. Nail board dipping method

Fig.3.4. Transient variations of surface level profile by the nail board measurements

Fig.3.5. (a)Time-averaged surface level and (b) surface level fluctuation by the nail board measurements

Fig. 3.6. Transient variations of surface flow pattern by the nail board measurements

Fig. 3.7. Averaged surface flow pattern by the nail board measurements

Fig. 3.8. (a) Time-averaged surface velocity and (b) surface velocity fluctuation by the nail board measurements

Fig.3.9. Steel shell thickness profile in the domain for the computational modeling

Fig.3.10. (a) Domain, (b) mesh for slide-gate, (c) mesh for nozzle port, (d) mesh for the mold and (e) center cross-section view of mesh of the computational modeling

Fig.3.11. Time-averaged and instantaneous velocity magnitude in the nozzle bottom

Fig.3.12. Time-averaged and instantaneous velocity magnitude in the mold

Fig.3.13. Instantaneous argon gas distributions in the mold

Fig.3.14. Time-averaged and instantaneous velocity magnitude at the surface

Fig.3.15. Location of points in the nozzle and mold center-middle plane

Fig.3.16. Transient velocity magnitude histories calculated (a) in the nozzle and (b) in the mold

Fig.3.17. Power spectra calculated (a) in the nozzle and (b) in the mold

Fig.3.18. Comparison of (a) surface level and (b) surface velocity between the computational modeling and the measurement

Fig.4.1. Position of eddy current sensor in the mold

Fig.4.2. External EMBr field: (a) locations measured, and (b) magnetic field profiles

Fig.4.3. External magnetic field magnitude distribution in the nozzle and mold

Fig.4.4. (a) Induced magnetic field, (b) current density, (c) electromagnetic force, and (d) electromagnetic force vector distributions in the nozzle

Fig.4.5. (a) Induced magnetic field, (b) current density, (c) electromagnetic field, and (d) electromagnetic force vector distributions in the mold

Fig.4.6. Predicted velocity magnitude in the nozzle (a) without EMBr and (b) with EMBr

Fig.4.7. Turbulent kinetic energy in the nozzle (a) without EMBr and (b) with EMBr

Fig.4.8. Predicted velocity magnitude on center-middle plane in the mold (a) without EMBr and (b) with EMBr including steel shell

Fig.4.9. Turbulent kinetic energy predicted in mold mid-plane (a) without EMBr and (b) with EMBr including steel shell

Fig.4.10. EMBR effect on (a) time-averaged surface level profile and (b) surface level fluctuations

Fig.4.11. EMBR effect on (a) time-averaged surface velocity and (b) surface velocity fluctuations

Fig.4.12. Surface level variations measured by the eddy current sensor during (a) 700 sec and (b) 20 sec with expanded scale

Fig.4.13. Power spectrum of the surface level signal measured by the eddy current sensor

Fig.4.14. Transient variations of surface level profile (a) without and (b) with EMBr by the nail board measurements

Fig.4.15. EMBR effect on (a) time-averaged surface level and (b) surface level fluctuation by the nail board measurements

Fig.4.16. Measured molten steel surface level shape (a) without EMBr and (b) with EMBr

Fig.4.17. Measured molten steel surface level fluctuations without and with EMBr

Fig.4.18. Schematic of the sloshing level mechanism (a) without and (b) with EMBr

Fig.4.19. Relation between molten steel level and liquid mold flux level (a) without EMBr and (b) with EMBr by the nail board measurements

Fig.4.20. Transient variations of surface flow pattern (a) without and (b) with EMBr by the nail board measurements

Fig.4.21. Averaged surface flow pattern (a) without and (b) with EMBR by the nail board measurements

Fig.4.22. EMBR effect on (a) time-averaged surface velocity and (b) surface velocity fluctuation by the nail board measurement

Fig.5.1. Comparison of time-averaged surface velocity magnitude between the model prediction and the plant measurement

Fig.5.2. Comparison of surface velocity magnitude fluctuation between the model prediction and the plant measurement

Fig.5.3. Time-averaged velocity vector and velocity magnitude contour in the nozzle bttom: (a) without EMBr and (b) with EMBr

Fig.5.4. Turbulent kinetic energy in the nozzle bottom: (a) without EMBr and (b) with EMBr

Fig.5.5. RMS velocity fluctuations in the nozzle bottom: (a) without EMBr and (b) with EMBr

Fig.5.6. Time-averaged velocity contour and streamlines in the mold: (a) without EMBr and (d) with EMBr

Fig.5.7. Turbulent kinetic energy contour in the mold: (a) without EMBr and (b) with EMBr

Fig.5.8. RMS velocities in the mold: (a)without EMBr and (b) with EMBr

Fig.5.9. Time-averaged velocity magnitude contour and velocity vector at the surface in the mold (a) without EMBr and (b) with EMBr

Fig.5.10. Turbulent kinetic energy contour at the surface in the mold (a) without EMBr and (b) with EMBr

Fig.5.11. RMS velocity fluctuation profiles at the surface in the mold: (a) u', (b) v', and (c) w'

Fig.5.12. Instantaneous velocity vector in the mold (a) without EMBr and (b) with EMBr

Fig.5.13. Instantaneous velocity vector in the mold (a) without EMBr and (b) with EMBr

Fig.5.14. Instantaneous velocity vector at the surface (a) without EMBr and (b) with EMBr

Fig.5.15. Location of points at the center-middle plane in the nozzle and mold

Fig.5.16. Velocity fluctuation histories during 15 sec on Point-1 in the nozzle port: (a) u, (b) v, and (c) w

Fig.5.17. Velocity fluctuation histories during 15 sec on Point-2 in the mold: (a) u, (b) v, and (c) w

Fig.5.18. Velocity fluctuation histories during 15 sec on Point-7 in the mold: (a) u, (b) v, and (c) w

Fig.5.19. Time-variation of velocity magnitude during 15 sec at the surface: (a) P-3, (b) P-4, (c) P-5, and (d) P-6

Fig.5.20. Transient surface level profile (a) without EMBr and (b) with EMBr

Fig.5.21. Instantaneous argon bubble distribution in the mold center-middle plane: (a) two-phase flow and (b) two-phase flow with EMBr

Fig.5.22. Instantaneous argon bubble distribution at the surface: (a) without EMBr and (b) with EMBr

Chapter 1: Introduction

1.1. Transient Fluid Flow Phenomena in Continuous Casting of Steel Slab

Continuous casting is used to manufacture over 95% of the steel in the world[1)] and many defects in the steel produced by this process are related to transient fluid flow in the nozzle and mold of the caster. Thus, small improvements in the understanding of transient fluid flow phenomena and their effects on steel product quality can lead to large savings.

Variations in the surface level and surface velocity in the mold of continuous steel slab casting are widely recognized as the most important factors responsible for the defects related with the fluid flow phenomena. As shown in Fig.1.1, severe surface level fluctuations can entrap slag into the molten steel.[2,3)] Abnormally high surface velocity and velocity variations, leading to asymmetric surface flow, vortex formation[4,5)], and instability at the interface between the molten steel and slag[6-8)], could entrain slag into the molten steel, causing both surface and internal defects in the steel product. On the other hand, abnormally slow surface flow could result in low and non-uniform surface temperature, thereby inducing insufficient slag melting and infiltration, meniscus freezing, hook formation[9,10)], and surface defects related to initial solidification problems.

The transient surface flow is greatly influenced by argon gas injection to prevent the nozzle clogging during continuous casting. In addition, magnetic field induced by an electromagnetic system to control flow can change the transient flow pattern at the surface by affecting time-averaged and time-dependent flow in the nozzle and mold during the casting. Thus, knowledge of the effects of argon gas injection and magnetic field application on transient fluid flow behaviors in the nozzle and mold is critical for defect-free continuous casting of steel slab.

1.2. Objectives and Contributions of the Current Work

The first objective of this thesis is to develop a two-phase flow model coupled with Magneto-Hydro-Dynamic (MHD) equations for a molten steel and argon gas system for continuous steel slab casting with double-ruler Electro-Magnetic Braking (EMBr). A second objective is to investigate transient fluid flow in the nozzle and mold of a caster that includes the application of argon gas injection and double-ruler EMBr.

The current work adopts computational modeling using steady and unsteady turbulence models, a 1/3 scale water model experiment, and plant measurements for the investigation of transient fluid flow phenomena affected by argon gas and by the electromagnetic forces induced by double-ruler EMBr.

Chapter 2 explores the mean bubble size at the refractory of an Upper Tundish Nozzle (UTN) with a slide-gate system in a continuous steel caster. The bubble size is calculated by a semi-analytical model that combines the two-stage analytical model of bubble formation developed by Bai and Thomas and the empirical model of active sites at the refractory developed by Lee et al. The predicted bubble size is then used as the input data for a Discrete Phase Model (DPM). An experiment is also performed with a 1/3 scale water model to validate the bubble formation model and extrapolate the model to predict bubble size in a stopper-rod system.

This work will be submitted to "Metallurgical and Materials Transactions B":

Seong-Mook Cho, Seon-Hyo Kim, and Brian G. Thomas: Argon Bubble Formation in the Stopper-rod Nozzle of Continuous Casting of Steel, In Writing Up

Chapter 3 presents a computational model of transient two-phase (molten steel-argon gas) flow in the nozzle and mold, determined using Large Eddy Simulation (LES) coupled with DPM. The calculated bubble size of argon gas given in Chapter 2 is chosen as the initial gas injection condition for the DPM. The LES model is compared with the measured transient surface level and surface velocity by nail board dipping tests in the plant. The plant measurements and the validated model results are then used to quantify the time-averaged and time-dependent flow in the nozzle and mold. Power spectrum analysis of the time variation of the velocity magnitude in the nozzle and mold was performed to reveal the transient variations and characteristic frequencies.

This work has been accepted for publication in the “ISIJ International”:

Seong-Mook Cho, Seon-Hyo Kim, and Brian G. Thomas: Transient Fluid Flow during Steady Continuous Casting of Steel Slabs Part I: Measurements and Modeling of Two-phase Flow, ISIJ Int, accepted, Nov 2013

Chapter 4 investigates the effect of electromagnetic braking on transient fluid flow in the nozzle and mold by employing a standard $k-\varepsilon$ model with a Magneto-Hydro-Dynamics (MHD) model and plant measurements that include magnetic field measurements, a nail board dipping test, and eddy-current sensor measurements. The model predicts single-phase (molten steel) flow with and without the double-ruler EMBr. The effect of an electric boundary condition on fluid flow is compared by adopting perfectly-insulated, perfectly-conducting walls, and real conducting steel shell cases. The plant measurements show the EMBr effect on time-averaged and time-dependent surface level and velocity, which is extensively discussed by the nozzle and mold flow pattern predicted by the steady-state molten steel flow model.

This work has been accepted for publication in the “ISIJ International” :

Seong-Mook Cho, Seon-Hyo Kim, and Brian G. Thomas: Transient Fluid Flow during Steady Continuous Casting of Steel Slabs Part II: Effect of Double-Ruler Electro-Magnetic Braking (EMBr), ISIJ Int, accepted, Dec 2013

Chapter 5 provides the LES coupled with DPM and MHD validated by the nail board dipping test, applied to quantify the effect of double-ruler EMBr on transient molten steel-argon flow in the nozzle and mold during continuous steel

casting. The time-averaged and time-dependent flow pattern with turbulent kinetic energy and velocity fluctuations in each direction (x: casting direction, y: mold width direction, z: mold thickness direction) are analyzed by considering two cases: two-phase flows with and without double-ruler EMBr. The model gives deep insight into the EMBr effect on transient two-phase fluid flow instability in the nozzle and mold. Argon gas distribution in the mold, which is affected by transient fluid flow, is also visualized and quantified.

This work will be submitted to "Metallurgical and Materials Transactions B":

Seong-Mook Cho, Seon-Hyo Kim, and Brian G. Thomas: Effect of Double-Ruler Electro-Magnetic Braking (EMBr) on Transient Two-Phase Flow in the Nozzle and Mold of Continuous Steel Slab Casting, In Writing Up

Conclusions and the future scope are discussed in Chapter 6. The results of the four chapters (Chapters 2–5) are evaluated to get an insight into the effects of argon gas and double-ruler EMBr on transient fluid flow in the nozzle and mold during continuous steel casting. Future scope of this work is discussed from the perspective of optimizing the fluid flow and reducing defects during continuous casting, by applying the computational model and research approaches, suggested in this thesis.

Other publications during Ph. D.:

Seong-Mook Cho, Seon-HyoKim, Rajneesh Chaudhary, BrianG.Thomas, Ho-JungShin, Wung-Yuel Choi, Sung-Kwang Kim: "Effect of Nozzle Clogging on Surface Flow and Vortex Formation in the Continuous Casting Mold", Iron and Steel Technology, 2012, Vol.9, No.7 ,p.85-95: reprinted from Proceedings of AISTECH2011

Rajneesh Chaudhary, Go-Gi Lee, Brian G. Thomas, Seong-Mook Cho, Seon-HyoKim, Oh-Duck Kwon,"Effect of Stopper-Rod Misalignment on Fluid Flow in Continuous Casting of Steel", Metallurgical and Materials Transactions B, 2011, Vol. 42(B), p.300-315

Seong-Mook Cho, Seon-Hyo Kim, Rajneesh Chaudhary, Brian G. Thomas, Ho-Jung Shin, Woong-Ryul Choi, Sung-Kwang Kim, "Effect of Nozzle Clogging on Surface Flow and Vortex Formation in the Continuous Casting Mold", Proceeding Paper of AISTECH 2011, Ladle and Secondary Refining/Continuous Casting/Metallurgy-Steelmaking and Casting - Control of Inclusion During Steel Continuous Casting Syposium, AISTECH 2011

Seong-Mook Cho, Hyoung-Jun Lee, Seon-Hyo Kim, Rajneesh Chaudhary, Brian G Thomas, Duck-Hee Lee, Yong-Jin Kim, Woong-Ryul Choi, Sung-Kwang Kim, Hui-

Soo Kim: "Measurement of Transient Meniscus Flow in Steel Continuous Casters and Effect of Electromagnetic Braking", Proceeding Paper of TMS 2011, Sensor, Sampling, and Simulation for Process Control Symposium, The Minerals, Metals, and Materials Society Annual Meeting 2011, Sensor, Sampling, and Simulation for Process Control (2011), p.59-66

Seong-MookCho, Go-Gi Lee, Seon-Hyo Kim ·Rajneesh Chaudhary, Oh-Duck Kwon, Brian G. Thomas: "Effect of Stopper-rod Misalignment on Asymmetric Flow and Vortex Formation in Steel Slab Casting", Proceeding Paper of TMS2010, Jim Evans Honorary Symposium, The Minerals, Metals, and Materials Society Annual Meeting 2010,The Minerals, Metals, and Materials Society,139(2010) ,p.71-77

1.3. Tables and Figures

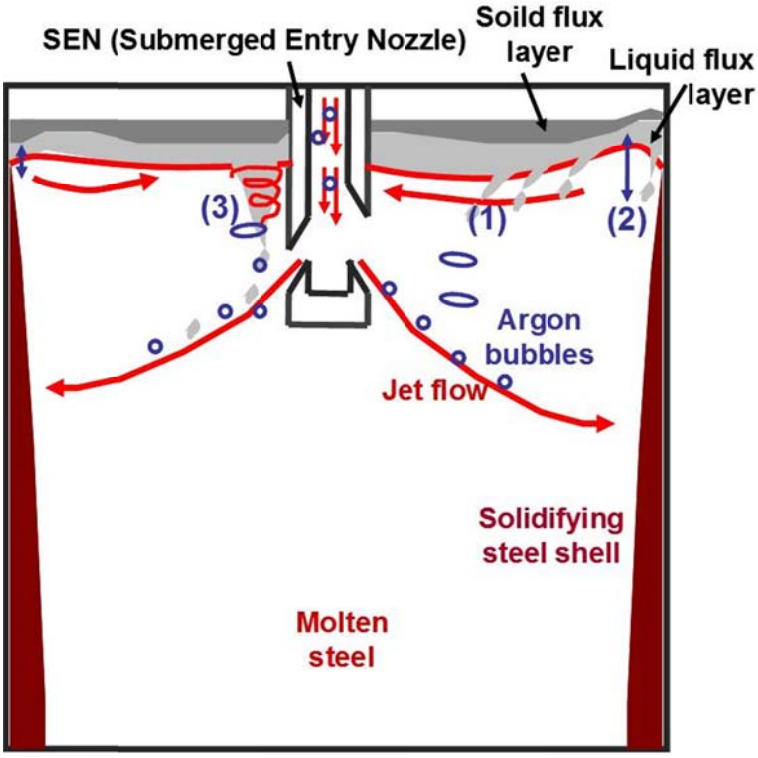

Fig. 1.1. Flow phenomena in the mold of steel slab continuous caster

1.4. Reference

1) World Steel in Figures 2012, World Steel Association, Brussels, Belgium, 2012
2) C. Ojeda, B.G. Thomas, J. Barco, J.L. Arana: Proc. of AISTech 2007, Assoc. Iron Steel Technology, Warrendale, PA, USA, 2007, 269
3) J. Sengupta, C. Ojeda, B.G. Thomas, Int. J. Cast Metals Res., Vol. 22 (2009), 8
4) S-M. Cho, G-G. Lee, S-H. Kim, R. Chaudhary, O-D. Kwon, and B. Thomas: Proc. of TMS 2010, TMS, Warrendale, PA, USA, 2010, 71
5) S-M. Cho, S-H. Kim, R. Chaudhary, B. G. Thomas, H-J. Shin, W-R. Choi, S-K. Kim: Iron and Steel Technology, Vol.9 (2012), 85
6) M. Iguchi, J. Yoshida, T. Shimizu, and Y. Mizuno: ISIJ Int., Vol. 40 (2000), 685
7) L.C. Hibbeler, R. Liu, and B.G. Thomas: Proc. of 7th ECCC, MetTecInSteelCon, Germany, 2011
8) R. Hagemann, R. Schwarze, H.P. Heller, and P.R. Scheller: Metallurgical and Materials Transaction B, Vol. 44B (2013), 80
9) J. Sengupta, B. G. Thomas, H. Shin, G. Lee, and S. Kim: Metallurgical and Materials Transactions A, Vol. 37A (2006), 1597
10) H. Shin, S. Kim, B. G. Thomas, G. Lee, J. Park, and J. Sengupta: ISIJ Int., Vol. 46 (2006), 1635

Chapter 2: Calculation of the Initial Bubble Size of Argon Gas in the Nozzle of Continuous Steel Slab Casting

2.1. Introduction

The predominant method for preventing nozzle clogging during continuous steel slab casting is argon bubble injection into molten steel. This method greatly affects the transient fluid flow pattern in the mold by inducing flow complexity and instability. Previous research has identified the volume flow rate and bubble size of the argon gas as key factors that influence the molten steel flow pattern[1-16]. Thus, quantifying these factors is important when investigating the effects of argon gas on transient fluid flow in order to reduce the defects related with fluid flow phenomena in the nozzle and mold.

This chapter provides a uniform argon bubble size for the computational modeling of two-phase (molten steel-argon gas) flow presented in Chapter 3. The calculation of bubble size is based on the two-stage (expansion and elongation) analytical model of bubble formation presented by Bai and Thomas[17], combined with an empirical model of the active sites developed by Lee et al.[18] that was based on measurements of bubble formation from pores on an engineered non-wetting surface of a porous refractory in an air-water model system.

The argon gas volume flow rate is firstly calculated using Boyle's law and Charles' law with Bernoulli's equation, while considering the molten steel temperature and pressure at the Upper Tundish Nozzle (UTN) where the argon bubbles are formed. The volume flow rate at each active site for bubble formation is then obtained by calculating the number of active sites at the UTN refractory using the empirical equation. Then, the mean bubble size is predicted from the volume flow rate per an active site, by the bubble formation model. A 1/3 water model experiment was also performed to validate the bubble formation model and to investigate application of the model to the stopper-rod system used in continuous steel slab casting.

2.2. Bubble Volume Flow Rate

During continuous steel casting with slide-gate system, argon gas is injected through the refractory of the UTN, and the gas expands when it enters the molten steel pool in the nozzle. The heated gas occupies a volume fraction F_{Ar} of the total volume flow rate of the molten steel Q_s and the argon gas $Q_{Ar,1827\,K}$. F_{Ar} is calculated as follows:

$$F_{Ar} = \frac{Q_{Ar,1827\,K}}{Q_s + Q_{Ar,1827\,K}} \times 100 \quad [2.1]$$

$$Q_s = W_{mold} \times T_{mold} \times U_{casting} \quad [2.2]$$

where W_{mold} is mold width, T_{mold} is mold thickness, and $U_{casting}$ is casting speed.

$$Q_{Ar,1827\,K} = Q_{Ar,\,273\,K} \times \left(\frac{P_{273\,K}}{P_{1827\,K}}\right) \times \left(\frac{1827\,K}{273\,K}\right) \quad [2.3]$$

$$\text{where } P_{1827K} = P_{s,tundish\_level} + \rho gh - \frac{1}{2}\rho\left(U_{s,UTN}\right)^2$$

where $P_{s,tundish\_level}$ is pressure at the tundish surface (1atm), ρ is molten steel density, h is distance from the tundish surface to the gas outlets, and $U_{s,UTN}$ is the mean velocity of the molten steel in the nozzle, as shown in Fig.2.1.

2.3. Bubble Active Site Model

The UTN refractory consists of many porous pores where bubbles can form during argon gas injection into the molten steel in a nozzle. The number of active sites at the refractory for this bubble formation during casting is investigated by considering

the gas volume flow rate, the liquid velocity in the nozzle, the refractory permeability, and the contact angle between the liquid and the refractory, as described by Lee et al[18]. Lee et al. performed the experiments using a 1/3 scale water model and a porous refractory (having non-wetting surface as shown in Fig. 2.2) of a continuous steel slab caster equipped with a slide-gate system for pouring steel into the nozzle and mold. The water model experimental results (Fig. 2.3) were used to derive the empirical equation. The number of active sites predicted using the equation was compared with the measured number of active sites. The model showed good agreement with the measurement. In this work, the model is extrapolated to the molten steel-argon system in a real continuous casting process by taking into account the expanded argon volume flow rate (which is calculated in section. 2.2) in molten steel, the nozzle flow velocity, the real refractory permeability, and the contact angle between molten steel and the refractory as follows:

$$K = \frac{7 \times \left(Q_{Ar,total(1827K),unit}\right)^{0.26} \times \left(U_{s,UTN}\right)^{0.85} \times \left(P\right)^{0.33}}{C} \quad [2.4]$$

where $\mathbf{Q}_{\mathbf{Ar,total(1827K),unit}}$ is argon gas volume flow rate per unit area (LPM/cm^2), P is permeability (nPm), and C is contact angle between molten steel and refractory (radian).

2.4. Bubble Formation Model

The bubble formation model suggested by Bai and Thomas[17)] considers the following two stages of bubble formation.

2.4.1. Expansion Stage

In the expansion stage, the bubble expands according to the balance of the drag, buoyancy, and surface tension forces on the bubble as it is held onto the tip of the gas hole, as shown in Fig.2.4(a). The force balance equation is as follows:

$$C_D \frac{1}{2}\rho\left(\bar{u}\right)^2 \pi\left(r_e\right)^2 = \frac{4}{3}\pi\left(r_e\right)^3\left(\rho - \rho_{Ar}\right)g + \frac{1}{2}\pi r_e \sigma \sin\theta_0\left(\cos\theta_r - \cos\theta_a\right) \quad [2.5]$$

$$C_D = \frac{24}{Re_{bub}}\left(1 + 0.15\left(Re_{bub}\right)^{0.687}\right) + \frac{0.42}{1 + 4.25\times10^4 \times \left(Re_{bub}\right)^{-1.16}} \quad [2.6]$$

$$\sin\theta_0\left(\cos\theta_r - \cos\theta_a\right) = 0.078773U^2 + 0.33109U - 0.06079 \quad [2.7]$$

where C_D is drag coefficient, $Re_{bub}(=\frac{\bar{u}r_e}{\nu})$ is the bubble Reynolds number, ν is the kinematic viscosity of the molten steel, ρ is molten steel density, $\bar{u}(=1.3173U\frac{(r_e)^{1/7}}{(D_N)^{1/7}})$ is steady average molten steel velocity across growing argon bubble, r_e is expansion radius of argon bubble, U is the mean liquid velocity in the nozzle, D_N is the nozzle diameter, ρ_{Ar} is argon gas density, σ is surface tension, θ_0 is static contact angle, θ_r is receding contact angle, and θ_a is advancing contact angle.

2.4.2. Elongation Stage

In the elongation stage, the drag force overcomes the buoyancy force and the surface tension force, so the bubble is elongated and expanded at the refractory wall. The elongated bubble radius, r_d, is calculated by following equation:

$$5.2692\frac{\pi u}{Q_{Ar,hole}(D_N)^{1/7}}\int_{r_e}^{r_d}\left(r^{15/7}(ar+b)^{3/2}+\frac{ar^{22/7}}{2}(ar+b)^{1/2}\right)dr=2r_d(e_d)^{3/2}+\frac{d}{2}-r_e \quad [2.8]$$

where $Q_{Ar,hole}$ is the argon gas volume flow rate into a gas hole of refractory, u is the mean vertical molten steel velocity in the nozzle, $a(=\frac{e_d - 1}{r_d - r_e})$ and $b\,(=\frac{r_d - e_d r_e}{r_d - r_e})$ are the constants related with the expansion diameter r_e, the elongated diameter r_d, and the elongation factor $e_d\,(=\frac{L}{D_d})$ of the argon bubble, and d is the pore diameter of the gas hole at the refractory surface. More details of this model can be found in reference 17.

The gas volume flow rate into a hole of refractory $Q_{Ar,hole}$ was calculated by considering the total gas volume flow rate $Q_{Ar,1827\,K}$ and the number of active sites at the refractory, #, as follows:

$$Q_{Ar,hole} = \frac{Q_{Ar,1827K}}{\#} \quad [2.9]$$

$$\# = A \times K \quad [2.10]$$

where A is the area of the UTN refractory and K ($\mathbf{\# / cm^2}$) is the number of active sites per unit area, which is obtained by Eqn 2.4.

2.5. Initial Bubble Size in Slide-Gate System of Continuous Casting

According to the process conditions (which is given in table 3.1 in Chapter 3), an average bubble size of 0.84 mm was found by coupling these two models (the bubble active site model and the bubble formation model) and extrapolating the air-water results to the real caster involving argon and molten steel. The details of the argon gas injection conditions are given in Table 2.1.

2.6. Initial Bubble Size in Stopper-Rod System of 1/3 Scale Water Model of Continuous Casting

The bubble size at the stopper-rod tip was quantified using the 1/3 scale water model shown in Fig.2.5. Geometry of the stopper-rod is shown in Fig.2.6. Six branch holes run from the main hole for injection of the argon gas into the water pool in the nozzle. Argon gas bubble formation occurs through gas expansion, elongation, and detachment at the gas hole tip, as shown in Fig. 2.7. Fig. 2.8 shows the relation between the argon gas volume flow rate and the bubbling frequency, which increases with an increasing volume flow rate of the gas. The average bubble size d_{cal} is calculated from the bubbling frequency by applying Eqn. 2.12, which is derived from Eqn. 2.11.

$$V_{bubble} = \frac{Q_{main}}{f} = \frac{4}{3}\pi\left(\frac{d_{cal}}{2}\right)^3 \quad [2.11]$$

$$d_{cal} = \left(\frac{24Q_{main}}{4\pi}\right)^{1/3} \quad [2.12]$$

where V_{bubble} is average bubble volume, f is bubbling frequency, and Q_{main} is total argon flow rate. According to this equation, increases in the bubbling frequency result in a larger average bubble size, as shown in Fig. 2.9

Table. 2.2 shows that the two-stage bubble formation model by Bai and Thomas[17)] is validated with the calculated bubble size from the measured bubbling frequency and the bubble size measured on the snapshots from high speed video. This means that the model can predict the bubble size in the stopper-rod system. The bubble formation model is applicable for predicting a size for a bubble that experiences the expansion and elongation stages of bubble formation.

2.7. Summary and Conclusions

The argon bubble size in a steel slab continuous caster with a slide-gate system is predicted by a semi-analytical model that considers the volume flow rate, the number of active sites at the UTN refractory, and the two stages of bubble formation. The model extrapolates the results of a water-air system to a steel-argon system in a real caster. The mean bubble size predicted by the model will be used as input data for argon gas injection in the DPM model, with the assumption that no coalescence or breakup of the bubbles occurs in the nozzle or mold during continuous casting. The bubble formation model shows good agreement with the measurements obtained with the 1/3 water model with a stopper-rod system. The model can therefore be used to predict the bubble size in future work that considers bubble behavior in the stopper nozzle.

2.8. Tables and Figures

Table 2.1. Conditions of argon gas injection

UTN refractory area		0.072 m^2
Refractory permeability		7.52 nPm
Steel velocity in the nozzle		1.58 m/sec (Reynolds number: 148048)
Contact angle between molten steel and refractory		107 degree (1.87 radian)
Active sites at the refractory		4.82 # / cm^2
Volume flow rate		9.2 SLPM (1 atm, 273 K); 33.0 LPM (1.87 atm, 1827 K)
Volume fraction		5.6 % (hot)
Active sites at the refractory		4.82 # / cm^2
Mean bubble diameter	expansion	0.48 mm
	elongation	0.84 mm
Gas injection velocity through UTN		0.008 m/sec

Table 2.2. Comparison of bubble size between prediction and measurement

Prediction		Measurement
Calculation of diameter from bubbling frequency from video frames	Bai's analytical model	
4.5 mm	4.3 mm	5 mm

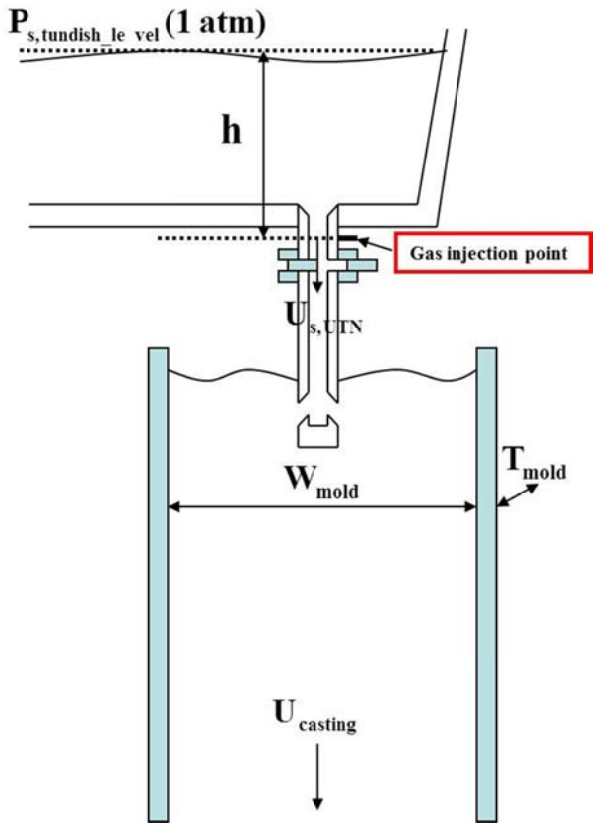

Fig.2.1. Schematic of continuous caster with slide-gate system

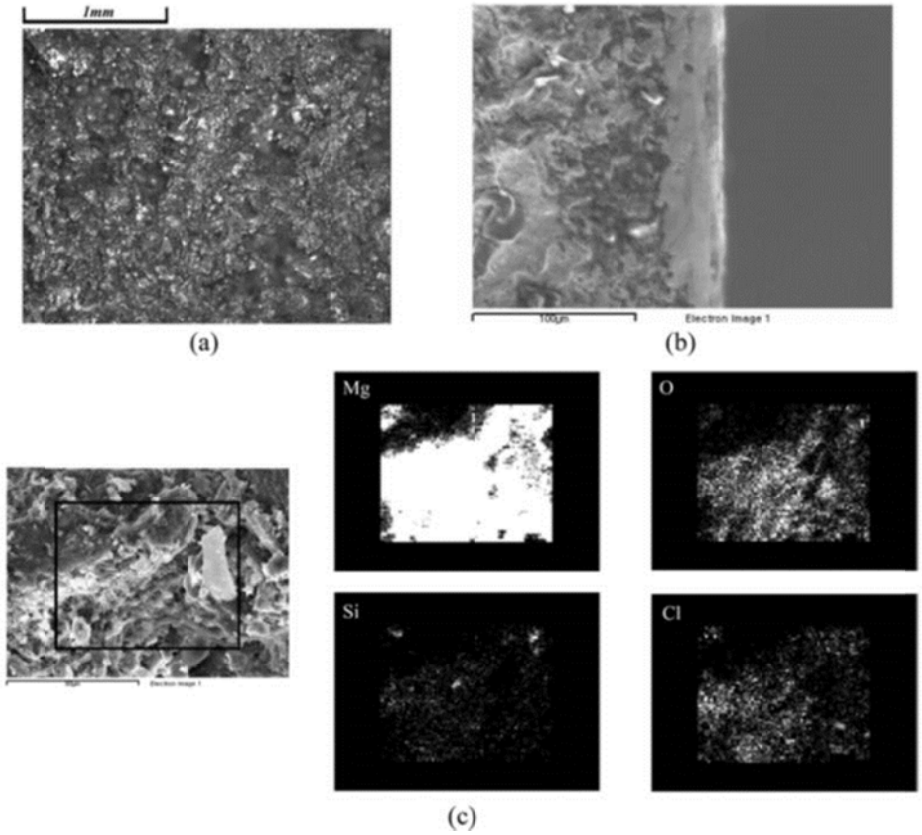

Fig.2.2. UTN refractory [ref.18]: (a) pores, (b) surface coating layer, and (c) chemical experiment of the coating layer

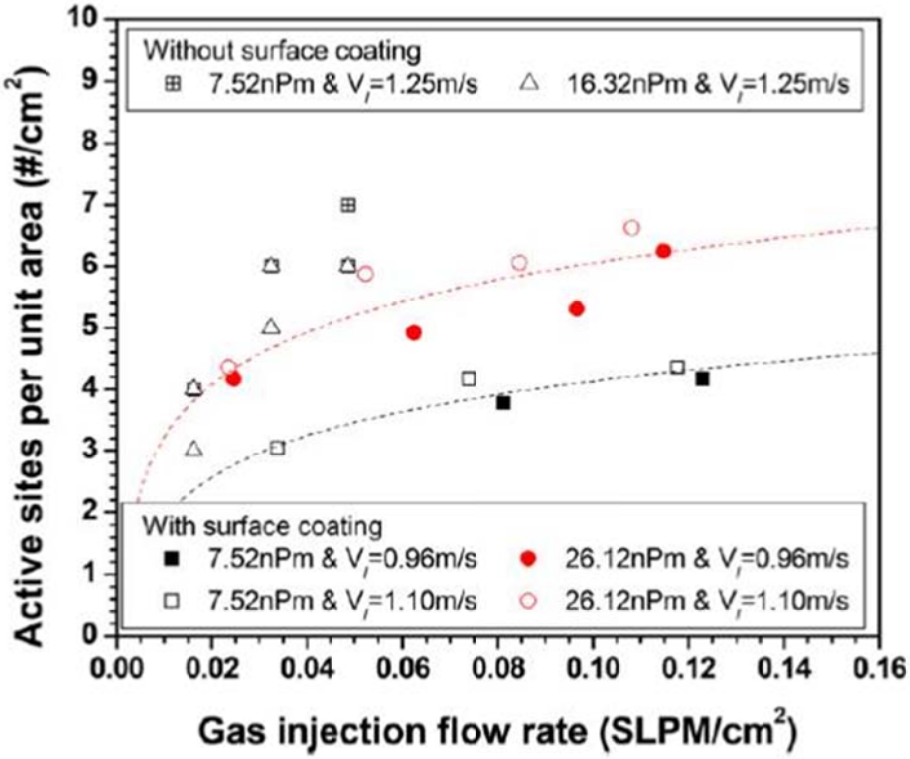

Fig.2.3. Extrapolating graph of the number of active sites [ref.18]

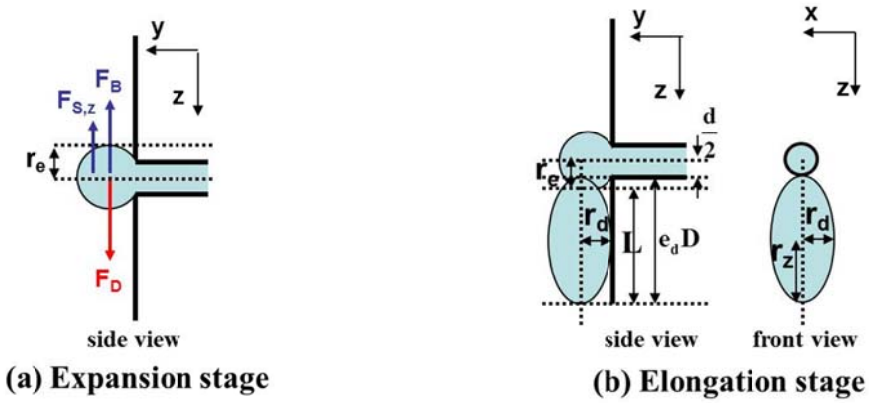

Fig.2.4. Schematic of initial bubble formation: (a) expansion stage and

(b) elongation stage

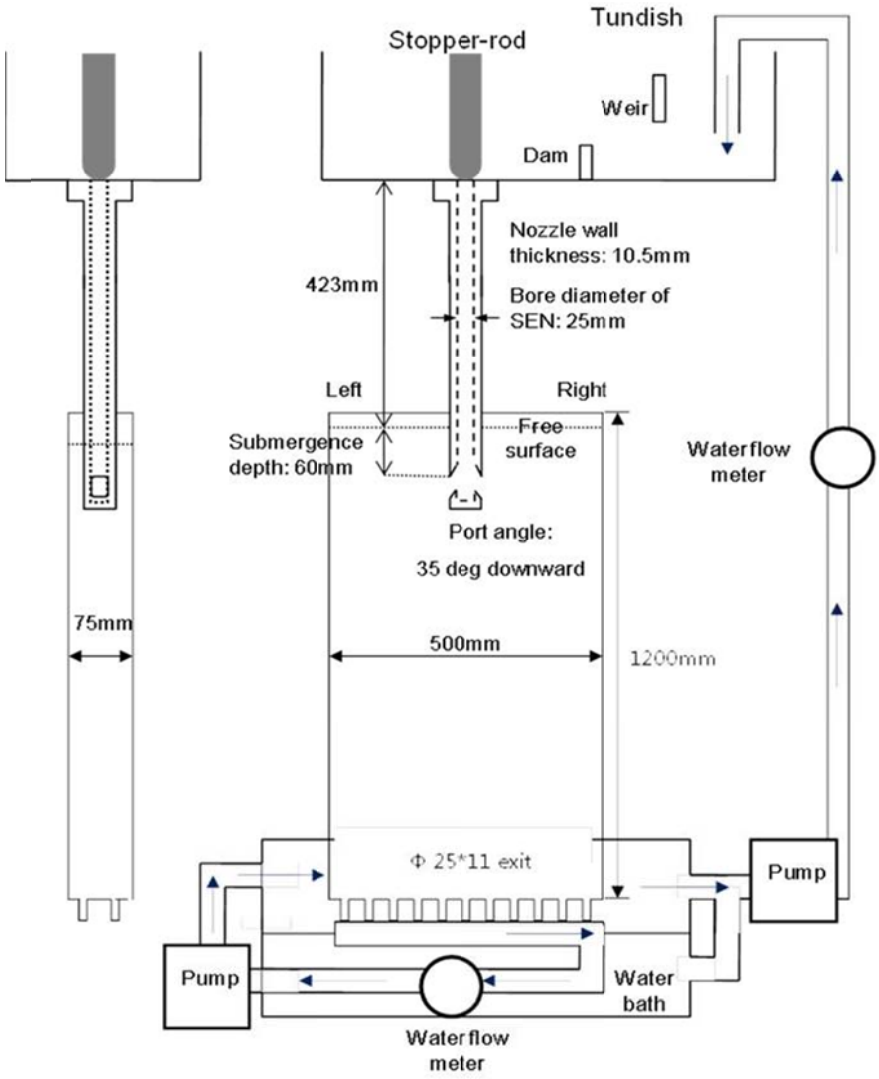

Fig.2.5. Schematic of 1/3 Scale Water Model

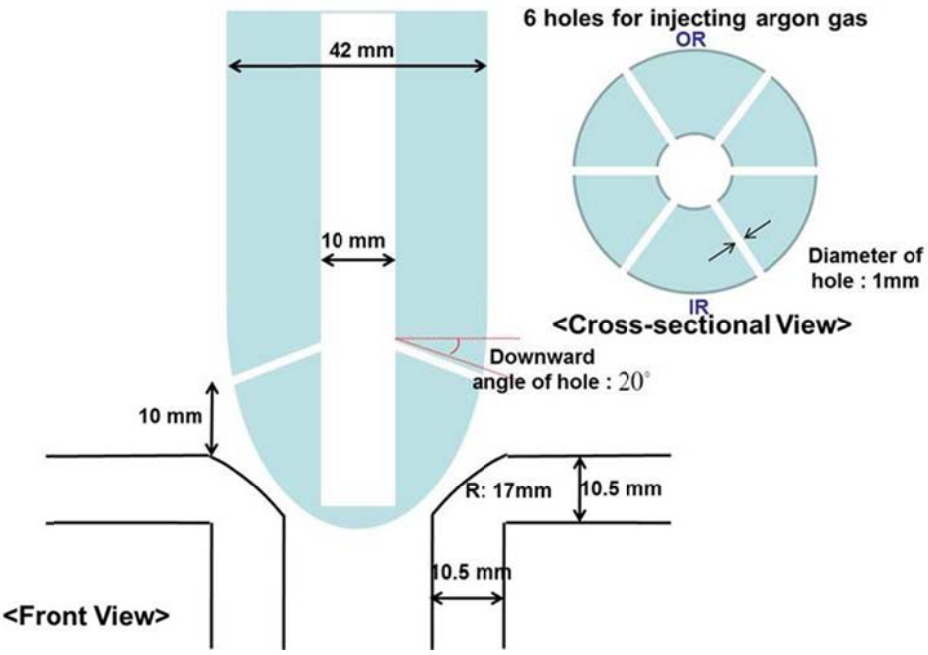

Fig.2.6. Geometry of Stopper-rod in the Water Model

Fig.2.7. Snapshot of Initial Bubble Behavior at Stopper-rod Tip

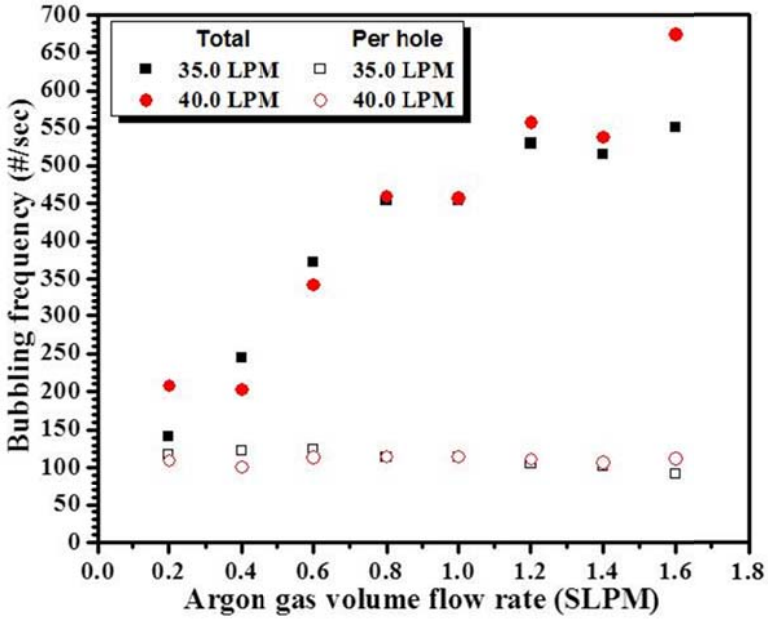

Fig.2.8. Relation between Argon Gas Volume Flow Rate and Bubbling Frequency

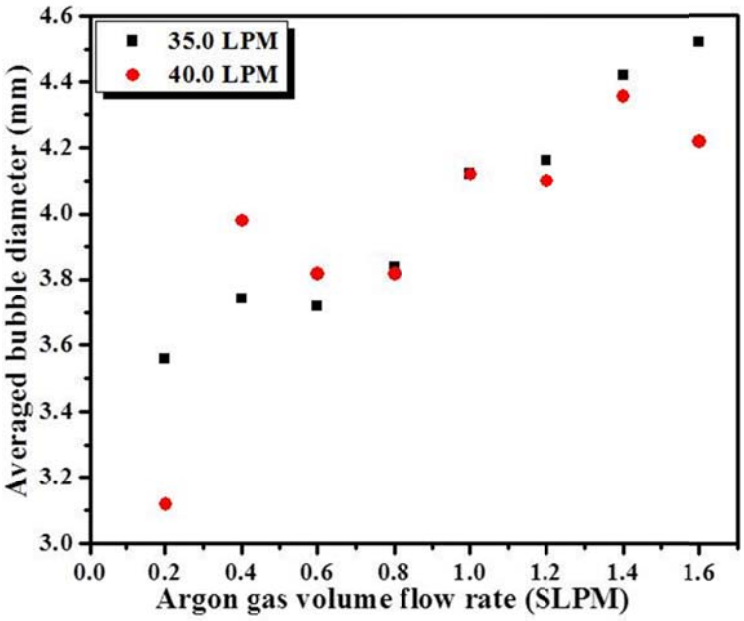

Fig.2.9. Relation between Argon Gas Volume Flow Rate and Bubble Size

2.9. References

1) N. Bessho, R. Yoda, and H. Yamasaki: Iron Steelmaker, Vol. 18 (1991), 39

2) P. Andrzejewski, K. –U. Kohler, and W. Pluschkeli: Steel Res., Vol. 3(1992), 242

3) H. Yu and M. Zhu: ISIJ Int., Vol. 48 (2008), 584

4) B. G. Thomas, X. Huang, and R. C. Sussman: Metallurgical and Materials Transaction B, Vol. 25B (1994), 527

5) Z. Wang, K. Mukai, and D. Izu: ISIJ Int., Vol. 39 (1999), 154

6) R. Sanchez-Perez, R. D. Morales, M. Diaz-Cruze, O. Olivares-Xometl, and J. P-Ramos: ISIJ Int., Vol. 43 (2003), 637

7) N. Kubo, T. Ishii, J. Kubota, and N. Aramaki: ISIJ Int, Vol. 42 (2002), 1251

8) V. Singh, S. K. Dash, J. S. Sunitha, S. K. Ajmani, and A. K. Das: ISIJ Int, Vol. 46 (2006), 210

9) M. Burty, M. De Santis, and M. Gesell: Revue de Metallurgie, Vol. 99(2002), 49

10) B. G. Thomas and L. Zhang: ISIJ Int, Vol. 41 (2001), 1181

11) T. Toh, H. Hasegawa and H. Harada: ISIJ Int, Vol. 41 (2001), 1245

12) H. Bai and B. G. Thomas: Metallurgical and Materials Transaction B, Vol. 32B (2001), 269

13) Y. Miki and S. Takeuchi: ISIJ Int, Vol. 43 (2003), 1548

14) Z. Liu, B. Li, M. Jiang, and F. Tsukihashi: ISIJ Int, Vol. 53 (2013), 484

15) S. Kunstreich, P. H. Dauby, S-K. Baek, and S-M. Lee: European Continuous Casting Conference, Nice, France, 2006, 20

16) P. H. Dauby: Revue de Metallurgie, Vol. 109(2012), 113

17) H. Bai and B. G. Thomas: Metallurgical and Materials Transaction B, Vol. 32B (2001), 1143

18) G-G. Lee, B. G. Thomas, and S-H. Kim: Met. Mater. Int., Vol. 16 (2010), 501

Chapter 3: Modeling of Transient Two-Phase Fluid Flow in the Nozzle and Mold of Continuous Steel Slab Casting & Plant Measurements

3.1. Introduction

Argon gas is injected to prevent nozzle clogging in continuous steel casting, but may cause complexity and instability of transient flow pattern. Applying a magnetic field induces Electro-Magnetic Braking (EMBr) forces which also affect transient mold flow and stability. It is important to understand the effects of argon gas and EMBr on transient fluid flow to prevent defects during the continuous casting. This thesis investigates the effects of argon gas (Chapter 3) and EMBr (Chapter 4 and 5) on transient flow in the nozzle and mold.

Many researchers have investigated the effect of argon gas on time-averaged flow in the nozzle and mold.[1-11] However, there is less study on the effect of gas on transient flow.[12-16] Using a standard steady-state $k-\varepsilon$ model, Bai and Thomas found that increasing argon gas volume fraction or bubble diameter bends the jet angle more upward and also increases turbulence.[12] Using Large Eddy Simulation (LES) and water modeling, several studies observed long-term asymmetry and unbalanced transient flow in the lower rolls, causing bubbles to penetrate deeply.[13,14] Using nail-board dipping tests, Kunstreich et al.[15] and Dauby[16] found detrimental ranges of operating conditions including argon gas injection rates that caused unstable, complex

flow, resulting in defects. Both transient computational model and plant measurements are needed to understand quantitatively transient flow and to find methods to prevent defects.

In Chapter 3 of this thesis, transient flow of molten steel and argon gas during steady continuous casting of steel slabs is investigated by applying both plant measurements and computational modeling. Nail board dipping tests quantify transient and time–averaged surface level and surface velocity of molten steel. Thickness and level motion of the liquid mold flux (slag) are also investigated. Further insight into transient flow in the nozzle and mold is quantified by LES coupled with Lagrangian Discrete Phase Model (DPM) for argon gas injection. Power spectrum analysis of the predicted velocity history was performed to reveal the transient variations and characteristic frequencies.

3.2. Plant Experiments

Plant measurements were conducted on a conventional continuous steel slab continuous caster at POSCO Gwangyang Works #2-1 caster in 2008 and in 2010. Results from 2010 measurements are included here while Chapter 4 includes both trials. Processing conditions for the plant measurements are given with nozzle and mold dimensions in Table 3.1. Flow in this 250 x 1300mm caster is through a standard bifurcated Submerged Entry Nozzle (SEN) with rectangular ports, controlled by a

slide-gate system with middle plate movement between Outside Radius (OR) and Inside Radius (IR) as shown in Fig.3.1. During the measurements, argon gas of 9.2 SLPM was injected through the Upper Tundish Nozzle (UTN), and expanded to 33.0 LPM. The heated gas occupies 5.6 % volume fraction.

Transient surface level and velocity in the mold were quantified via both eddy-current sensor measurements and nail board dipping tests. The mold water-box had a cavity that contained the static DC magnets for a double-ruler EMBr system by ABB. The applied field strength was measured without molten steel using a Gauss meter.

3.2.1. Eddy-current Senor Measurements

The eddy-current sensor detects the surface level, and sends the signal to a controller, which aims to maintain a constant average liquid level in the mold by moving the middle plate of the slide-gate to adjust the open area of the nozzle. This sensor was positioned over the "quarter point" located midway between the SEN and Narrow Face (NF). If the level drops slightly, the slide-gate opens to increase flow rate until the level returns to the set-point, located 103 mm below top of the mold. The sensor signal sent to the controller is filtered intentionally to remove the high-frequency level variations, which cannot be controlled. Averages, standard deviations, and power spectra of the 1 sec moving time-average of the surface level signal in 2010 trial were calculated both with and without EMBr and are presented in Part II

3.2.2. Nail Board Dipping Tests

Nail board dipping tests were conducted to quantify surface level, surface velocity, and their fluctuations for the trials in both 2008 and 2010. Nail board dipping tests are commonly used to investigate mold surface flow due to their convenience and efficiency.[17-21] In these trials, two rows of ten 5 mm-diameter, 290 mm-long STainless Steel (STS) nails, spaced 50mm apart were attached to each wood board, together with 3 mm diameter aluminum nails, as shown in Fig.3.2. The nail board with the STS and Al nails was immersed into the mold, centered between the IR and OR, and between the SEN and the NF on the opposite side from the eddy-current sensor. The nail board is supported above the oscillating mold on two bent rods to keep it stable and level without tilting. As molten steel flows around the nails, it is pushed up on the windward side, and down on the leeward side, so solidifies an angled lump around each nail. As shown in Fig.3.3, after taking out the nails from the molten steel pool, these solidified steel lumps are used to reveal the liquid level profile and the velocity across the top of the mold. Surface velocity at the nail is estimated from the measured lump height difference h_{lump} (mm), and lump diameter ϕ_{lump} (mm), using the empirical equation developed by Liu et al.[19] based on the data of computational modeling by Rietow et al.[20]

$$V_{surface} = 0.624 \cdot \left(\phi_{lump}\right)^{-0.696} \cdot \left(h_{lump}\right)^{0.567} \quad [3.1]$$

For each test, the nail board was dipped into the molten steel pool for ~3 sec with 1 minute time interval between tests. The slag layer thickness h_{slag} is estimated from the height difference between the steel lump and the melted-back aluminum nail.

3.2.3. Magnetic Field Measurements

The magnetic field applied by the double ruler EMBr was measured using a Gauss meter at 69 data points in the mold cavity without molten steel. On each of three vertical lines, located 0, 350, and 700mm from the mold center, 23 positions are measured by lowering the Gauss meter downward in 50mm increments from the mold top. The measurements were extrapolated to cover the entire nozzle and mold, and input to a standard $k-\varepsilon$ model with EMBr, as discussed in detail in Chapter 4.

3.3. Plant Measurement Results

Plant measurement results in this paper are from the 2010 trial (no EMBr) and are presented in Figs.3.4-3.8 for surface level and velocity.

3.3.1. Surface Level

The transient surface level profile of the interface between the molten steel and the slag layer in the mold was quantified during a 9-minute time interval via 10 nearly instantaneous snapshots using nail board dipping tests and are shown in Fig. 3.4. The time-average of these surface level shapes is shown in Fig. 3.5(a), and the surface level fluctuations are presented as the standard deviation of the snapshots in Fig. 3.5(b). These surface level profiles reveal evidence of transient low-frequency sloshing or waves between the SEN and the NF. Usually, surface level near the SEN and the NF is higher than at the quarter point, which is typical of surface behavior induced by a classic double roll pattern in the mold. With progressing time, the level profiles change, with the NF region higher at the same time the SEN region is lower, and vice versa. The magnitude of these rising and falling levels is up to 20mm, (eg. Fig.3.4 frames 7 and 8). The sloshing period is shorter than 1 minute, and other fluctuations complicate the profiles, so it is not easy to see in Fig.3.4 alone. Surface level fluctuations shown in Fig.3.5(b) become more severe towards the SEN. In the quarter point region, surface level is the lowest and also exhibits the highest stability. Surface level fluctuations near the NF are intermediate. This is consistent with a slow sloshing mechanism, where the surface level pivots around the quarter point region.

The surface level of the steel-slag interface near the OR is usually slightly higher than near the IR. The level fluctuations near the OR were also slightly higher in the 2008 trial[21)], but not in the 2010 trial shown here in Fig.3.5(b), so this trend is not consistent and needs further study with more data.

Slag level profiles, also shown in Figs.3.4 and 3.5, show corresponding transient flow with sloshing, as influenced by the molten steel level motions. The slag surface level shape is similar to that of the steel. These results suggest that the slag level is simply lifted up and down by the molten steel motion. This contrasts with previous findings[22)], where large differences in slag layer thickness were observed due to slag flow from the high NF region towards the SEN, which resulted in a thinner slag layer near the NF due to displacement. Perhaps there was insufficient time for slag flow due to gravity and displacement in the current study, or perhaps the effective slag viscosity was lower in the previous study, owing to foam formation from the higher argon flow.[23)] The relation of the surface level motion between the molten steel and the slag will be further discussed in detail in Chapter 4.

3.3.2. Surface Velocity

Transient evolution of the surface flow pattern and velocity of the molten steel is visualized during the 9 minute period by snapshots taken 1 minute apart, and are shown in Fig.3.6. Each surface flow pattern snapshot shows flow direction vectors as arrows with velocity magnitude represented by the length of each arrow. Most flow is towards the SEN, which is typical of a classic double-roll flow pattern in the mold. The profiles also show significant time variation and strong fluctuating cross-flow between the IR and OR. This surface cross-flow indicates variable asymmetric flow in the mold, likely related to the slide-gate movement between OR and IR, which

induces swirl at the nozzle ports.[24] Most surface flow is slightly biased from the OR towards the IR. This effect is clearly seen in the measurements of the row of nails near the OR. Surface flows measured near the IR show strong random variations towards either the IR or the OR. Surface flow very near the NF mostly goes towards the NF or the IR. This suggests a small region of recirculating flow in the top of the mold near the NF. Time-averaging of these surface flow patterns, given in Fig.3.7 confirms the biased cross-flow towards the IR.

The velocity magnitudes across the mold are shown in Fig.3.8(a), and their variations are given in Fig.3.8(b). Higher surface velocities are found towards the quarter point, midway between the SEN and the NF, as typical for a double-roll flow pattern[3,7, 25] The highest velocity is found closer to the OR. Surface velocity fluctuations are consistently very large ~0.12 m/sec across the entire mold width. These chaotic fluctuations are almost 50% of the average surface velocity magnitude for both the IR and the OR. This finding suggests that surface velocity fluctuations may be even more important than average surface velocity to understand surface flow phenomena related to defect formation.

3.4. Computational Models

Three-dimensional finite-volume computational models, including a standard $k-\varepsilon$ model and LES coupled with a Lagrangian Discrete Phase Model (DPM) were

applied to predict transient flow of molten steel and argon gas in the nozzle and mold. First, steady-state single-phase flow of molten steel was predicted with the standard $k-\varepsilon$ model. Then, LES coupled with Lagrangian DPM was applied to calculate transient molten steel flow with argon gas, starting from the steady-state single-phase flow field. These models were implemented into the commercial package ANSYS FLUENT[29] and are summarized below.

3.4.1. Single-phase (Molten Steel) Model of Steady Flow

A steady-state Reynolds Averaged Navier-Stokes (RANS) model using the standard $k-\varepsilon$ model for turbulence was used to model single-phase flow. The continuity equation for mass conservation of mass is given as

$$\frac{\partial}{\partial x_i}\left(\rho \bar{u}_i\right) = S_{shell,\ mass} \quad [3.2]$$

$$S_{shell,mass} = -\frac{\rho u_{casting} A}{V} \quad [3.3]$$

where ρ is molten steel density, $\overline{u}_i$ is average velocity in the 3 coordinate directions, $S_{shell,mass}$ is a mass sink term to account for solidification of the molten steel,[26] $u_{casting}$ is casting speed, A is projection of surface area of the steel shell in the casting direction, and V is volume of each cell with the sink term. This sink term in Eq.3.3 is only applied to the fluid cells on the wide faces and the narrow faces next to the interface between the fluid zone of the molten steel and the solid zone of the steel shell.

The Navier-Stokes equation for momentum conservation is as follows

$$\frac{\partial}{\partial x_j}\left(\rho \overline{u}_i \overline{u}_j\right) = -\frac{\partial \overline{p}^*}{\partial x_i} + \frac{\partial}{\partial x_j}\left[\left(\mu + \mu_t\right)\left(\frac{\partial \overline{u}_i}{\partial x_j} + \frac{\partial \overline{u}_j}{\partial x_i}\right)\right] + S_{shell,mom,i} \quad [3.4]$$

$$\mu_t = \rho C_\mu \frac{k^2}{\varepsilon} \quad [3.5]$$

$$S_{shell,\,mom,i} = -\frac{\rho u_{casting} A}{V}\overline{u}_i \quad [3.6]$$

$\overline{p}^*$ is modified pressure ($\overline{p}^* = \overline{p} + \frac{2}{3}\rho k$), $\overline{p}$ is gauge static pressure, μ is dynamic viscosity of molten steel, μ_t is turbulent viscosity, k is turbulent kinetic energy, ε is turbulent kinetic energy dissipation rate, and C_μ is a constant, 0.09. $S_{shell,mom,i}$ is a momentum sink term in each component direction to consider solidification of the molten steel on the wide faces and the narrow faces.[26)] This term is also applied to the cells which consider $S_{shell,mass}$. The mass and momentum sink terms $S_{shell,mass}$, $S_{shell,mom,i}$ are implemented into ANSYS FLUENT with User-Defined Functions (UDF).

In the standard $k-\varepsilon$ model, two additional scalar transport equations, of turbulent kinetic energy k and its dissipation rate ε, are required to model turbulence:

$$\frac{\partial}{\partial x_i}(\rho k \overline{u}_i) = \frac{\partial}{\partial x_j}\left[\left(\mu + \frac{\mu_t}{\sigma_k}\right)\frac{\partial k}{\partial x_j}\right] + G_k - \rho\varepsilon \quad [3.7]$$

$$\frac{\partial}{\partial x_i}(\rho \varepsilon \overline{u}_i) = \frac{\partial}{\partial x_j}\left[\left(\mu + \frac{\mu_t}{\sigma_\varepsilon}\right)\frac{\partial \varepsilon}{\partial x_j}\right] + C_{1\varepsilon}\frac{\varepsilon}{k}G_k - C_{2\varepsilon}\rho\frac{\varepsilon^2}{k} \quad [3.8]$$

where G_k is generation of turbulent kinetic energy due to mean velocity gradients, σ_k and σ_ε are turbulent Prandtl numbers associated with k and ε, 1.0, and 1.3 respectively, $C_{1\varepsilon}$ and $C_{2\varepsilon}$ are standard constants of 1.44 and 1.92.

3.4.2. Two-phase (Molten Steel with Argon Gas) Model of Transient Flow

The transient multiphase flow field was calculated using LES with an Eulerian model of the molten steel phase coupled with a Lagrangian DPM of the argon gas.[29)]

3.4.2.1. Eulerian Model for Molten Steel Phase

Mass conservation is as follows

$$\frac{\partial}{\partial x_i}(\rho u_i) = S_{shell,\ mass} \qquad [3.9]$$

where ρ is molten steel density, u_i is velocity, and $S_{shell,mass}$ is a mass sink term for solidification given in Eqn.3.3. The time-dependent momentum balance equation is given by

$$\frac{\partial}{\partial t}(\rho u_i) + \frac{\partial}{\partial x_j}(\rho u_i u_j) = -\frac{\partial p^*}{\partial x_i} + \frac{\partial}{\partial x_j}\left[(\mu + \mu_t)\left(\frac{\partial u_i}{\partial x_j} + \frac{\partial u_j}{\partial x_i}\right)\right] + S_{shell,mom,i} + S_{Ar,mom,i} \quad [3.10]$$

$S_{Ar,mom,i}$ is a momentum source term to consider the effect of argon gas bubble motion on molten steel flow, which is calculated by the DPM model, and other terms are defined previously. Although the subgrid-scale model for μ_t produces some velocity filtering on the local scale, the effect is small, so the bar (averaging) symbol is dropped, in order to distinguish the variables from those of the time-averaged standard $k-\varepsilon$ model.

For μ_t, the Wall-Adapting Local Eddy (WALE) subgrid-scale viscosity model was adopted

$$\mu_t = \rho(L_S)^2 \frac{\left(S_{ij}^d S_{ij}^d\right)^{3/2}}{\left(S_{ij}S_{ij}\right)^{5/2} + \left(S_{ij}^d S_{ij}^d\right)^{5/4}} \quad [3.11]$$

where $L_S = \min(\kappa d, C_w V^{1/3})$, $S_{ij} = \frac{1}{2}\left(\frac{\partial u_i}{\partial x_j} + \frac{\partial u_j}{\partial x_i}\right)$,

$S_{ij}^d = \frac{1}{2}\left(g_{ij}^{\ 2} + g_{ji}^{\ 2}\right) - \frac{1}{3}\delta_{ij} g_{kk}^{\ 2}$, $g_{ij} = \frac{\partial u_i}{\partial x_j}$, $g_{ij}^{\ 2} = g_{ik} g_{kj}$, $\delta_{ij} = 1(i = j)$ or $0(i \neq j)$. κ is the von Karman constant 0.418, d is distance from the cell center to the closet wall, C_w is constant 0.325, and V is cell volume.

3.4.2.2. Lagrangian DPM Model for Argon Gas

To calculate $S_{Ar,mom,i}$ for Eqn.3.10, the Lagrangian DPM model solves a force balance on each argon bubble:

$$\frac{du_{Ar,i}}{dt} = F_{drag,i} + F_{buoyancy,i} + F_{virtual\_mass,i} + F_{pressure\_gradient,i} \quad [3.12]$$

where the following forces act in each coordinate direction per unit mass of argon gas: $F_{drag,i}$ is drag force, $F_{buoyancy,i}$ is buoyancy force, $F_{virtual\_mass,i}$ is virtual mass force, and $F_{pressure\_gradient,i}$ is pressure gradient force. $F_{drag,i}$ is calculated as follows

$$F_{drag,i} = \frac{3}{4}\frac{\mu C_D Re}{\rho_{Ar}(d_{Ar})^2}\cdot(u_i - u_{Ar,i}) \quad [3.13]$$

$$Re = \frac{\rho d_{Ar}|u_{Ar} - u|}{\mu} \quad [3.14]$$

C_D is drag coefficient, μ is dynamic viscosity of molten steel, Re is relative Reynolds number, $u_{Ar,i}$ is argon bubble velocity, ρ_{Ar} is argon gas density, and d_{Ar} is diameter of argon bubble. The drag coefficient is from Kuo and Wallis.[27] Computational modeling using the drag coefficient in molten steel and argon gas system showed reasonable agreement with measurements.[28] The drag coefficient varies with relative Reynolds number and Weber number and is implemented to ANSYS FLUENT by a User-Defined Function (UDF).

$$\begin{aligned} C_D &= \frac{16}{Re} \quad (Re < 0.49) \\ &= \frac{20.68}{Re^{0.643}} \quad (0.49 < Re < 100) \\ &= \frac{6.3}{Re^{0.385}} \quad (100 < Re) \\ &= \frac{We}{3} \quad \left(\frac{2065.1}{We^{2.6}} < Re\right) \\ &= \frac{8}{3} \quad (8 < We) \end{aligned} \quad [3.15]$$

where $We = \frac{\rho d_{Ar} \left| u_{Ar} - u \right|^2}{\sigma_{steel-argon}}$

The other forces are calculated as follows[29]:

$$F_{buoyancy,i} = \frac{\rho_{Ar} - \rho}{\rho_{Ar}} g_i, \quad F_{virtual\_mass,i} = \frac{1}{2} \frac{\rho}{\rho_{Ar}} \frac{d}{dt} \left(u_i - u_{Ar,i} \right),$$

$$F_{pressure\_gradient,i} = \frac{\rho}{\rho_{Ar}} u_i \frac{\partial u_i}{\partial x_i} \quad [3.16]$$

$S_{mom,Ar,i}$ is calculated as follows

$$S_{mom,Ar,i} = -\left(F_{drag,i} + F_{buoyancy,i} + F_{virtual\_mass,i} + F_{pressure\_gradient,i} \right) \dot{m}_{Ar} \Delta t \quad [3.17]$$

$\dot{m}_{Ar}$ is mass flow rate of injected argon gas bubble and Δt is time step of bubble trajectory calculation. In this work, Δt is same time step size used for the LES.

3.4.3. Bubble Size Model

For the Lagrangian DPM of this work, a uniform argon bubble size was chosen, based on a two-stage (expansion and elongation) analytical model of bubble formation by Bai and Thomas[30] combined together with an empirical model of active sites by Lee et al.[31] based on measurements of bubble formation from pores on an engineered non-wetting surface of a porous refractory in an air-water model system. An average bubble size of 0.84 mm was found by coupling these two models and extrapolating the air-water results to the real caster involving argon and molten steel.

3.4.4. Domain, Mesh, and Boundary Conditions

The computational model domain is a symmetric half of the real caster, including part of the bottom of the tundish, the UTN, the slide-gate, SEN with nozzle port, and the top 3000 mm of the liquid pool in the mold and strand. The half domain includes both the IR and OR on the south side of the caster, assuming a symmetry plane between NFs. So the domain includes the asymmetric effect of the 90 degree movement[12] of the middle plate of the slide-gate between IR and OR. The steel shell thickness profile is shown in Fig.3.9 and is given by

$$S\,(\mathrm{mm}) = k\sqrt{t\,(\mathrm{sec})} \qquad [3.18]$$

S is steel shell thickness at location below meniscus, t is time for steel shell to travel to the location, and constant k can be calculated according to measured shell thickness in a break-out shell. The constant k is $2.94\ \mathrm{mm/sec}^{1/2}$. The calculation domain includes the liquid pool, and does not include the solid shell, although both regions are shown in Fig.3.10(a). This domain consists of ~ 1.8 million hexahedral cells as shown in Fig. 3.10(b), (c), (d), and (e).

In both the standard $k-\varepsilon$ model and the LES, constant velocity was fixed as the inlet condition at the outside surface of the tundish bottom region. This velocity (0.00938 m/sec) was calculated according to the molten steel flow rate and the surface area (0.982 m^2) of the circular top and cylindrical sides of the tundish bottom region. Corresponding small values of turbulent kinetic energy ($10^{-5} m^2/\sec^2$) and turbulent kinetic energy dissipation rate ($10^{-5} m^2/\sec^3$) were fixed at the inlet for the $k-\varepsilon$ model.

A pressure outlet condition was chosen on the domain bottom at the mold exit as 0 pascal gauge pressure. The standard $k-\varepsilon$ model also imposed small values of turbulent kinetic energy ($10^{-5} m^2/\sec^2$) and its dissipation rate ($10^{-5} m^2/\sec^2$) for any back flow entering the domain exit into the lower recirculation zone.

In both models, the interface between the molten steel fluid flow zone and the steel shell and at the top surface (interface between steel and slag pool) was given by a stationary wall with a no slip shear condition. For the DPM model calculation, argon gas (16.5 LPM (5.6%) for half domain) was injected through the inner-wall

surface area of the UTN refractory with uniform size bubbles of 0.84 mm. An escape condition was adopted at the domain bottom exit and the top surface. A reflection condition was employed at other walls.

3.4.5. Computational Method details

In the standard $k-\varepsilon$ model, the five equations for the three momentum components, k, ε, and the pressure Poison equation were discretized using the finite volume method in ANSYS FLUENT with a second order upwind scheme for convection terms.[29)] These discretized equations were solved for velocity and pressure by the Semi-Implicit Pressure Linked Equations (SIMPLE) algorithm, which started with an initial value of zero velocity in all cells. The LES with the Lagrangian DPM calculated three momentum components and pressure considering the interaction between the molten steel and argon bubble using a time step ($\Delta t = 0.0006$ sec). The steady-state single-phase molten steel flow field calculated by the standard $k-\varepsilon$ model was used to initialize the LES model. The transient, two-phase LES model was started at time = 0 sec and run for 19.8 sec. The flow was allowed to develop for 15 sec, and then a further 4.8 sec of data was used for compiling time-averages.

3.5. Model Results and Discussion

3.5.1. Nozzle Flow

Transient flow in the bottom region of the SEN shows an asymmetric swirling flow pattern exiting the nozzle port, as shown in Fig.3.11. This swirl is induced by the asymmetric shape of the open area in the middle plate of the slide-gate that delivers the molten steel. The time-averaged flow pattern shows a clockwise rotation in the nozzle well. The two snapshots of the instantaneous flow pattern show strong as well as weak rotation. When the clockwise rotating flow becomes weak, counter-clockwise rotating flow towards to OR is often observed, in both the model[24)], and in a water model of this caster.[32)]

An influence of asymmetric inlet velocity on turbulent pipe flow is expected when the following condition holds [33)]

$$\frac{L}{D} < 4.4\left(\mathrm{Re}\right)^{1/6} \quad [3.19]$$

where L is pipe length, D is pipe diameter, and Re is Reynolds number ($\mathrm{u}D\rho / \mu$). For the slide-gate nozzle here, L/D (nozzle length from middle plate to port measured in nozzle bore diameters) is ~10.1 which is much less than the critical L/D of ~31.9 from Eq.3.19. Thus, the asymmetric flow created at the slide-gate persists down to the port and causes the rotating flow pattern.

3.5.2. Mold Flow

Time-averaged and instantaneous contour plots of velocity magnitude at the center plane between IR and OR in the mold are shown in Fig.3.12. A classic double roll pattern is observed in the 4.8 sec time average. Two instantaneous snapshots separated by 1.2 sec show up-and-down wobbling of jet flow in the mold, which induces different impinging points of the jet onto the NF. This causes fluctuating strengths of the flow up the NF, and corresponding fluctuations of the surface flow with time. Jet wobbling also induces corresponding variations in the argon gas distribution, as shown in Fig.3.13. The time-averaged flow pattern near the top surface, shown in Fig.3.14, matches well with the nail board measurements in Fig.3.7.Transient surface flow patterns separated by 1.2 sec show strong cross flow between the IR and the OR, which agrees with the transient surface flow patterns of the nail board measurements. According to the measurements, these surface flow variations often exceed ~200 % of the mean horizontal (x-velocity) component from NF to SEN.

3.5.3. Transient Velocity Variation

Instantaneous velocity magnitude histories are presented at 4 locations in the nozzle and 6 locations in the mold shown in Fig.3.15. As shown in Fig.3.16, points P-1 and P-2 in the nozzle have high velocity but small fluctuations, compared with P-3

and P-4 near the port, which have ~30 % smaller magnitude and large fluctuations (often reaching 100 % of the local mean velocity). The rotating swirl flow in the well-bottom region shown in Fig.3.11 causes flow instability, and high velocity fluctuations, and appears to worse with gas injection[12)] and is also influenced by the backflow region and the port-to-bore ratio.[34,35)] In the mold region, P-5 in the jet shows much higher velocity (~130 % higher) and corresponding higher fluctuations (~200 % bigger) than locations at the surface or deep in the strand, which all show fluctuations (based on standard deviations relative to the mean velocity) of ~10-30 %. Point P-8 (w/4 region) midway between the SEN and the NF shows the highest average velocity (~0.34 m/sec) at the surface with fluctuations of ~15 %. Computational modeling under-predicts the fluctuations, compared with the measured ~50 % fluctuations observed in the nail board dipping tests.

A power spectrum analysis of the velocity history was performed to evaluate the strength of different frequencies in the turbulent fluctuations, as shown in Fig.3.17. The power of the fluctuations is higher at P-4 in the nozzle port than at other points in the nozzle. All nozzle points show a similar profile, with power generally decreasing with increasing frequency. In the mold regions, the jet core at P-5 shows the highest power. Surface fluctuations decrease in power according to following sequence P-7, P-6, P-9, and P-8 (P-7 > P-6 > P-9 > P-8). This is significant, because point P-8 has the highest average velocity. This suggests that surface instability cannot be predicted by examining only averages of surface quantities. The strongest fluctuation powers are generally found at the lowest frequencies, which matches previous observations.[25)] Strong peaks are observed in the nozzle and mold with various frequencies between

0.1 and 10 Hz, including several characteristic frequencies of 0.5 - 2 Hz at the nozzle port and jet core, due to the interaction between the strong recirculation in the nozzle bottom and the natural turbulence. These frequency ranges correspond to the time intervals of periodic momentum fluctuations in the mold (0.1 to 10 sec) and in the nozzle (0.5 to 2 sec). Recall that these frequencies are caused by transients predicted over only ~10 sec in each symmetric half of the mold. Further consideration of longer time intervals and side-to-side variations would likely induce a wider frequency range of power at the mold surface.

3.5.4. Model Validation

The transient model of molten steel and argon gas using the coupled LES and Lagrangian DPM model was validated by comparing the predicted surface level and the surface velocity magnitude with the measurements from the nail board dipping tests. The predicted surface level profile h_{steel} is calculated from the surface pressure P_i, the average pressure P_{Avg} at the surface, and gravity acceleration g as follows[36)]

$$h_{steel} = \frac{P_i - P_{Avg}}{\rho g} \quad [3.20]$$

In this equation, slag density is not included because the slag layer experiences lifting while maintaining relatively constant thickness, rather than displacement, as observed in the measured slag motion in Figs.3.4 and 3.5. Details of this slag layer motion behavior will be discussed further in Chapter 4.

As shown in Fig.3.18(a), the predicted surface level profiles show remarkable agreement with the measured ones. The level near the narrow face and SEN are 6-8 mm higher than the minimum level found midway in between. Both also have large variations which show evidence of transient sloshing behavior. The measured variations increase towards the SEN and the NF and are much larger than the predictions. This is likely because the measurements cover 9 minutes but the predictions only cover 3 sec. During 3 sec, the LES model can capture only the high frequency and low amplitude components of the surface fluctuations. The low frequency and high amplitude wave motion observed in the measurements would require much longer modeling time. The measured sloshing frequency is far longer than 3 sec, so cannot be captured.

Surface velocity predicted by the LES model is compared with the measurements in Fig.3.18(b) and shows a reasonable match. The predictions are somewhat higher than the measurements, but fall within the range of the measurements. Again, it is likely that longer simulation time would produce an even better match for the velocity fluctuations. The surface velocity profile increases from less than 0.1m/s near the SEN and NF to a maximum of over 0.3 m/sec midway between. This maximum is within the optimal range of 0.2-0.5 m/sec suggested by

Kubota et al.[37] to avoid defects. Of greater concern is the variability and potential sloshing, which is investigated further in Chapter 4.

3.6. Summary and Conclusions

The transient fluid flow of molten steel and argon gas during steady continuous casting was investigated by employing the nail board dipping test and the LES coupled with the Lagrangian DPM.

- A series of nail board dipping tests captures level and velocity variations at the surface during nominally steady-state casting.
- The surface level profile of the molten steel shows time-variations induced by sloshing with high level fluctuations (up to ~8mm) near the SEN. In the quarter point region, located midway between the SEN and the NF, surface level is the lowest with the highest stability.
- The surface level of the liquid mold flux varies according to the lifting force produced by the molten steel motion below.
- Surface flow mostly goes towards to the SEN according to a classic double roll pattern in the mold. Transient asymmetric cross-flow between the IR and the OR mainly goes towards to the IR at the region near the OR and shows random variations (~200 % of mean horizontal velocity towards the SEN) near the IR.

- The chaotic fluctuations of the surface velocity are almost 50% of the average surface velocity magnitude across the entire mold width. This finding suggests that surface velocity fluctuations are very important to understand transient surface flow phenomena resulting in defects.
- Clockwise rotating flow pattern in the nozzle well is produced by the asymmetric opening area of the middle plate of the slide-gate. When clockwise rotating flow becomes weak, small counter-clockwise rotating flow is also induced in the nozzle well.
- Up-and-down wobbling of the jet flow induces variations of velocity magnitude and direction at the surface and changes the jet flow impingement point on the NF. The jet wobbling also influences argon gas distribution with time in the mold.
- Nozzle flow shows bigger velocity fluctuation with higher power in the well and port region.
- Jet flow with high velocity fluctuations becomes slower with increasing stability after impingement on the NF, resulting in slower velocity (~60 % lower) with smaller fluctuations (~70 % less) at the surface.
- Strong peaks are observed at several different frequencies between 0.1 and 10 Hz (0.1 to 10 sec), including several characteristic frequencies from 0.5-2 Hz (0.5-2 sec) at the nozzle port and jet core.
- LES coupled with Lagrangian DPM shows a very good quantitative match with the average surface profile and velocities from the nail board measurements, and the trends of their fluctuations. The model under-predicts the magnitude of the measured variations of both level and velocity, likely due to the short modeling time

(4.8 sec), which is insufficient to capture the important low-frequency fluctuations. Longer calculating time is needed to improve the model predictions of transient behavior.

3.7. Table and Figures

Table 3.1. Caster dimensions and process conditions

Caster Dimensions	
Nozzle bore diameter (inner/outer)	90 mm (at UTN top) to 80 mm (at bottom well) / 160 mm (at UTN top) to 140 mm (at SEN bottom)
Nozzle bottom well depth	19 mm
Nozzle port area	80 mm (width) × 85 mm (height)
Nozzle port angle	*2008: 52 to 35 down degree step angle at the top, 45 down degree angle at the bottom *2010: 35 down degree angle at both top and bottom
Mold thickness	250 mm
Mold width	1300 mm
Domain length	4648 mm (mold region: 3000 mm (below mold top))
Process Conditions	
Steel flow rate	552.5 LPM (3.9 tonne/min)
Casting speed	1.70 m/min (28.3 mm/sec)
Argon gas flow rate & volume fraction	9.2 SLPM (1 atm, 273 K); 33.0 LPM (1.87 atm, 1827 K) & 5.6 % (hot)
Submerged depth of nozzle	164 mm
Meniscus level below mold top	103 mm
EMBr current (both coils)	DC 300 A

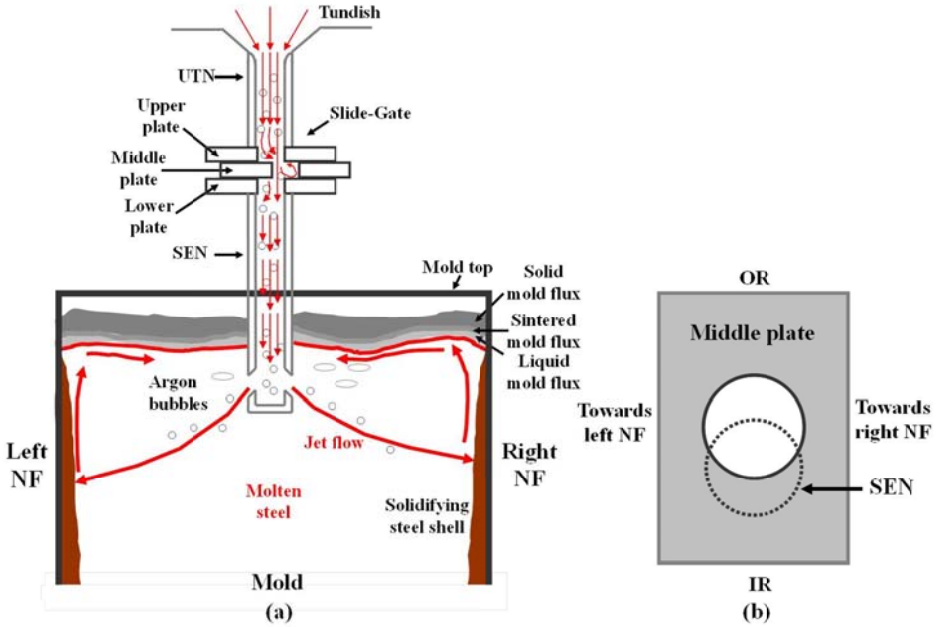

Fig. 3.1. (a) Schematic of slide-gate in steel slab continuous casting and (b) slide-gate middle plate on SEN

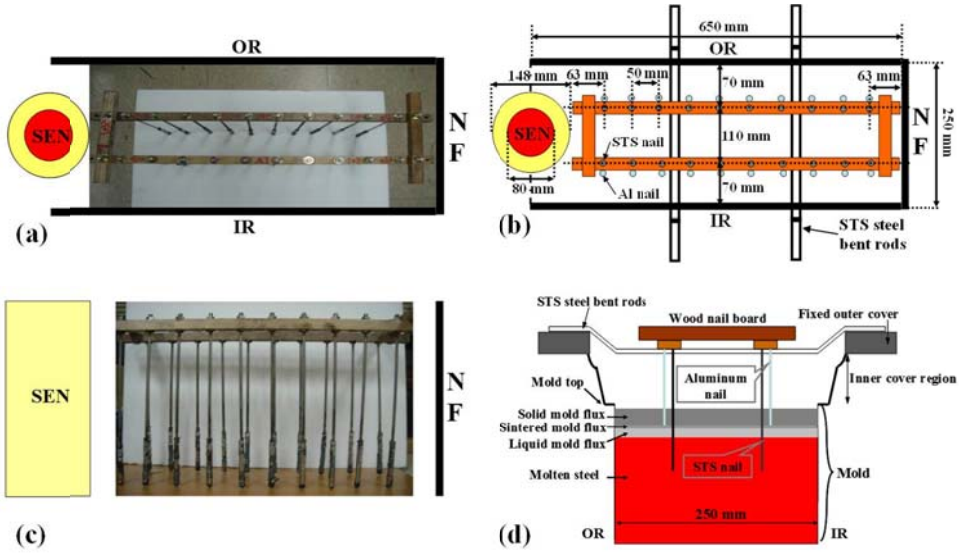

Fig. 3.2. Photos of the nail board: (a) top view, (c) front view and schematics of the nail board: (b) top view, (d) NF view

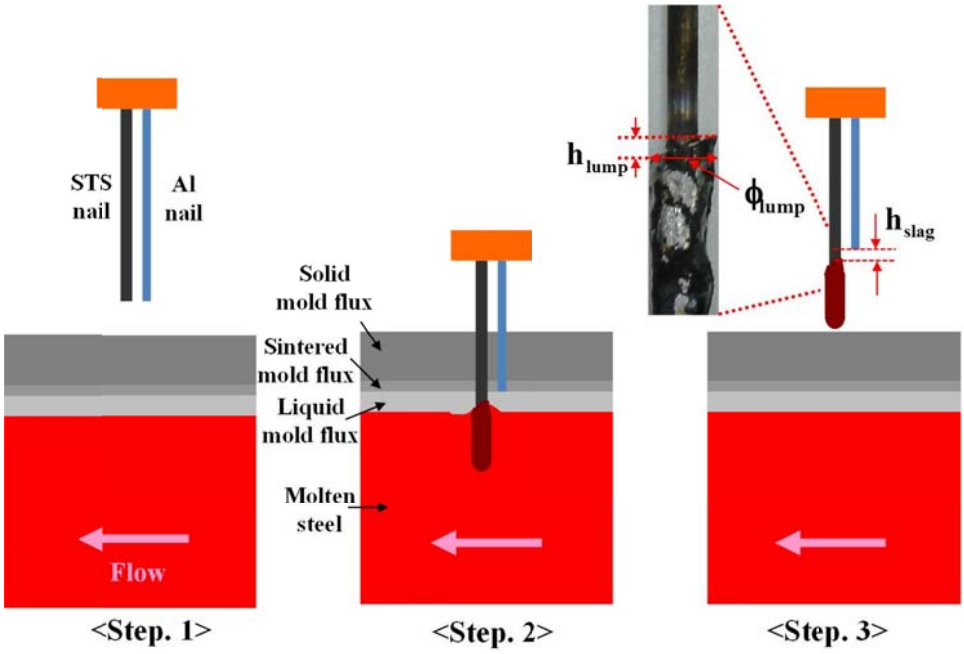

Fig.3.3. Nail board dipping method

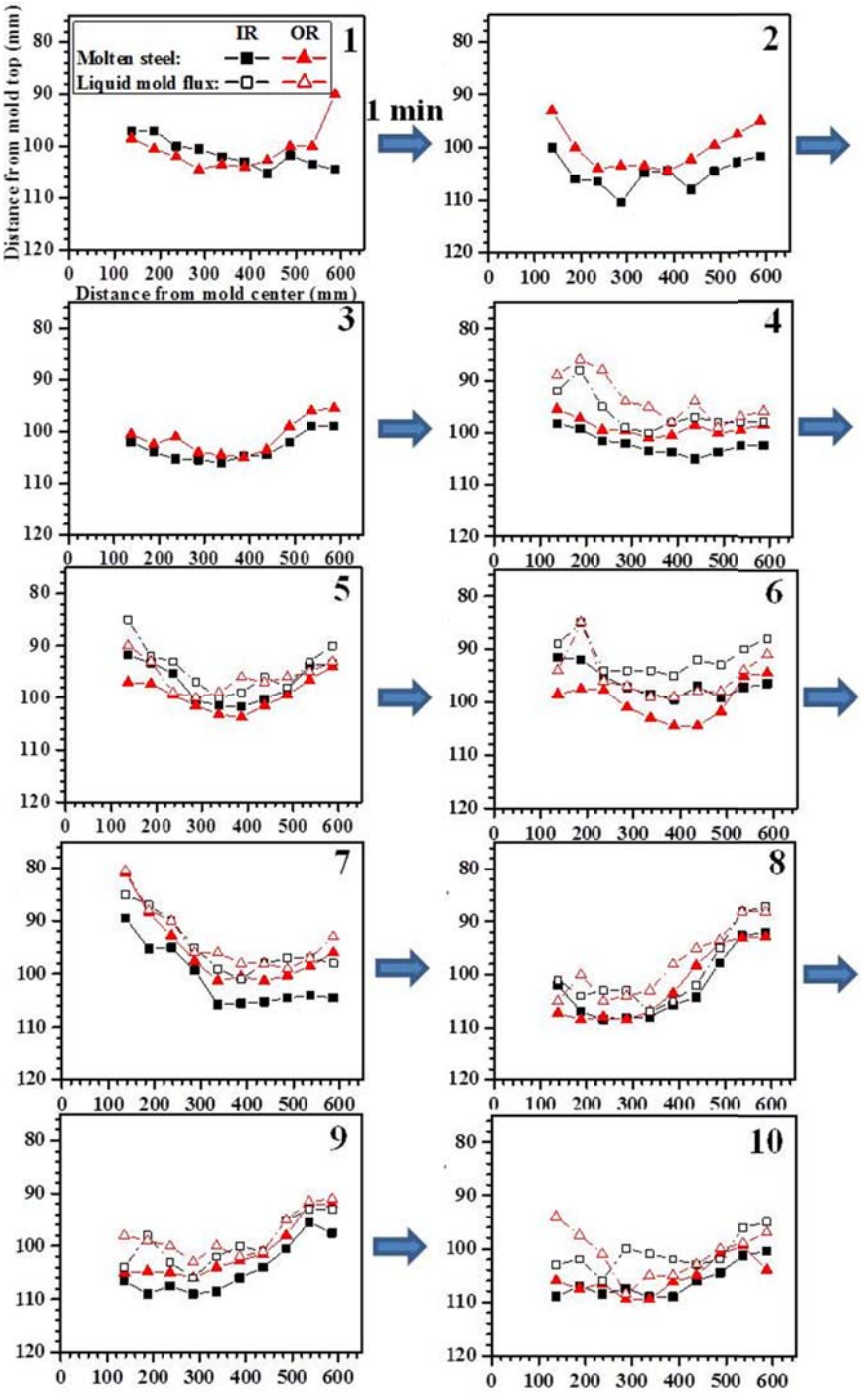

Fig.3.4. Transient variations of surface level profile by the nail board measurements

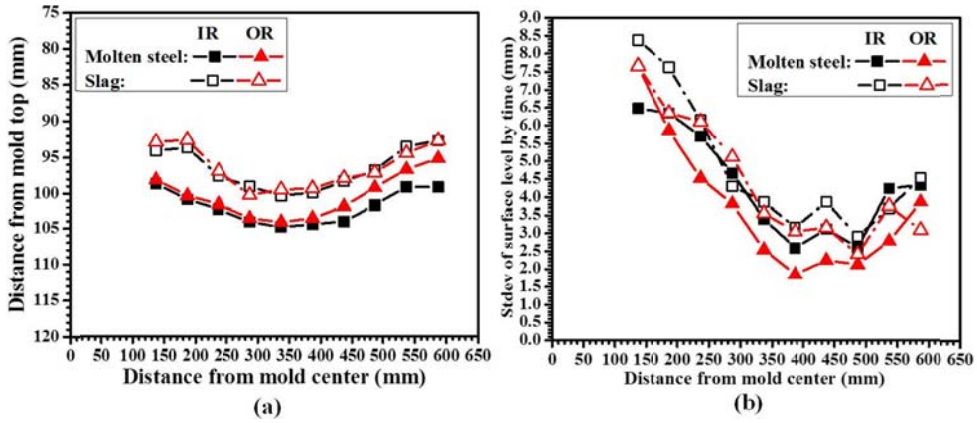

Fig.3.5. (a)Time-averaged surface level and (b) surface level fluctuation by the nail board measurements

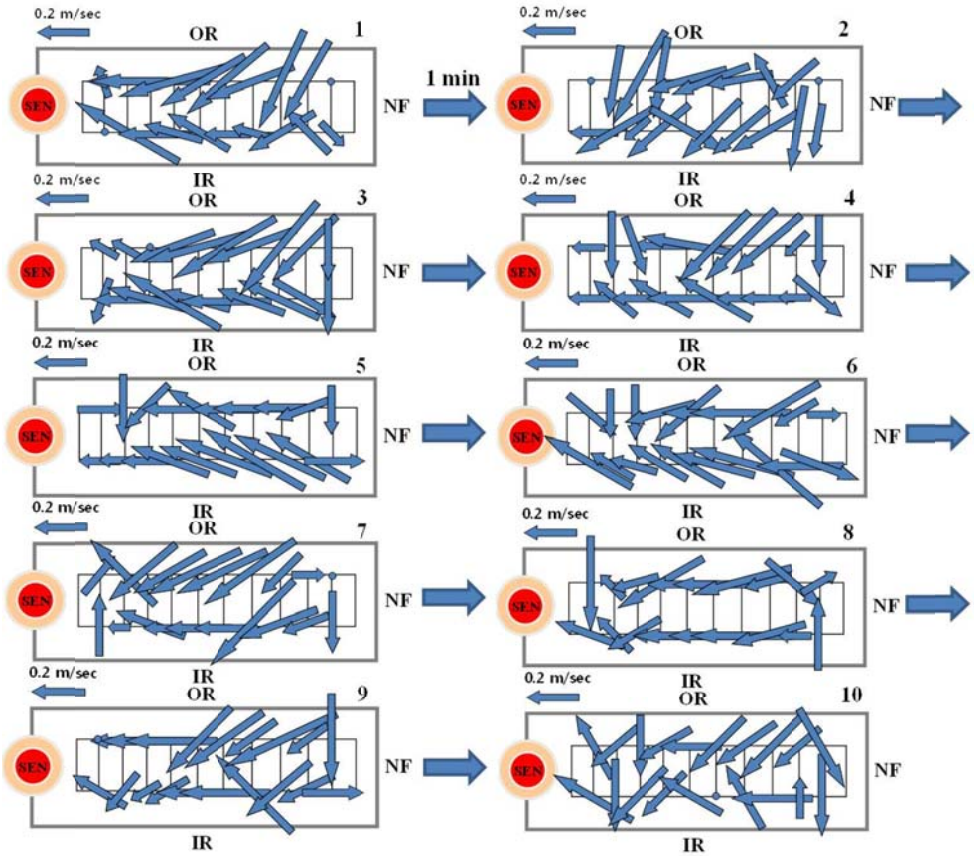

Fig. 3.6. Transient variations of surface flow pattern by the nail board measurements

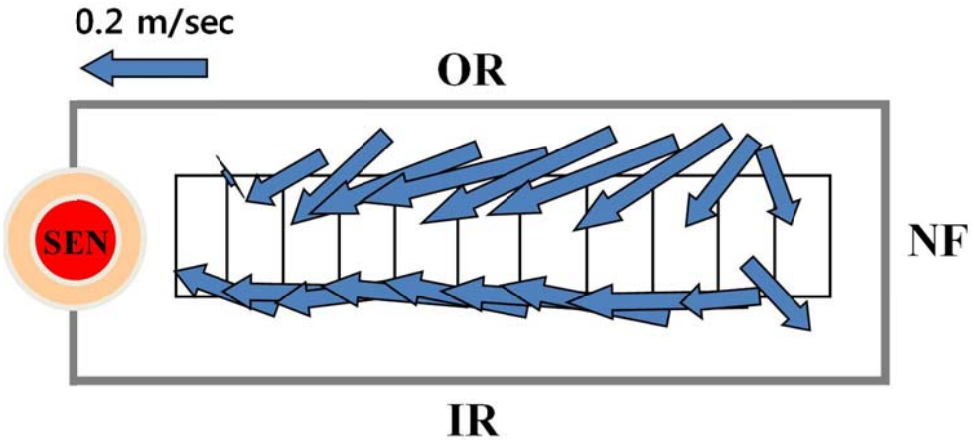

Fig. 3.7. Averaged surface flow pattern by the nail board measurements

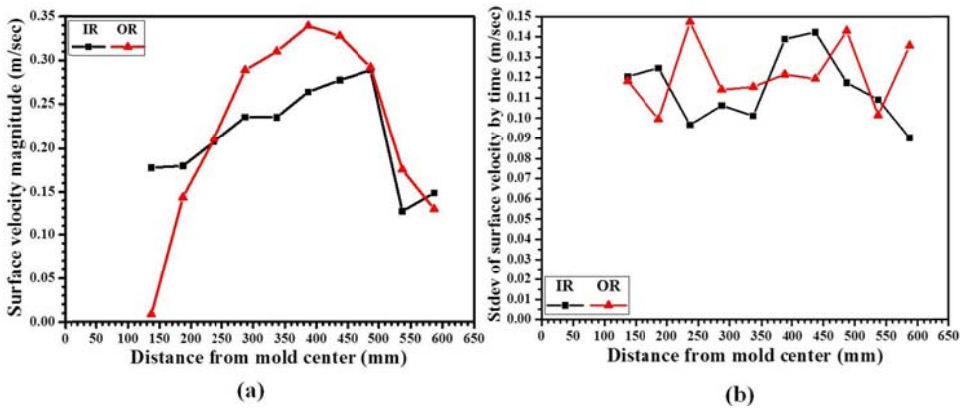

Fig. 3.8. (a) Time-averaged surface velocity and (b) surface velocity fluctuation by the nail board measurements

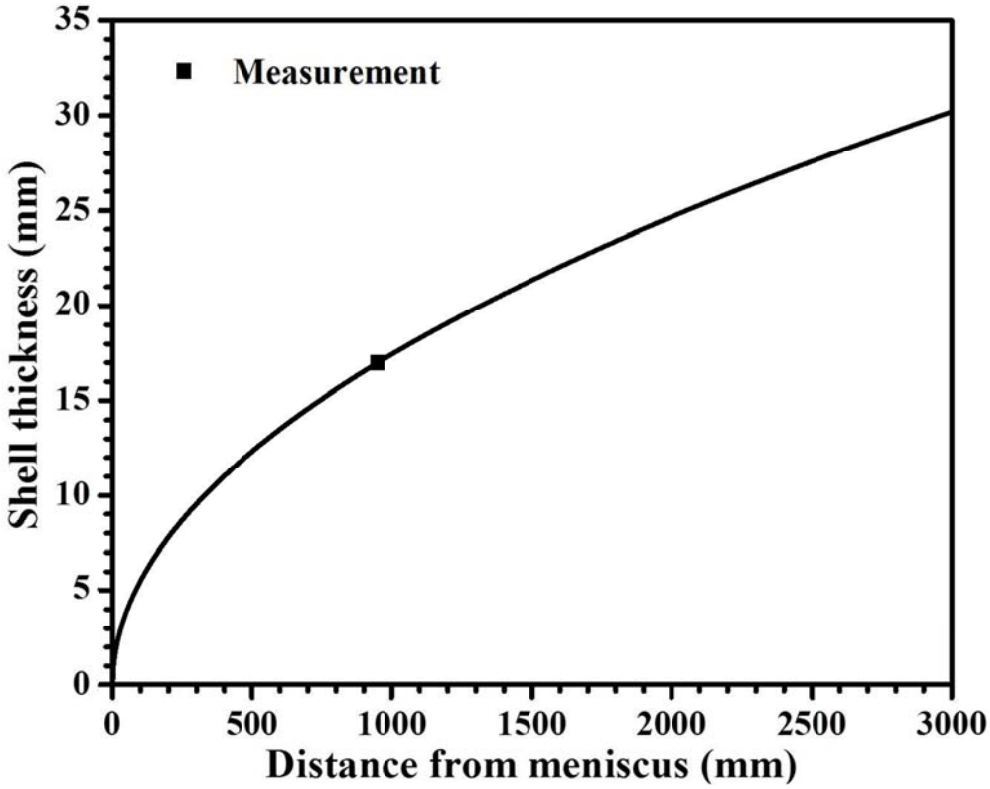

Fig.3.9. Steel shell thickness profile in the domain for the computational modeling

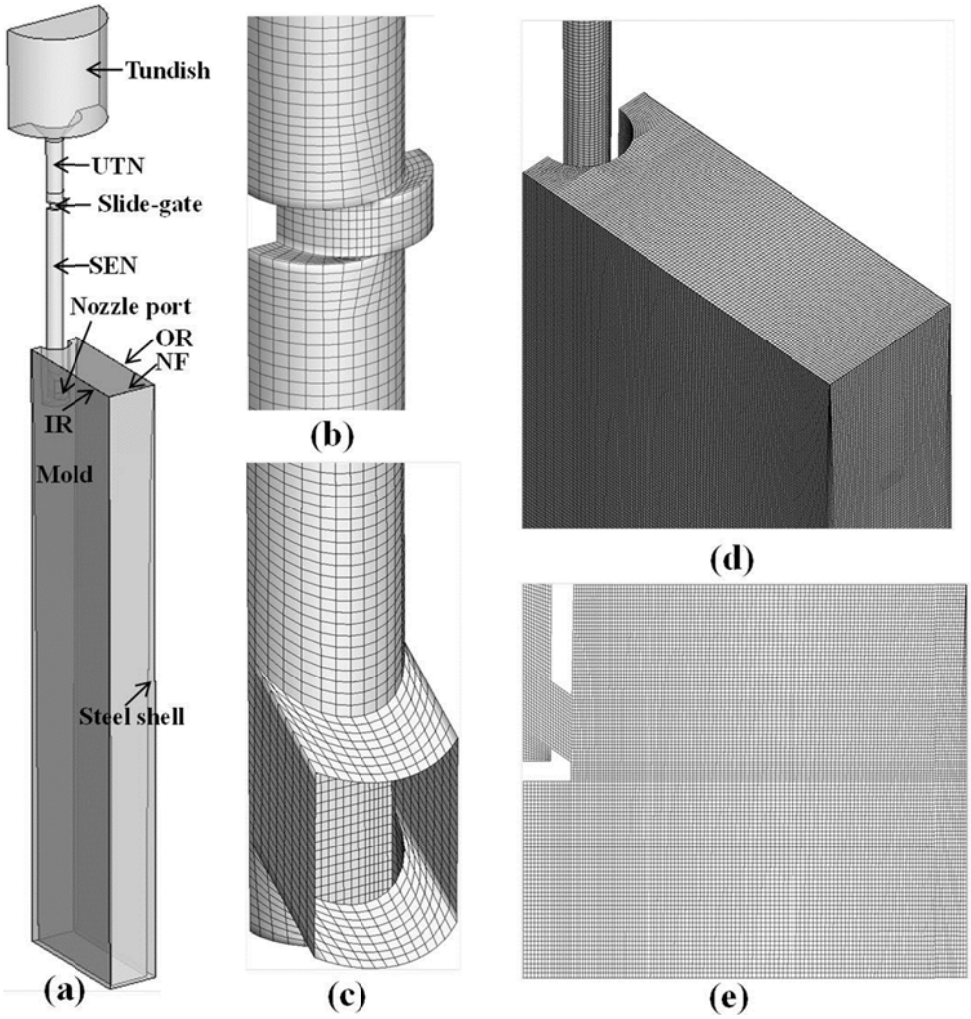

Fig.3.10. (a) Domain, (b) mesh for slide-gate, (c) mesh for nozzle port, (d) mesh for the mold and (e) center cross-section view of mesh of the computational modeling

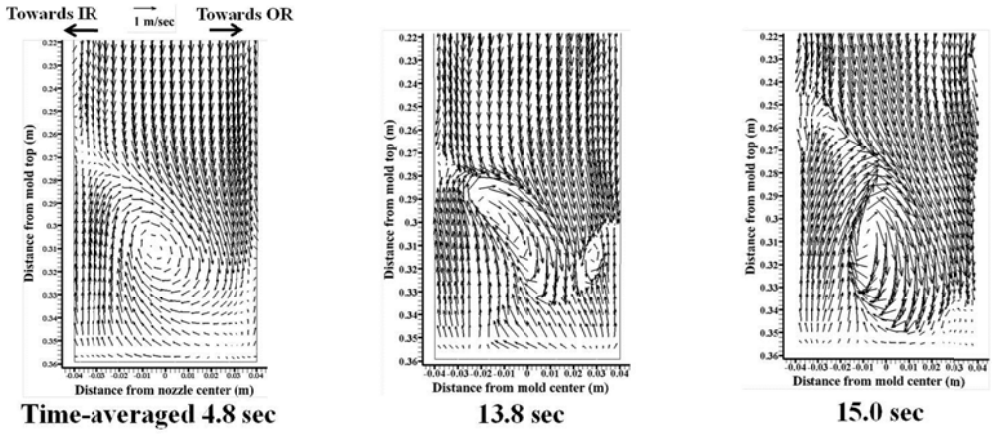

Fig.3.11. Time-averaged and instantaneous velocity magnitude in the nozzle bottom

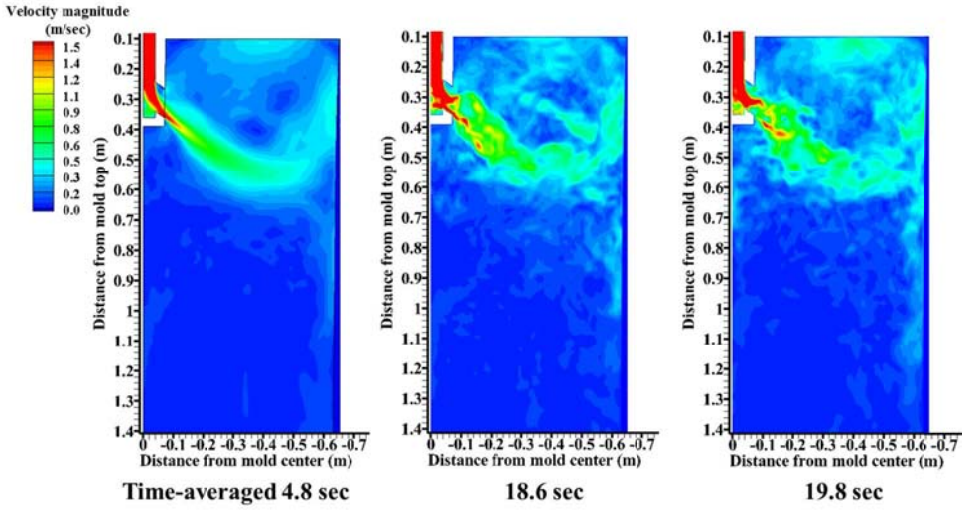

Fig.3.12. Time-averaged and instantaneous velocity magnitude in the mold

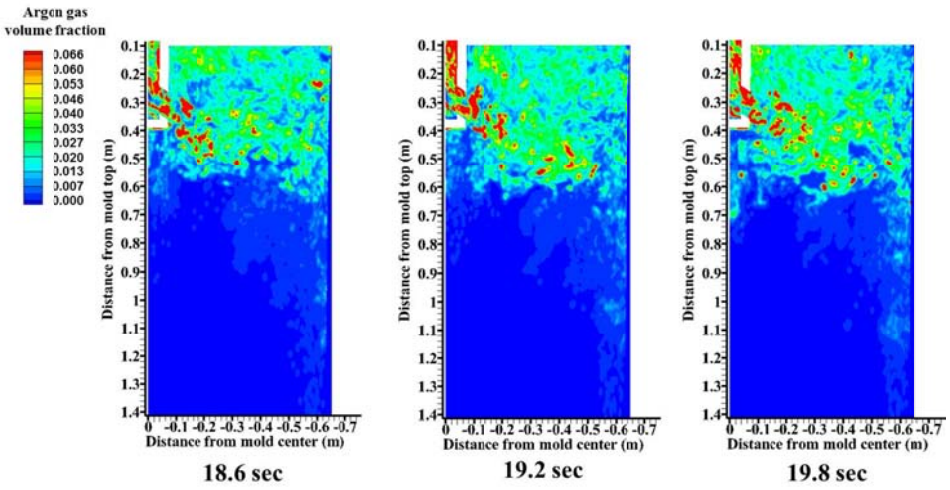

Fig.3.13. Instantaneous argon gas distributions in the mold

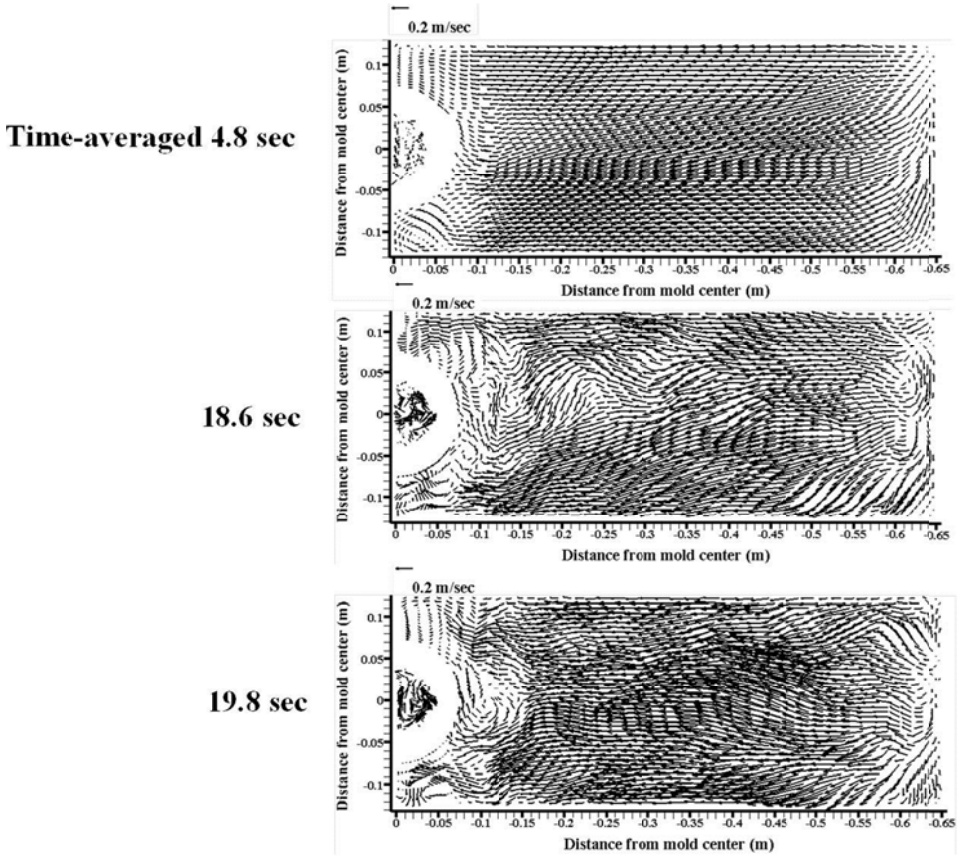

Fig.3.14. Time-averaged and instantaneous velocity magnitude at the surface

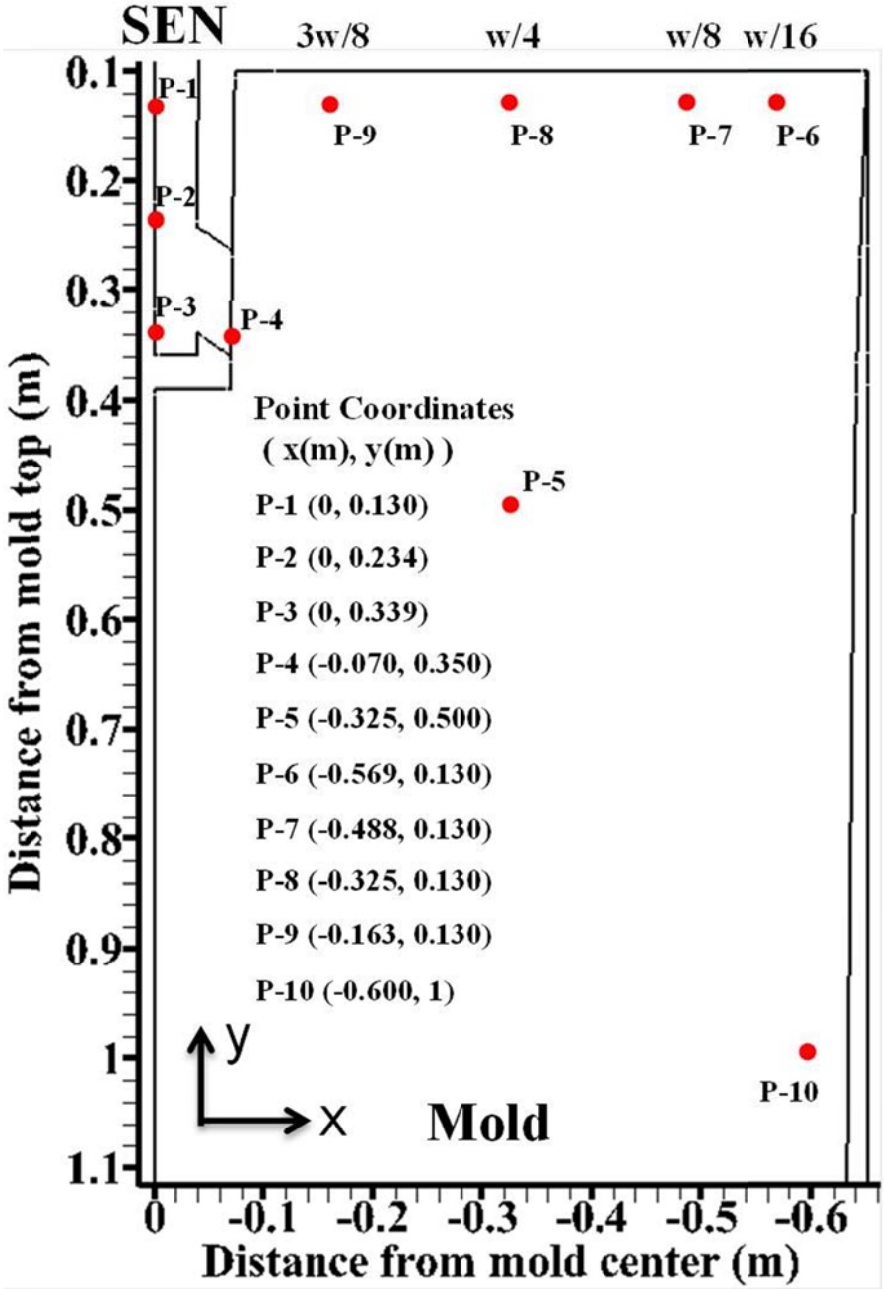

Fig.3.15. Location of points in the nozzle and mold center-middle plane

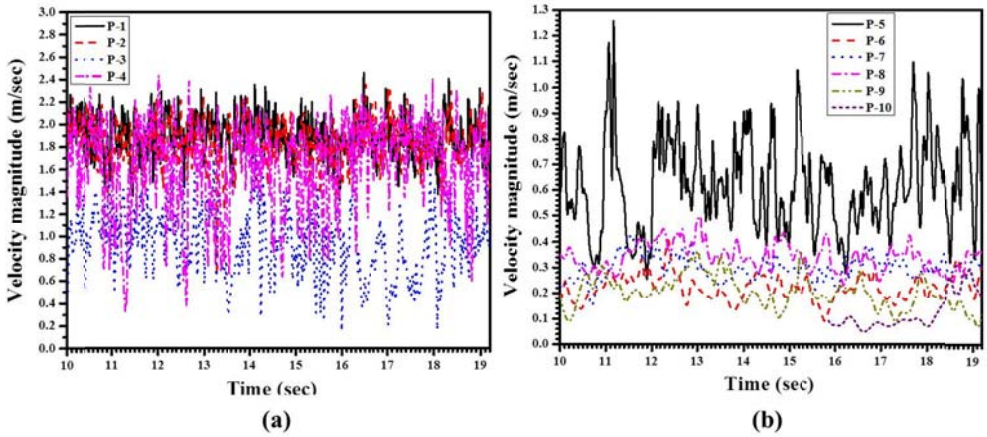

Fig.3.16. Transient velocity magnitude histories calculated (a) in the nozzle and (b) in the mold

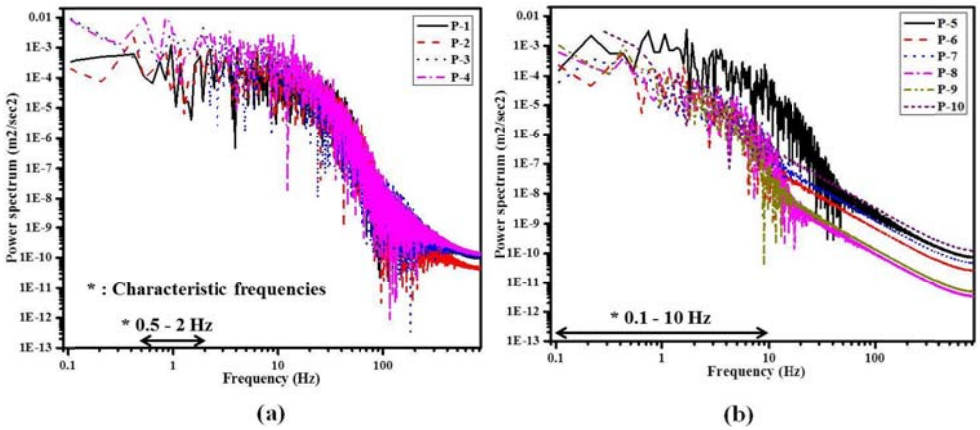

Fig.3.17. Power spectra calculated (a) in the nozzle and (b) in the mold

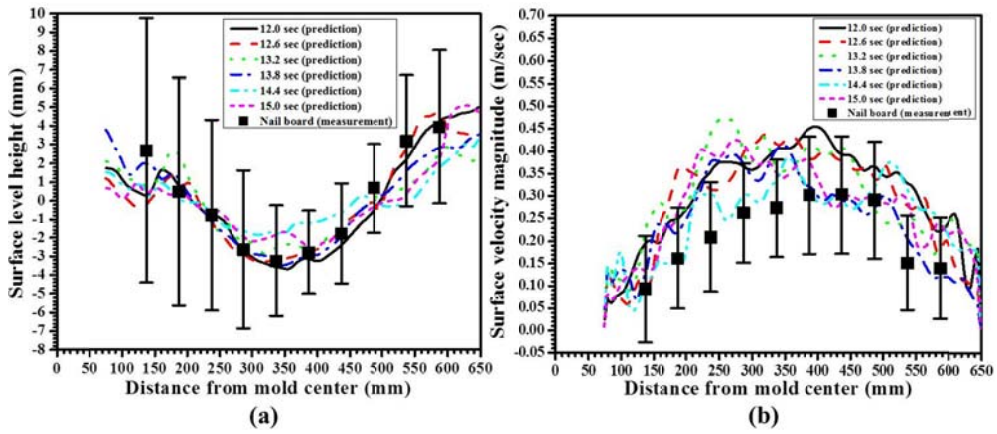

Fig.3.18. Comparison of (a) surface level and (b) surface velocity between the computational modeling and the measurement

3.8. References

1) N. Bessho, R. Yoda, and H. Yamasaki: Iron Steelmaker, Vol. 18 (1991), 39

2) P. Andrzejewski, K. –U. Kohler, and W. Pluschkeli: Steel Res., Vol. 3(1992), 242

3) H. Yu and M. Zhu: ISIJ Int., Vol. 48 (2008), 584

4) B. G. Thomas, X. Huang, and R. C. Sussman: Metallurgical and Materials Transaction B, Vol. 25B (1994), 527

5) Z. Wang, K. Mukai, and D. Izu: ISIJ Int., Vol. 39 (1999), 154

6) R. Sanchez-Perez, R. D. Morales, M. Diaz-Cruze, O. Olivares-Xometl, and J. P-Ramos: ISIJ Int., Vol. 43 (2003), 637

7) N. Kubo, T. Ishii, J. Kubota, and N. Aramaki: ISIJ Int, Vol. 42 (2002), 1251

8) V. Singh, S. K. Dash, J. S. Sunitha, S. K. Ajmani, and A. K. Das: ISIJ Int, Vol. 46 (2006), 210

9) M. Burty, M. De Santis, and M. Gesell: Revue de Metallurgie, Vol. 99(2002), 49

10) B. G. Thomas and L. Zhang: ISIJ Int, Vol. 41 (2001), 1181

11) T. Toh, H. Hasegawa and H. Harada: ISIJ Int, Vol. 41 (2001), 1245

12) H. Bai and B. G. Thomas: Metallurgical and Materials Transaction B, Vol. 32B (2001), 269

13) Y. Miki and S. Takeuchi: ISIJ Int, Vol. 43 (2003), 1548

14) Z. Liu, B. Li, M. Jiang, and F. Tsukihashi: ISIJ Int, Vol. 53 (2013), 484

15) S. Kunstreich, P. H. Dauby, S-K. Baek, and S-M. Lee: European Continuous Casting Conference, Nice, France, 2006, 20

16) P. H. Dauby: Revue de Metallurgie, Vol. 109(2012), 113

17) P.H. Dauby, W.H. Emling, and R. Sobolewski: Ironmaker and Steelmaker, Vol. 13 (1986), 28

18) R. McDavid: "Fluid Flow and Heat Transfer Behavior of Top-Surface Flux Layers in Steel Continuous Casting", Masters Thesis, University of Illinois at Urbana-Champaign, 1994.

19) R. Liu, J. Sengupta, D. Crosbie, S. Chung, M. Trinh, and B. Thomas: Proc. of TMS 2011, TMS, Warrendale, PA, USA, 2011

20) B. Rietow and B.G. Thomas: Proc. of AISTech 2008, Assoc. Iron Steel Technology, Warrendale, PA, USA, 2008

21) S. Cho, H. Lee, S. Kim, R. Chaudhary, B.G. Thomas, D. Lee, Y. Kim, W. Choi, S. Kim, and H. Kim: Proc. of TMS2011, TMS, Warrendale, PA, USA, 2011, 59

22) R. McDavid and B. G. Thomas: Metallurgical and Materials Transaction B, Vol. 4B (1996), 672

23) W. H. Emling, T. A. Waugaman, S. L. Feldbauer and A. W. Cramb: Proc. of 77th Steelmaking Conf., ISS, Warrendale, PA, USA, 1994, 371

24) H. Bai and B. G. Thomas: Metallurgical and Materials Transaction B, Vol. 32B (2001), 253

25) R. Chaudhary, G-G Lee, B. G. Thomas, and S-H. Kim: Metallurgical and Materials Transaction B, Vol. 39B (2008), 870

26) Yuan, Q., B. G. Thomas, and S. P. Vanka, Metallurgical and Materials Transactions B, Vol. 35B:4, 2004, pp. 685-702.

27) J. T. Kuo and G. B. Wallis: Int. J. Multiphase Flow, Vol. 14 (1988), 547

28) J. Aoki, L. Zhang, and B. G. Thomas: Proc. of 3rd International Congress on Science & Technology of Steelmaking, Assoc. Iron Steel Technology, Warrendale, PA, USA, 2005

29) ANSYS FLUENT 13.0-Theory Guide, ANSYS Inc.

30) H. Bai and B. G. Thomas: Metallurgical and Materials Transaction B, Vol. 32B (2001), 1143

31) G-G. Lee, B. G. Thomas, and S-H. Kim: Met. Mater. Int., Vol. 16 (2010), 501

32) X-W. Zhang, X-L. Jin, Y. Wang, K. Deng, and Z-M. Ren: ISIJ Int., Vol. 52 (2011), 581

33) F.M. White: Fluid Mechanics, 4th ed., Mc-Graw Hill, New York, NY, 1999.

34) T. Honeyands, J. Lucas, J. Chambers, and J. Herberston: 75th Steelmaking Conference, Iron Steel Soc, Warrendale, PA, USA, 1992, 451

35) F. M. Najjar, B. G. Thomas, and D. E. Hershey: Metallurgical and Materials Transaction B, Vol. 26B (1995), 749

36) G.A. Panaras, A. Theodorakakos, and G. Bergeles: Metallurgical and Materials Transaction B, Vol. 29B (1998), 1117

37) J. Kubota, K. Okimoto, A. Shirayama, and H. Murakami: Mold Operation for Quality and Productivity, edited by A.W. Cramb and E. Szekeres, Iron & Steel Society, Warrendale,Pa., 1991

Chapter 4: Effect of Double-Ruler Electro-Magnetic Braking (EMBr) on Transient Fluid Flow in the Nozzle and Mold of Continuous Steel Slab Casting

4.1. Introduction

To control surface level and velocity to avoid defects in steel slab continuous casting, many efforts have been made to optimize nozzle geometry and caster operating conditions including casting speed, submergence depth of the nozzle, mold width, argon gas injection, and Electro-Magnetic Forces (EMF), with the aim to achieve stable mold flow under nominally steady-state operation conditions. Application of a magnetic field to stabilize steel flow is an attractive method because the induced forces intrinsically adjust to flow variations. The field strength distribution depends on the magnet position(s), coil windings, and current. Electromagnetic systems are classified according to the type of field: static (DC current) or moving field (usually AC current). Static systems include local, single-ruler, and double-ruler (FC-Mold) Electro-Magnetic Braking (EMBr). Moving systems include Electro-Magnetic Level Stabilizer (EMLS), Electro-Magnetic Level Accelerator (EMLA), and Electro-Magnetic Rotating Stirrer (EMRS). EMBr is often used in slab continuous casting.

Many previous studies have investigated the average effect of EMBr on steady-state fluid flow in the mold.[1-11] For example, Cukierski and Thomas reported

that local EMBr usually decreases the surface velocity, depending on the submergence depth of the Submerged Entry Nozzle (SEN).[8] Wang and Zhang investigated the effects of local EMBr on the fluid flow, heat transfer, and transport of argon bubbles and inclusions in the mold.[9] Li et al. studied the effect of double-ruler EMBr with argon gas injection on mold flow[10] and biased flow induced by nozzle misalignment.[11] Only a few previous studies have investigated the effect of EMBr on transient flow and flow stability.[12-17] Timmel et al. found that single-ruler EMBr across the nozzle port induces significant jet fluctuations with non-conducting mold walls, and efficient damping of jet fluctuations in the conducting mold through measuring mold flow in a GaInSn physical model using Ultrasound Doppler Velocimetry (UDV).[12,13] Chaudhary et al. and Singh et al. performed Large Eddy Simulation (LES) of the GaInSn physical model and found that positioning a strong single-ruler EMBr across the nozzle port region induces large-scale and low-frequency flow variations.[14, 15] Singh et al. also observed that the single-ruler EMBr across the nozzle induces higher surface velocity, surface level, and surface level fluctuations by deflecting the jet flow upward, and the large scale jet wobbling induced by the EMBr with insulating wall is decreased with the EMBr with conducting wall.[15] These LES models predict that double-ruler EMBr causes surface velocity and velocity variations both decrease greatly.[14, 17]

Chapter 3 of this thesis presented models and experimental methods, and applied them to investigate two-phase transient flow.[18] In Chapter 4, the effect of double-ruler EMBr on transient flow in a conventional steel slab continuous caster is investigated using both computational modeling and plant measurements. Turbulent

flow in the nozzle and mold are computed by solving the standard Magneto-Hydro-Dynamics (MHD) flow equations. Plant measurements were conducted using an eddy current sensor as shown in Fig.4.1 and nail boards to quantify the effect of EMBr on surface level, surface flow, and the slag pool thickness. Furthermore, the effect of EMBr on stability of surface level and velocity is investigated. Details of the nozzle geometry and casting conditions were given in Table 3.1 of Chapter 3.[18)]

4.2. External Magnetic Field Distribution

The magnetic field was measured at 69 data points in the mold cavity as explained in Chapter 3.[18)] The magnetic field applied by the double-ruler EMBr is shown in Fig.4.2, and has high peaks in two regions: one centered just above the port, ~250 mm below mold top and the other below the nozzle port, ~750 mm below mold top. The magnetic field strength decreases significantly towards to the Narrow Face (NF). The measurements were extrapolated to produce the full 3D magnetic field distribution including the nozzle region and deep into the strand. The external magnetic field implemented to the computational model is visualized in Fig. 4.3.

4.3. Computational Model

A three-dimensional finite-volume computational model employing a Reynolds Averaged Navier-Stokes (RANS) approach using the standard $k-\varepsilon$ model coupled with a MHD model is applied to predict molten steel flow field in the nozzle and mold regions with the double-ruler EMBr. Steady-state single-phase flow was first predicted by the standard $k-\varepsilon$ model and then, the coupled MHD model system was applied to calculate the effect of the EMBr. The equations and boundary conditions were solved with the finite-volume method in ANSYS FLUENT, as described in Chapter 3.[18)]

4.3.1. MHD Model

A Lorentz force source term $\vec{F}_L$ is added to the RANS model Eqn.3.4 of Chapter 3,[18)] as given by

$$\vec{F}_L = \vec{j} \times \left(\vec{B}_0 + \vec{b}\right) \quad [4.1]$$

where $\vec{B}_0$ is the applied external magnetic field, $\vec{b}$ is the induced magnetic field, and $\vec{j}$ is induced current density, calculated by

$$\vec{j} = \frac{1}{\mu}\nabla \times \left(\vec{B}_0 + \vec{b}\right) \quad [4.2]$$

where μ is magnetic permeability of the molten steel and $\vec{b}$ is calculated from the magnetic induction equation:

$$\frac{\partial \vec{b}}{\partial t} + \left(\vec{u} \cdot \nabla\right)\vec{b} = \frac{1}{\mu\sigma}\nabla^2\vec{b} + \left[\left(\vec{B}_0 + \vec{b}\right)\cdot \nabla\right]\vec{u} - \left(\vec{u} \cdot \nabla\right)\vec{B}_0 \quad [4.3]$$

where σ is electrical conductivity of the molten steel, t is time, and $\vec{u}$ is the velocity vector field.

4.3.2. Domain, Mesh, Boundary Conditions, and Numerical Methods

The domain, mesh, boundary conditions, and numerical methods used here are the same, as given in Chapter 3, for the standard $k-\varepsilon$ model.[18)] Process parameters and material properties are provided in Table 4.1. Spatial discretization of the magnetic field terms used the second order upwind scheme. For the MHD model, three cases of wall conductivity for the domain boundary at the interface between the

molten steel and the solid steel shell region were considered: perfectly-conducting walls, perfectly-insulating walls, and a realistic treatment containing the conducting steel shell region as a solid zone added into the MHD model domain. The cases with perfectly-conducting walls and insulating walls had no steel shell region in the domain. The case with the realistic steel shell had an insulated exterior boundary, where the shell is surrounded by the non-conducting slag layer. The flow equations are solved only in the liquid zone, and the magnetic field equations were solved in both zones.

4.4. Model Results

To understand how the double-ruler EMBr affects surface level, velocity, and stability, the nozzle and mold flow phenomena were modeled without and with EMBr. Predicted level, velocity, and their fluctuations were compared with measurements.

4.4.1. Electromagnetic Phenomena

The steel flowing through the applied static magnetic field induces current which interacts with the field to generate a Lorentz force in the opposite direction of the flow. The interaction between the external magnetic field and the fluid flow in the nozzle region also induces a magnetic field, which is shown in Fig.4.4(a). This induced field comprises less than 1% of the total field. The current density

distribution produced by the total magnetic field is shown in Fig.4.4(b) and the Lorentz force is in Fig.4.4(c). The largest current and force is generated near the nozzle well-bottom and the upper-junction between nozzle bore and port, where the fastest flow is found. The force vectors in these regions are directed upwards, as shown in Fig.4.4(d). These forces greatly lessen variations in the swirl leaving the nozzle ports, while the swirl velocity magnitudes stay about the same.

In the mold region, the induced magnetic field, induced current density, and Lorentz force are presented in Fig.4.5 for the case with the realistic steel shell. High Lorentz forces are observed in two regions corresponding to high current density: near the nozzle port and near the NF 600mm below the mold top. The direction of the force opposes the flow of the jet, which agrees with theory. While also retaining mass and momentum balances, the result is deflection of the jet flow away from these two regions. For the conditions here, the easiest path for jet deflection is downward, towards the lower strand where the magnetic field is weaker, especially near the NF.

4.4.2. EMBr Effect on Nozzle Flow

As shown in Fig.4.6, the EMBr effect on the mean nozzle flow is small, even though the Lorentz force in the nozzle is strong. Predicted velocity contours without and with EMBr are very similar at these two center-plane cross sections (front and side views). The clockwise-rotating swirl flow produced by asymmetric opening area of the middle plate of the slide-gate[18)] exists both without and with the EMBr. However, the EMBr significantly affects the velocity fluctuations in the nozzle. As

shown in Fig.4.7, EMBr decreases the turbulent kinetic energy considerably at the well-bottom region, especially in the side-center view. This means that the rotating flow experiences fewer variations and changes in direction with EMBr.

4.4.3. EMBr Effect on Mold Flow

Velocity contours in the mold are compared in Fig.4.8. Without EMBr, the jet impinges high on the NF wall, induces strong flow upward along the NF, and results in high surface velocity. The strong flow near the meniscus could be detrimental in shearing off and entraining slag at the surface. With EMBr, however, jet flow in the mold is deflected downward by the strong Lorentz forces induced in the regions near the ports, and near the NF, 600mm below mold top. This produces a steeper downward angle of impingement on the NF, with less flow up the NF and consequently slower surface velocity. The strong downward mean flow along the NF with EMBr could be undesirable by taking argon bubbles and inclusions deep into the mold cavity, resulting in more internal defects. The jet flow is expected to have smaller turbulent kinetic energy with EMBr, especially towards the top surface, as shown in Fig.4.9. On the other hand, turbulent kinetic energy increases below the jet impingement point with EMBr, indicating more detrimental velocity variations in the lower strand. This finding differs from that of previous researchers[14, 17)], where both surface flow and downward flow greatly decrease with double-ruler EMBr. This is likely because the fields and casting conditions were different. Perhaps of greatest significance, the

magnetic fields of these previous studies were uniform across the mold width, which contrasts with the present measured fields, which decreased greatly towards the NF.

4.5. Model Validation

The predicted profiles of surface level, velocity magnitude and their fluctuations across the mold surface are compared with measurements from a series of nail-board dipping tests in Figs.4.10-4.11, both with and without EMBr. For both conditions, ten nail-board tests were taken during 9 minutes in the 2010 trial at both the Inside Radius (IR) and Outside Radius (OR), and averaged both temporally and spatially. The measurements without EMBr were shown in Chapter 3.[18] The measurements with EMBr (DC 300A to both rulers) are presented in Section 4.6. Both sets of measurements are compared here with model predictions along the center line of the top surface. In addition to the best predictions using the realistic solid shell, model predictions are also presented with perfectly-conducting and perfectly-insulated walls for comparison purposes.

The surface level profile was calculated from the surface pressure with Eqn 3.20 in Chapter 3.[18] The surface level fluctuation Δh was estimated from the turbulent kinetic energy k predicted by the standard $k-\varepsilon$ model as follows.[19]

$$\Delta h = \frac{k}{g} \quad [4.4]$$

where g is gravity acceleration. Similar to the assumption for surface level, slag density is not considered in Eq.4.4 because measurements presented here in Section 4.6 show that the slag is lifted more than it is displaced. Huang and Thomas found that surface level fluctuations predicted from Eqn 4.4 matched well with measurements.[19] Surface velocity fluctuations $\overline{|u_i'|}$ were calculated from the turbulent kinetic energy k by assuming that components in the 3 coordinate directions (i) are isotopic.

$$\overline{|u_i'|} = \sqrt{\frac{2}{3}k} \quad [4.5]$$

The surface level is flatter with EMBr, in both the predictions and the measurements, as shown in Fig.4.10(a). The surface level is highest near the NF, and lowest at the quarter point in both predictions and measurements, as found in previous work.[8,9,15,16] The predicted level is much flatter with EMBr, but the measured level profile variations decrease only near the SEN. The best prediction with the realistic steel shell matches well with the measurements with EMBr. Without EMBr, however,

the predictions significantly over-predict the extent of the variation in surface level profile across the width.

Surface level fluctuations decrease with EMBr in both the predictions and the measurements, but the magnitudes and variations differ, as shown in Fig.4.10(b). The predicted fluctuations are much smaller than the measurements, are smallest near the SEN, and decrease with EMBr along the entire surface. One the other hand, the measured fluctuations are much larger near the SEN and NF, likely due to sloshing waves, which are not possible to capture with the current model. Furthermore, the measured fluctuations decrease only from the quarter point to the SEN. Thus, the model Eq.4.4 is very crude and gives only a very rough estimate of level fluctuations.

Surface velocity decreases with EMBr, in both the predictions and the measurements, as shown in Fig.4.11(a). Surface velocity is a maximum at the quarter point, and decreases towards the SEN and NF. This trend and quantitative predictions with the realistic steel shell match well with the measurements with EMBr. The extent of the reduction of surface velocity caused by EMBr is over-predicted, however. The model predicts 43% reduction, but the measurements show only 17% reduction.

Surface velocity fluctuations with EMBr also decrease in both the predictions and the measurements, as shown in Fig.4.11(b). The model predictions again match well with the measurements with EMBr. However, the extent of the reduction with EMBr is slightly under-predicted. The model predicts 37 % reduction, but the measurement shows 43 % reduction.

The discrepancy in the model predictions without EMBr is likely due to the neglect of argon gas injection. It seems that 5.6 % argon gas volume injected in the real caster is not negligible, and has an important effect on the flow pattern and surface behavior, especially without EMBr. Future models should incorporate these multiphase flow effects. Further model improvements are also needed to make better predictions of transient phenomena, such as using LES models, and to incorporate gravity wave effects, such as using a free–surface model. Nevertheless, the simple model used here when considered together with the measurements provides important insights into understanding the effect of EMBr on nozzle, mold, and surface flow behavior.

Finally, the predictions with three different wall conductivity conditions (perfectly-conducting wall, -insulating wall, and realistic solid shell) are compared in Figs.4.10 and 4.11. The predictions of surface phenomena with the realistic solid shell fall between the less-appropriate cases of perfectly-insulating and -conducting walls.

4.6. Measurement Results

The effect of EMBr on surface level and surface velocity is quantified by measurements using an eddy-current sensor and nail board dipping tests in plant experiments conducted in 2008 and 2010 and explained in Chapter 3.[18)]

4.6.1. Surface Level (2010 Trial)

The transient time-history of surface level of the molten steel was measured by a standard commercial eddy current sensor at the "quarter point" located midway between the SEN and the NF both with and without EMBr. Signals were collected with 1 sec moving time averaging for 700 sec, as shown in Fig.4.12(a). Replotting of a 20 sec interval with expanded scale in Fig.4.12(b) shows the multiple frequencies of the level rises and drops. The average surface level is ~103 mm for both cases. The amplitude of the level variations is clearly greatly lowered with EMBr, as expected. Specifically, the level fluctuations drop from ~0.6 mm without EMBr to ~0.4 mm with EMBr.

Power spectrum analysis of the eddy-current surface level in Fig.4.12 is shown in Fig.4.13. Due to the data collection time interval of 1 sec, and total collection time of 700 sec, frequencies could be calculated only in the range from 0.5 Hz to 0.0014 Hz. A very strong maximum peak is observed at ~0.03 Hz, both with and without EMBr, which corresponds to periodic flow oscillations of ~35 sec. Without EMBr, many periodic level fluctuations are observed, including a peak at ~0.1 Hz for asymmetric flow past the SEN predicted using Honeyands and Herbertson's relation[20)]. With EMBr, the power of this maximum peak is decreased by ~50 % and other peaks in the power spectrum at frequencies > ~0.03 Hz, are decreased significantly with EMBr. Thus, EMBr stabilizes the surface level by dampening the fluctuations with higher frequencies > ~0.03 Hz.

To investigate the effect of EMBr on the surface level at other regions of the mold surface, the transient surface level profiles of the molten steel and the slag were measured by 10 nail board dipping tests taken over 9 minutes both with and without EMBr. As shown in Fig.4.14, both conditions show evidence of sloshing, where the level is alternatively higher and then lower near the SEN and near the NF. The steel level measured by the eddy current sensor is shown as a cross symbol, located at its actual position near the quarter point on the opposite side of the mold. The level at this location matches the nail board measurements well, which shows that the measurements on opposite sides of the mold are consistent and symmetrical. More significant is that the level at the eddy-current sensor location varies very little during this time, while the SEN and NF fluctuate greatly. This finding suggests that the eddy current sensor was positioned near a central "node" which best indicates the average level, and enables the level control system to maintain a stable average molten steel level. However, this finding confirms that the sensor is unable to detect the large level variations at other regions of the mold surface, such as due to sloshing. Furthermore, it should not be designed to detect them. The time-averaging of the sensor signal is another means that the sensor signal is stabilized and another reason that the large level variations are missed.

The time-averaged surface level with EMBr was slightly (~3 mm) higher than without EMBr, as shown in Fig.4.15(a). This effective change in the level set-point is inconsequential to quality, although it is interesting that this difference was not detected by the eddy-current sensor. This likely indicates variations in average level between the two sides of the mold.

The level fluctuations, as indicated by the standard deviation (stdev) of the level measurements, are greatly decreased with EMBr, especially near the SEN, as shown in Fig.4.15(b). Without EMBr, level fluctuations become severe towards the SEN, showing maximum average fluctuations of over 7 mm. On the other hand, with EMBr, the maximum average fluctuations are decreased to < 4 mm, and are more uniform across the mold width (average ~3.3 mm). Average level fluctuations across the mold width are ~4.0 mm without EMBr and ~3.0 mm with EMBr. The lowest fluctuations are found near the quarter point without EMBr and slightly off the quarter point with EMBr. This trend appears due to the sloshing mechanism, which is explained in the next section.

4.6.2. Surface Level and Sloshing (2008 Trial)

The transient time-history of surface level was measured with 6 nail board tests over 5 minutes in the 2008 trial under the same casting conditions as the 2010 trial in Fig.4.14, with and without EMBr. The surface levels at each location across the mold width, were averaged over inside and outside radius, and all plotted together in Fig.4.16. As in the 2010 trial, large periodic variations are observed both with and without EMBr, showing sloshing behavior. During the 5 minutes, the surface level shows at least two periodic oscillations without EMBr, and at least three with EMBr.

Considering the peak at 35 sec in the 2010 trial, the 6 snapshots measured in 2008 may have been taken over as many as 9 major oscillations in surface level.

The set-point (target) level for the eddy current sensor, shown as a cross-symbol, again shows significantly more stability at its quarter point location than the rest of the mold surface. The level variations are generally less with EMBr, both at this location, and across the mold width. The greatest fluctuations are found near the SEN without EMBr, as shown in Fig.4.16 (maximum difference > 25mm) and Fig.4.17 (standard deviation > 11mm). With EMBr, the fluctuations decrease to only 7mm near the SEN, but increase to 6mm near the NF, where they were < 2mm without EMBr.

A wave sloshing mechanism to explain the level variation behavior in 2008 is illustrated in Fig.4.18. Decreasing fluctuations observed from the SEN towards the NF without EMBr are consistent with the oscillating wave shape shown in Fig.4. 18(a). Minimum fluctuations at the quarter point, observed with EMBr, are consistent with the waves in Fig.4.18(b). Although this mechanism does not exactly match all of the 2010 trial measurements, it is consistent with the improvement in level stability with EMBr recorded at the quarter point by the eddy-current sensor (on average and at the 0.03 Hz peak), and with the lack of improvement at the NF nails. Thus, the eddy-current sensor should be positioned near stable nodes in the surface waves if possible, and the large detrimental sloshing variations should be measured independently, using nail boards tests.

4.6.3. Slag Layer Behavior (2010 Trial)

Slag level profiles were also measured via the nail board experiments, as explained in Chapter 3,[18] and show transient variations that correspond to the level variations of the molten steel. Sloshing of the slag level is observed both with and without EMBr in Figs.4.14 and 4.15(a). The surface level profile of the slag/powder interface generally follows the rising and falling of the steel/slag interface. The difference between these slag and steel levels indicates the thickness of the liquid slag layer. The relative lack of thickness variations suggests that the slag layer is simply lifted up and down by the steel motion.

To further investigate this phenomenon, the slag level is plotted as a function of the steel level in Fig.4.19. Both level heights are measured from the time average of the steel levels. Data were divided into three regions: SEN region 1 from 135 mm to 235 mm, Quarter-point region 2 from 235 mm to 485 mm, and NF region 3 from 485 mm to 585 mm from the mold center. Linear trend lines are plotted in each region, and included in Fig.4.19. The coefficients of these linear equations have physical meanings. The constant (y-intercept) means average thickness of the liquid slag layer, and the slope quantifies the slag motion. A slope of 0 means that slag motion is totally caused by displacement of some liquid slag by molten steel, as gravity causes the slag to flow down to where the steel level profile is lower in order to accommodate a local rise in the steel level. A slope of 1 means that the slag level is simply lifted up and down by the steel level motion, with no change in thickness.

The slag behavior in SEN region 1 shows mainly lifting, especially with EMBr. The other regions show a significant (up to 37%) displacement component of motion, especially with EMBr. The slag thickness in all regions is slightly larger with EMBr. Perhaps this is because smaller level fluctuations lead to shallower average oscillation mark depth, decreasing slag consumption slightly, and thus allowing a slightly thicker slag layer to build up.

The thinnest slag layer is found in the quarter-point region 2, both with and without EMBr. Thomas et al. found that temperature of the molten steel is expected to be highest near the midway point of a double-roll flow pattern.[21, 22] The finding here offers proof that higher steel temperature is not as effective as convective mixing due to steel flow in controlling the melting behavior of the slag and the slag layer thickness. Convection mixing inside the slag layer transports more heat to the powder and thereby increases melting rate and slag layer thickness.[23] This is also obvious via the theory that a few degrees of temperature variation across the surface is negligible relative to drop across slag layer over 1000 ^{o}C, so should theoretically have negligible effect on slag melting. The mixing mechanism is likely enhanced by higher steel surface velocity, level fluctuations, and interaction with argon gas leaving the surface.

4.6.4. Surface Flow Pattern and Velocity (2010 Trial)

Transient flow patterns and velocity profiles across the molten steel surface were calculated from the 10 nail board dipping tests for 9 minutes both with and without EMBr, as shown in Figs.4.20-4.22. The flow direction is given by a vector arrow with length proportional to the velocity magnitude. Flow is generally directed from the NF towards the SEN, according to a classic double-roll flow pattern. In addition, there is also a strong transient cross flow component, usually directed towards the inside radius, for both cases. Sometimes, the cross flow is towards the outside radius on one side, especially without EMBr. Very near the NF, surface flow goes slightly toward the NF, but is weaker with EMBr, suggesting there is less subsurface recirculating flow there with EMBr.

Average surface velocity profiles across the mold width are compared in Fig.4.22(a). The classic profile with maximum velocity near the quarter point is found both with and without EMBr, and have similar magnitudes. The highest average surface velocity magnitude is found near the outside radius for both cases. On average, surface flow is slightly slower (by ~17 %) with EMBr. Surface velocity fluctuations, as indicated by the standard deviation (stdev) of the velocity measurements, are smaller (by ~43 %) with EMBr, as shown in Fig.4.22(b). This finding suggests that use of the double-ruler EMBr for the conditions of this study may help to reduce defects caused by surface flow instability.

4.7. Summary and Conclusions

The effect of double-ruler EMBr on transient flow during steady continuous casting was investigated by applying a standard $k-\varepsilon$ RANS model coupled with MHD equations and plant measurements using an eddy-current sensor and nail boards.

- The double-ruler "FC-Mold" EMBr studied here creates two regions of equally-strong magnetic field across the mold width: one centered just above the port and the other centered farther below the nozzle port. Both peaks in the measured field significantly decrease in strength towards the NF.
- With EMBr, turbulent kinetic energy is decreased in the nozzle well region, where rotating swirl flow is caused by the asymmetric open area at the slide-gate.
- Jet flow with this EMBr configuration is deflected downward, resulting in flatter surface level and slower surface velocity with less level fluctuations.
- With EMBr, the predicted surface level profile, velocity profile, surface level fluctuations, and velocity fluctuations all match surprisingly well with the measurements, considering the simplified model. Without EMBr, the model over-predicts the level profile variations and the surface velocities, and underpredicts the fluctuations.
- The surface level fluctuations measured by an eddy-current sensor of 0.6 mm (Without EMBr) and 0.4 mm (With EMBr) are much smaller than those by the nail board dipping tests, of 4.0 mm (Without EMBr) and 3.0 mm (With EMBr). This is likely because the eddy-current sensor is positioned over a near-stationary node in the waves, and its signals are filtered (1 sec time-average) according to standard industry practice, to miss the real transient fluctuations which are captured by the nail board tests.

- Both with and without EMBr, the surface level experiences periodic variations which show sloshing between the SEN and the NF, as indicated by sequences of nail board dipping tests. The sloshing is high amplitude (up to 8mm) and low frequency / long period (up to 1 minute).
- Both with and without EMBr, a characteristic frequency peak of the surface level variations is observed at ~0.03 Hz (~35 sec) at the "quarter point" located midway between the SEN and the NF.
- EMBr increases surface level stability, specifically by decreasing the severe level fluctuations near the SEN by ~50%, and lowering the peaks in the level fluctuation power spectrum.
- Motion of the steel-slag interface level mainly causes lifting of the slag layers, especially near the SEN. Elsewhere, the slag layers are partially displaced by the steel, due to flow that causes the liquid layer to become slightly thinner, especially near the NF, and with EMBr.
- The slag pool is slightly thicker with EMBr.
- The surface flow with EMBr shows more biased cross-flow pattern from outside to inside radius.
- EMBr produced ~20 % lower surface velocities (Without EMBr: 0.22 m/sec, With EMBr: 0.18 m/sec) with ~40 % less velocity variations (Without EMBr: 0.12 m/sec , With EMBr: 0.07 m/sec).
- Double-ruler EMBr may help to reduce defects caused by surface instability if used properly.

4.8. Table and Figures

Table 4.1. Process parameters

Casting speed	1.7 m/sec
Domain width	650 mm
Domain thickness	250 mm
Domain length	4648 mm (mold region: 3000 mm)
Molten steel density	7000 kg/m^3
Molten steel visocity	0.0067 $\mathrm{kg}/\mathrm{m\ s}$
Electrical conductivity of molten steel	$714{,}000\ (\Omega\mathrm{m})^{-1}$
Electrical conductivity of solid shell	$787{,}000\ (\Omega\mathrm{m})^{-1}$

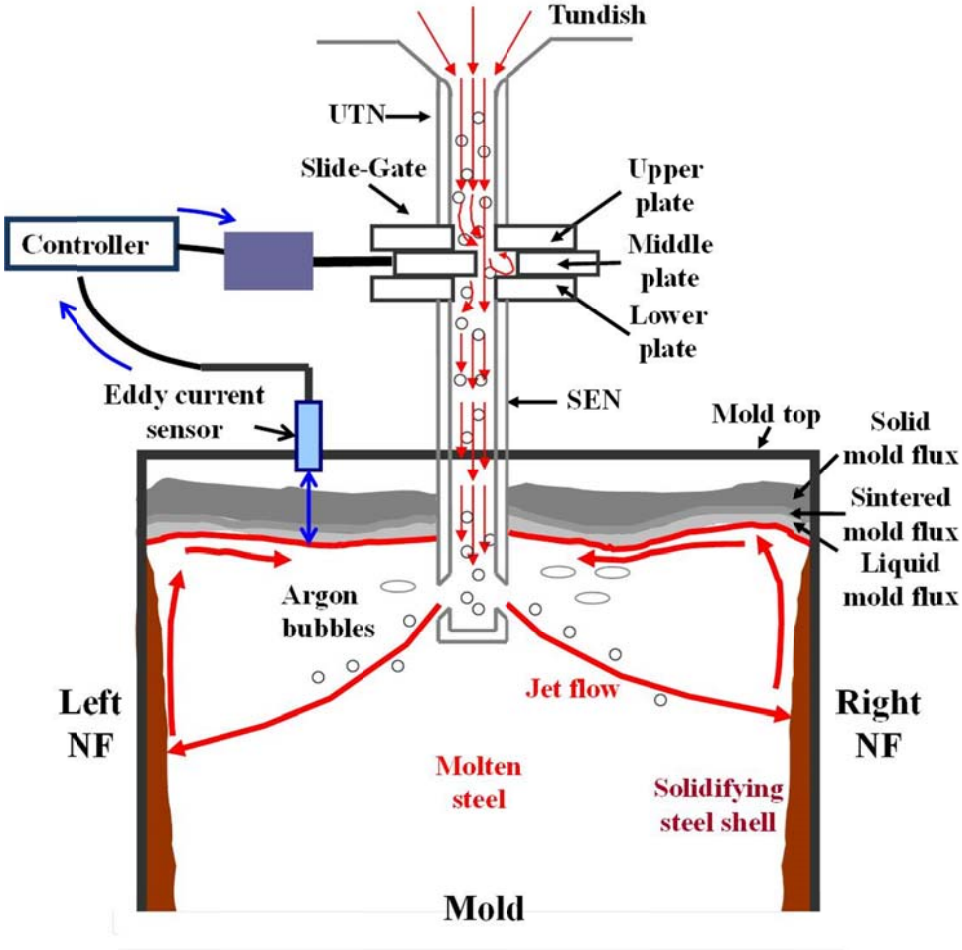

Fig.4.1. Position of eddy current sensor in the mold

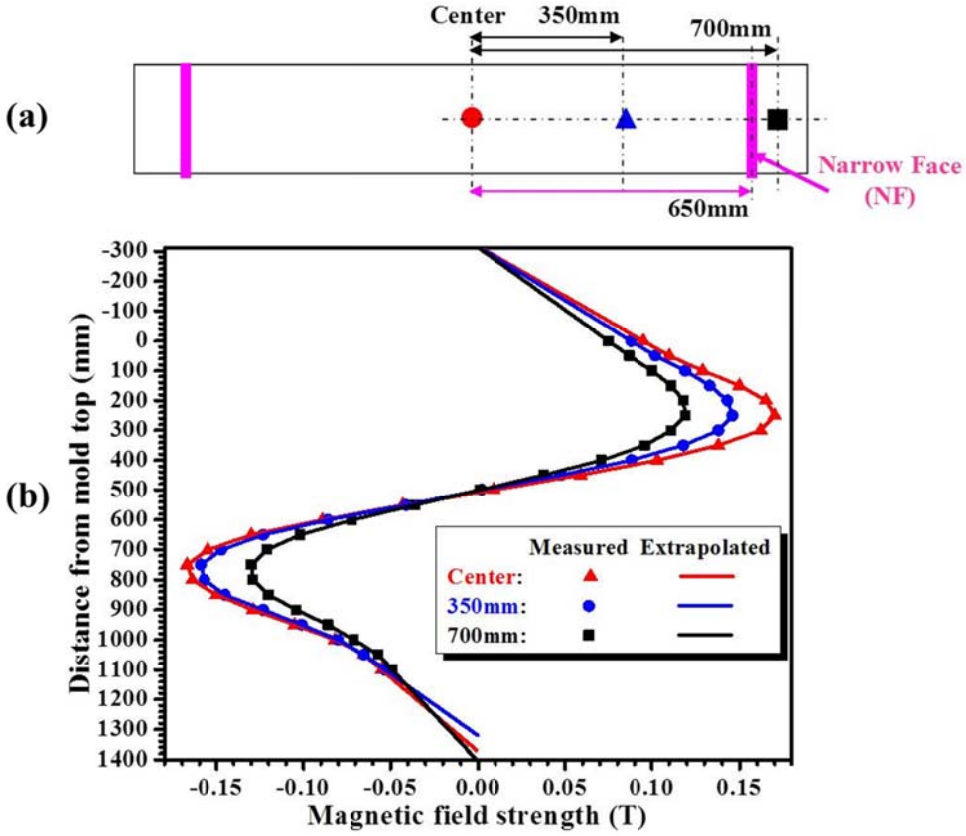

Fig.4.2. External EMBr field: (a) locations measured, and (b) magnetic field profiles

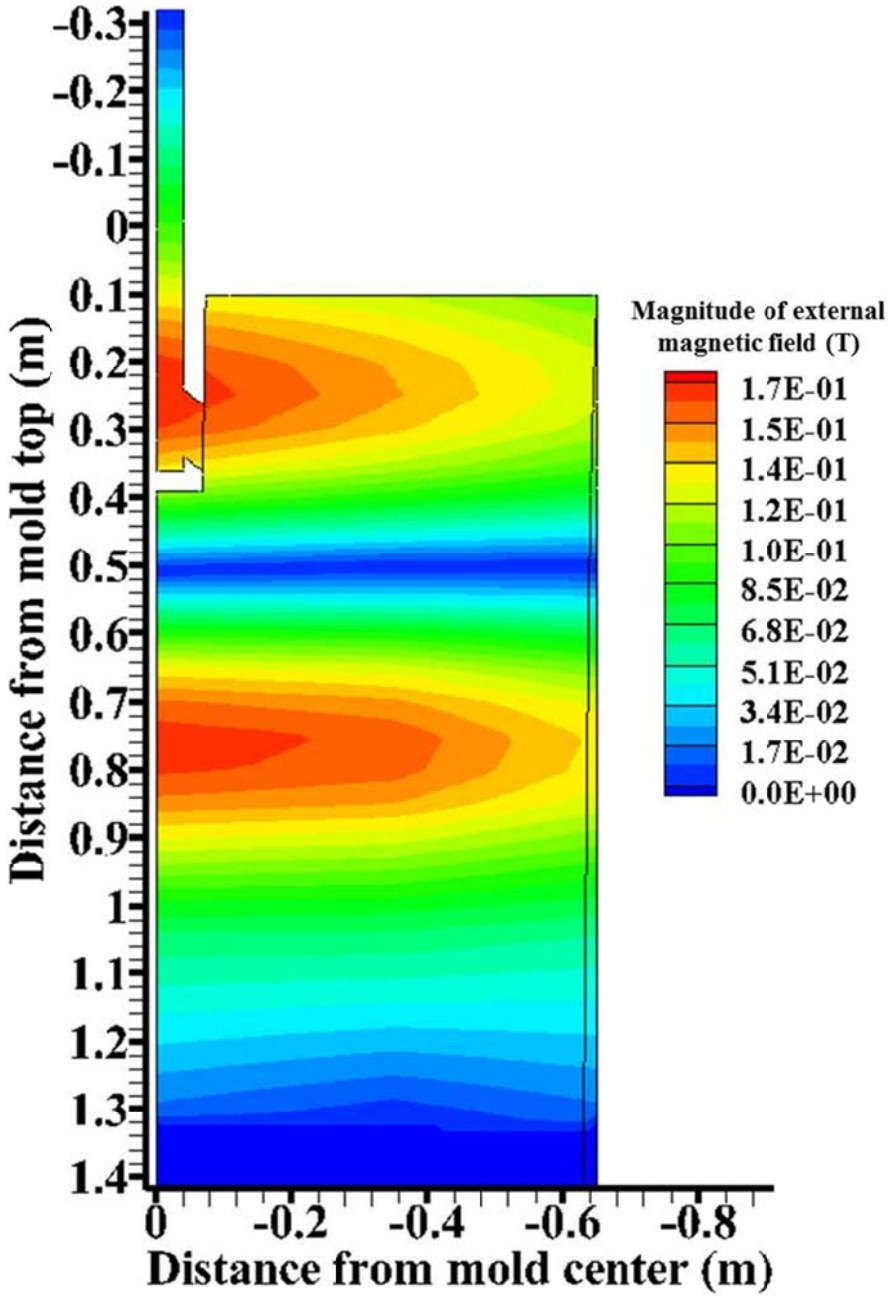

Fig.4.3. External magnetic field magnitude distribution in the nozzle and mold

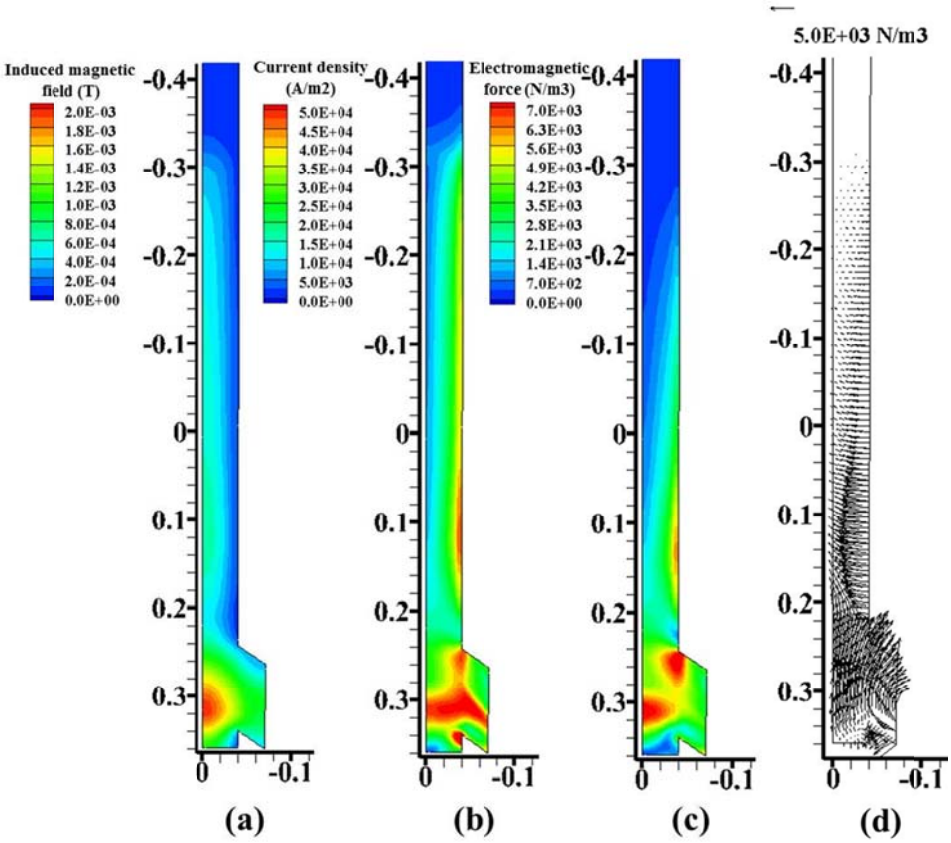

Fig.4.4. (a) Induced magnetic field, (b) current density, (c) electromagnetic force, and (d) electromagnetic force vector distributions in the nozzle

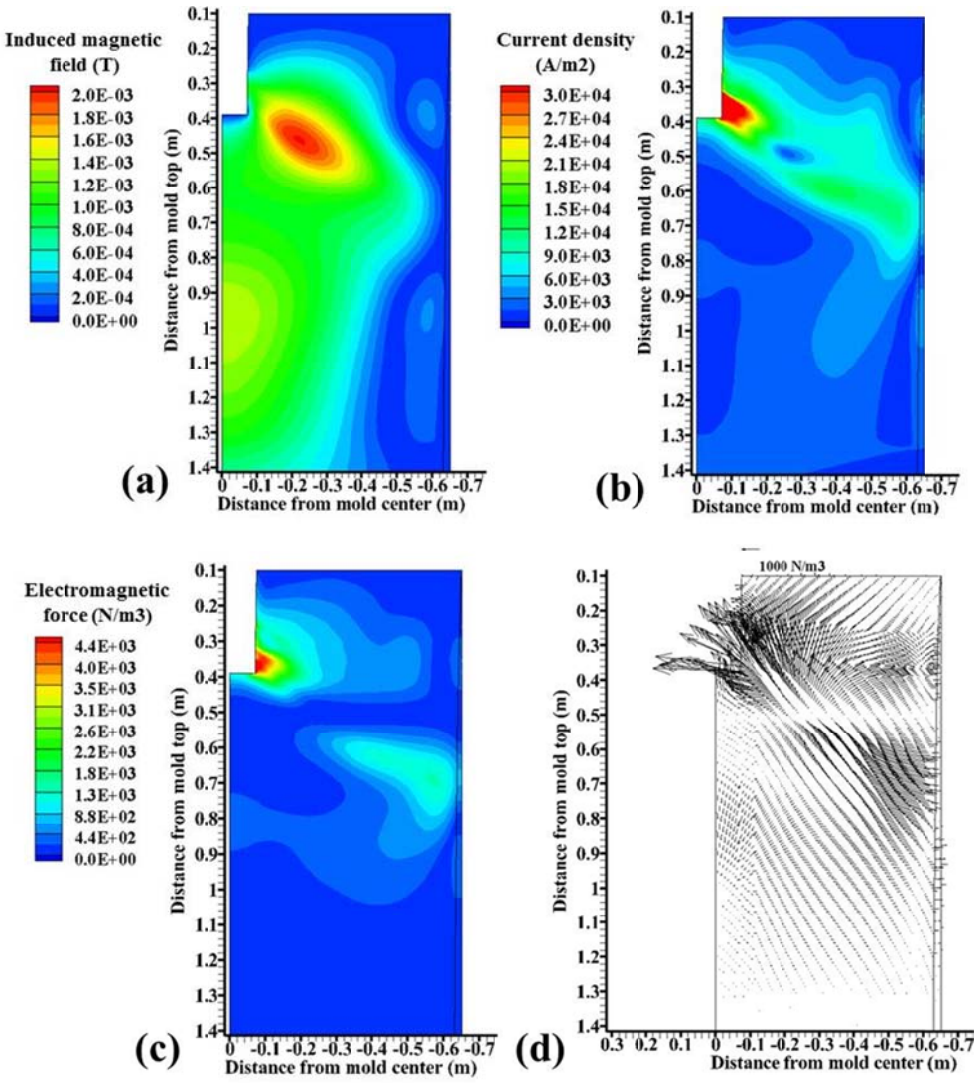

Fig.4.5. (a) Induced magnetic field, (b) current density, (c) electromagnetic field, and (d) electromagnetic force vector distributions in the mold

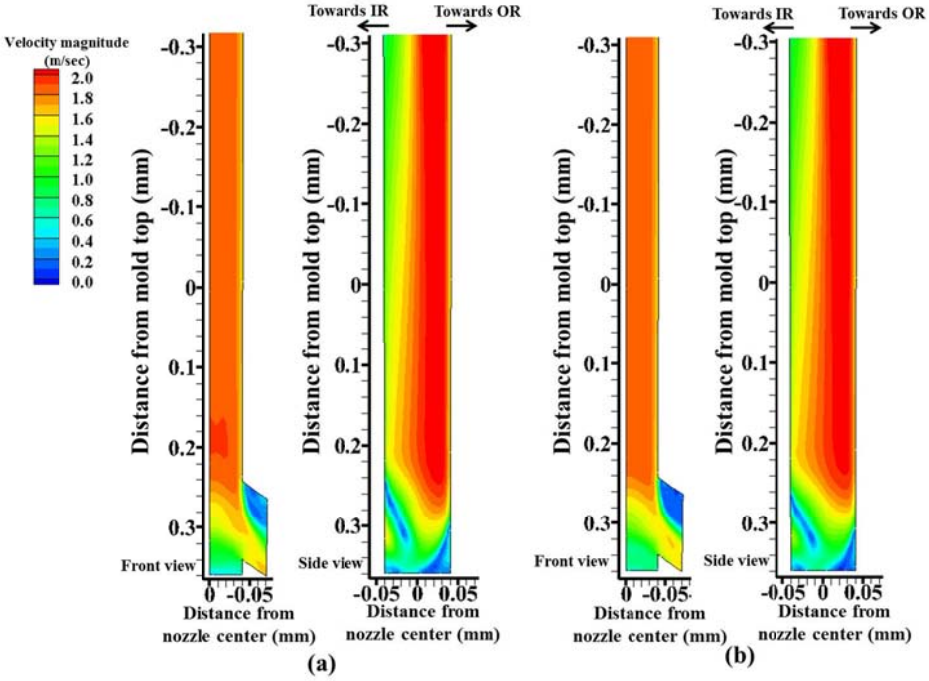

Fig.4.6. Predicted velocity magnitude in the nozzle (a) without EMBr and (b) with EMBr

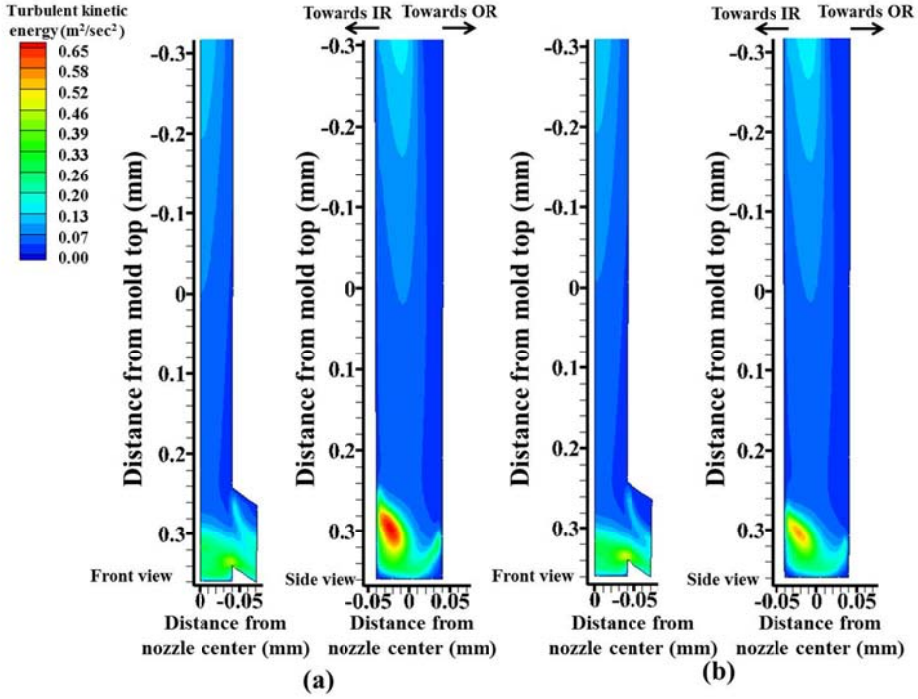

Fig.4.7. Turbulent kinetic energy in the nozzle (a) without EMBr and (b) with EMBr

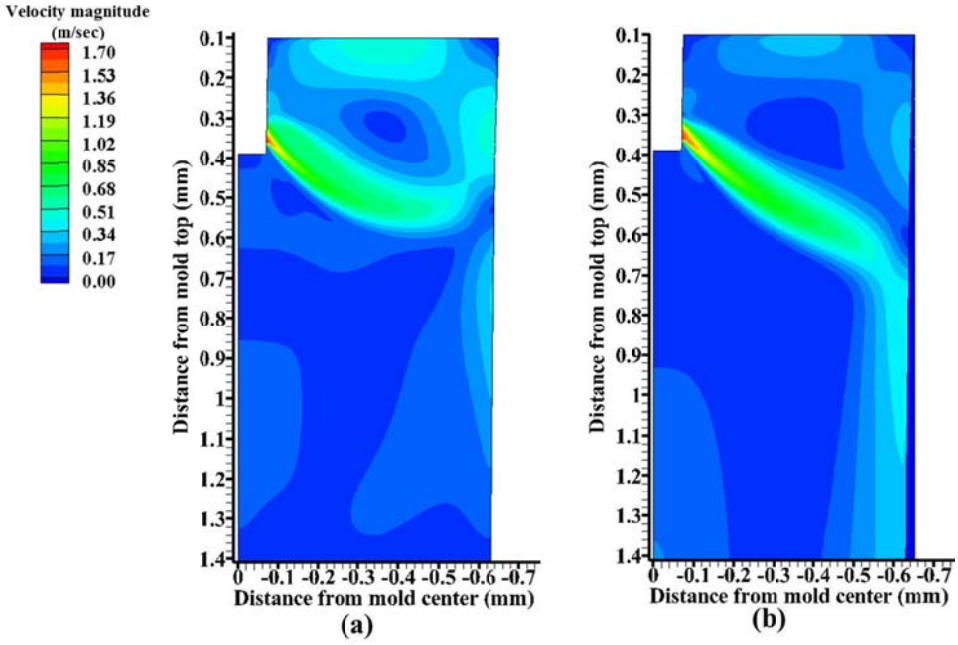

Fig.4.8. Predicted velocity magnitude on center-middle plane in the mold (a) without EMBr and (b) with EMBr including steel shell

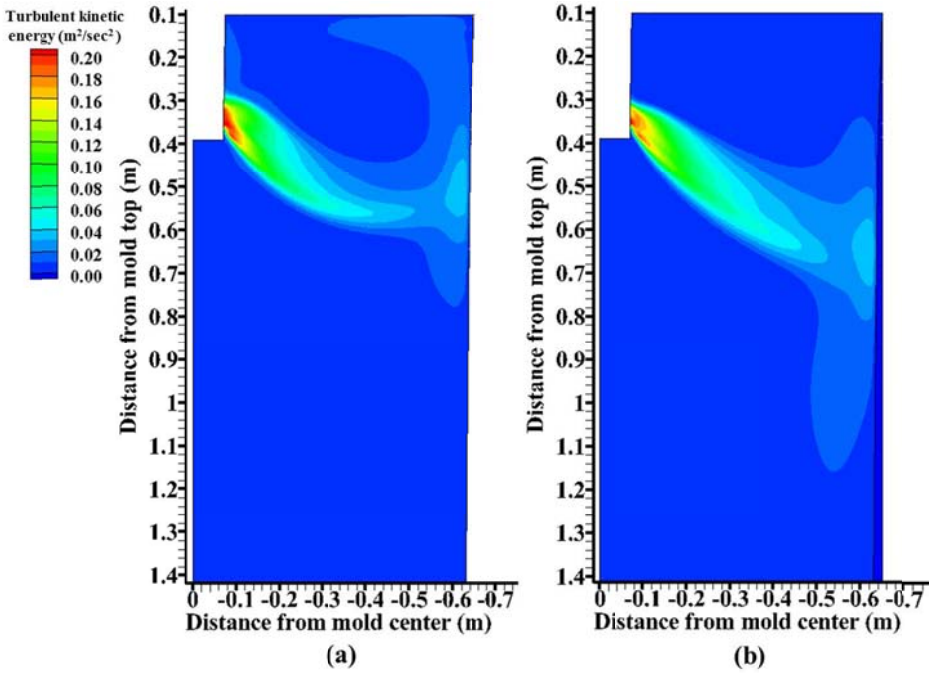

Fig.4.9. Turbulent kinetic energy predicted **i**n mold mid-plane (a) without EMBr and (b) with EMBr including steel shell

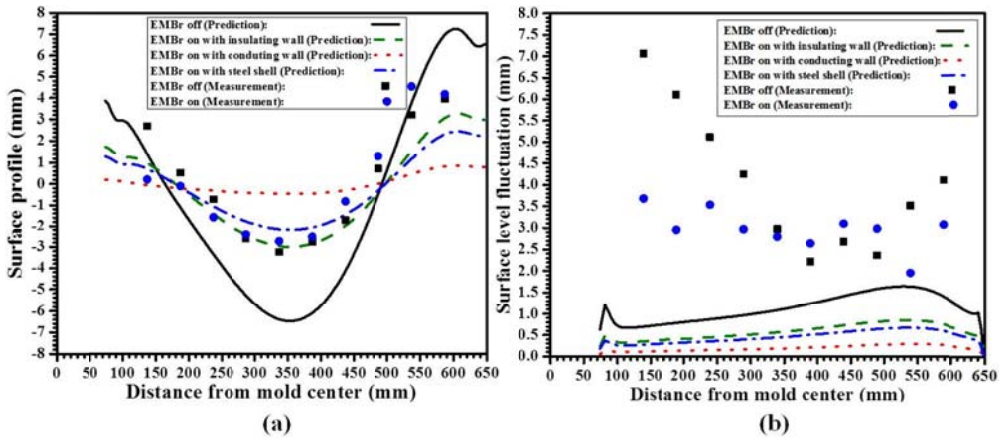

Fig.4.10. EMBR effect on (a) time-averaged surface level profile and (b) surface level fluctuations

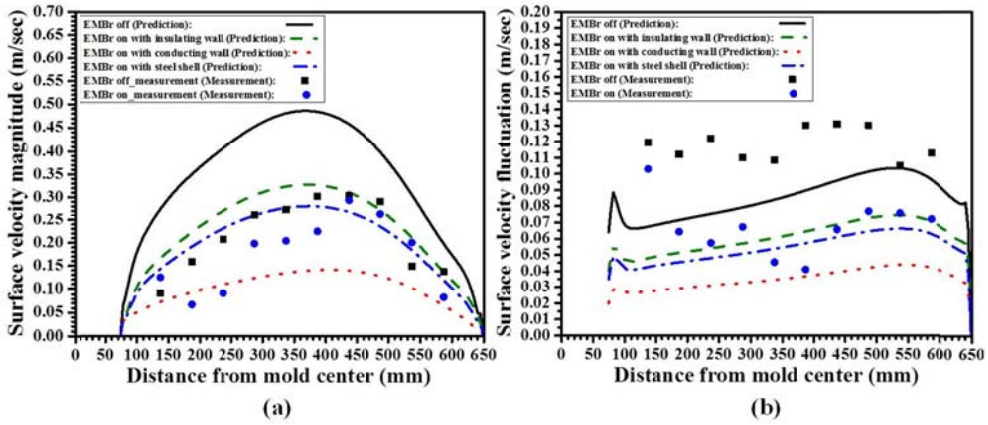

Fig.4.11. EMBR effect on (a) time-averaged surface velocity and (b) surface velocity fluctuations

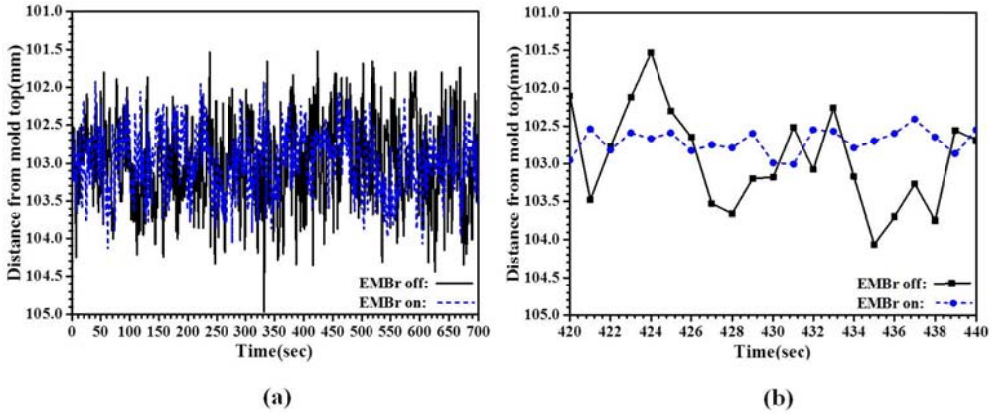

Fig.4.12. Surface level variations measured by the eddy current sensor during (a) 700 sec and (b) 20 sec with expanded scale

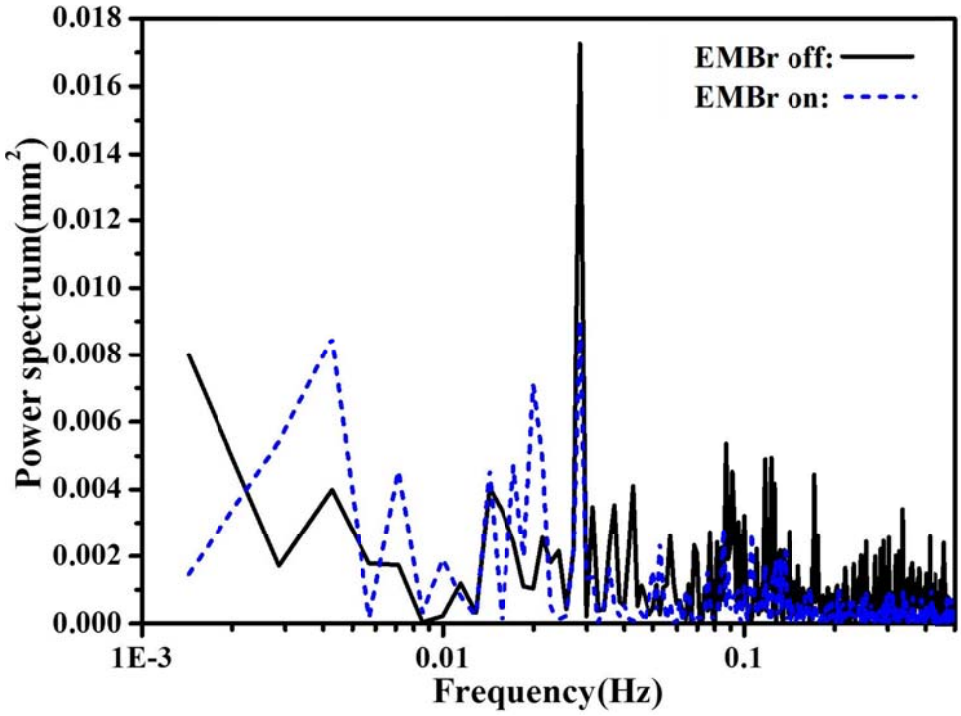

Fig.4.13. Power spectrum of the surface level signal measured by the eddy current sensor

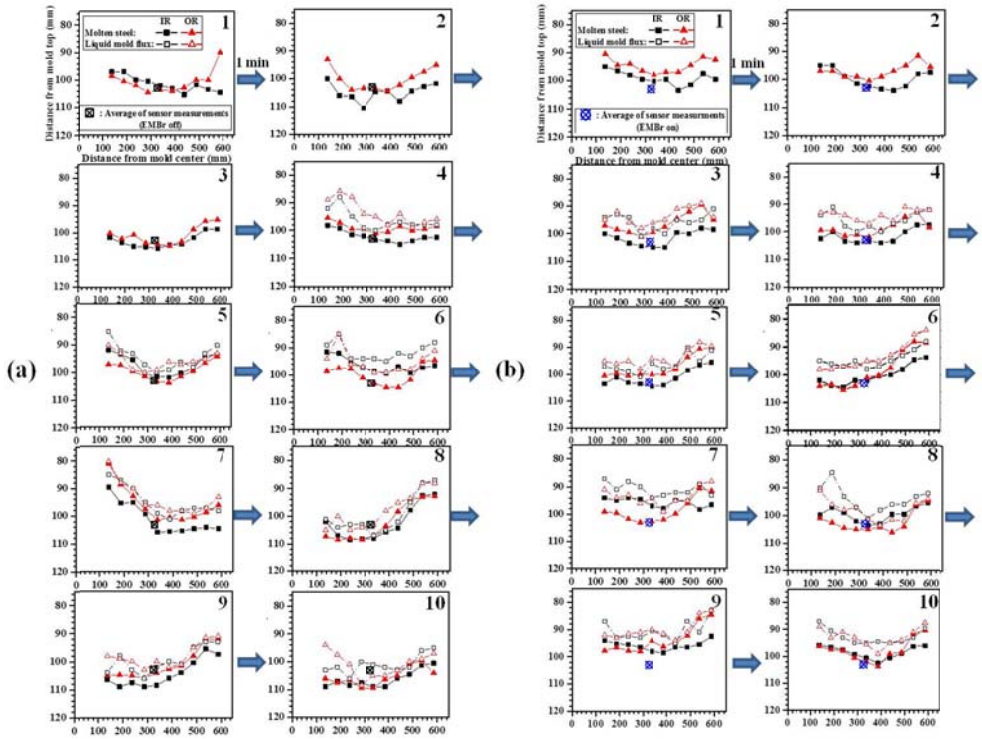

Fig.4.14. Transient variations of surface level profile (a) without and (b) with EMBr by the nail board measurements

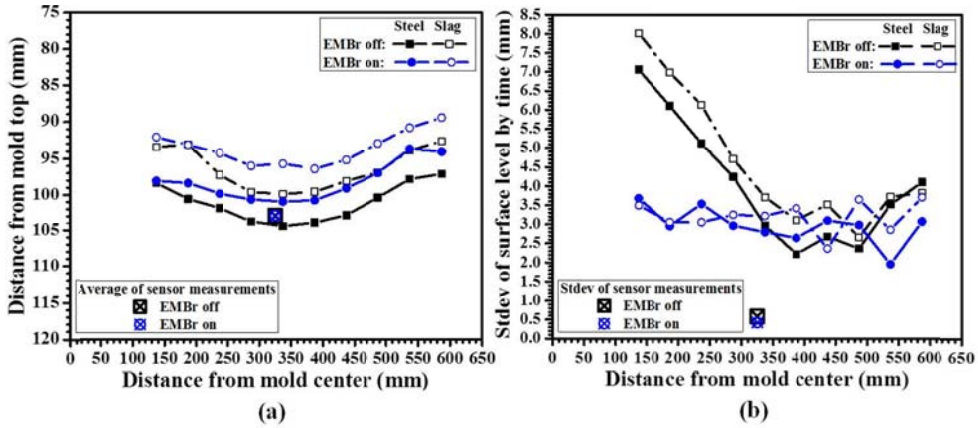

Fig.4.15. EMBR effect on (a) time-averaged surface level and (b) surface level fluctuation by the nail board measurements

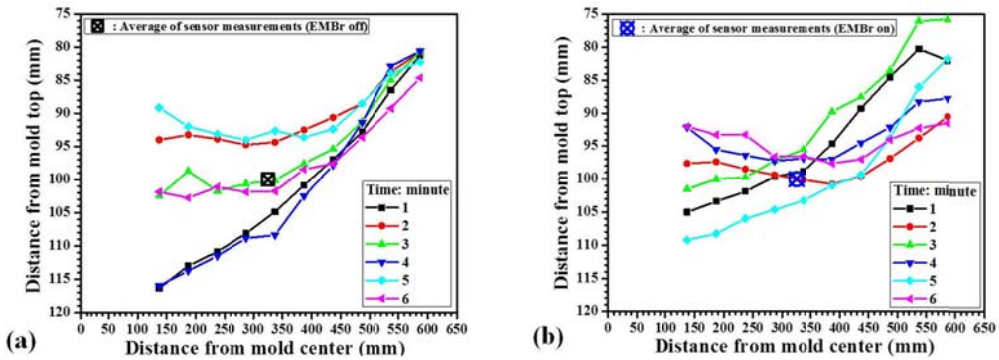

Fig.4.16. Measured molten steel surface level shape (a) without EMBr and (b) with EMBr

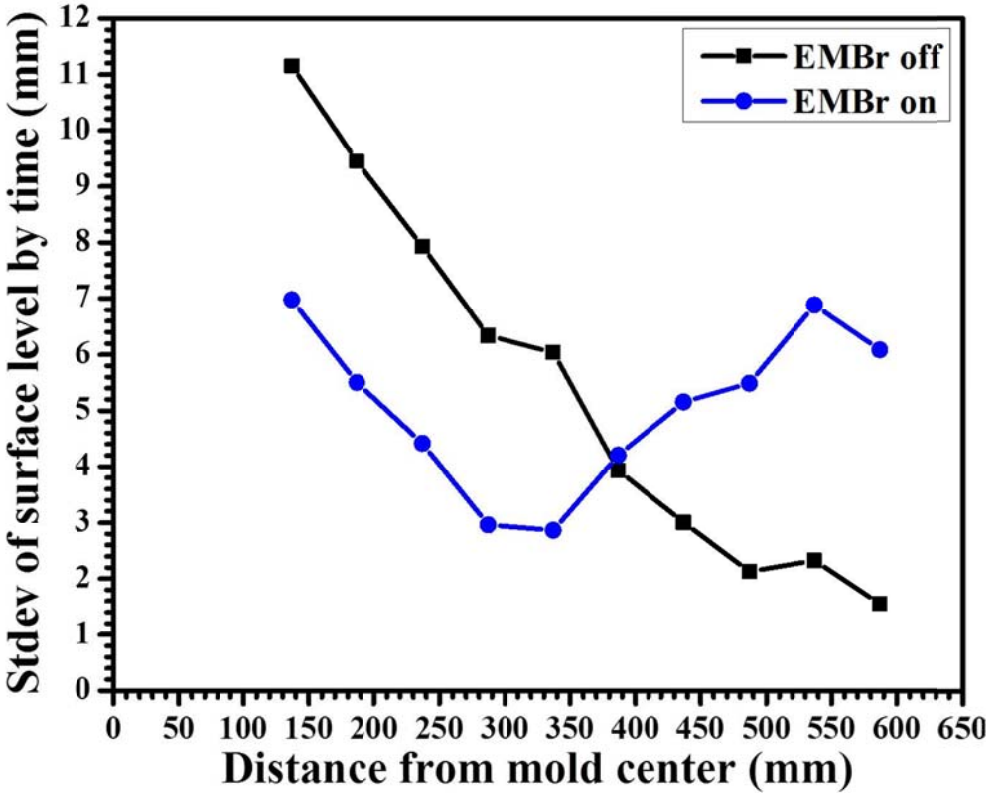

Fig.4.17. Measured molten steel surface level fluctuations without and with EMBr

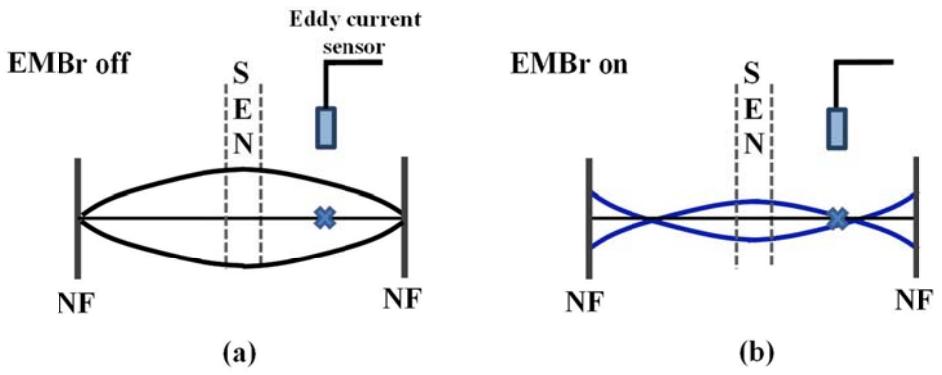

Fig.4.18. Schematic of the sloshing level mechanism (a) without and (b) with EMBr

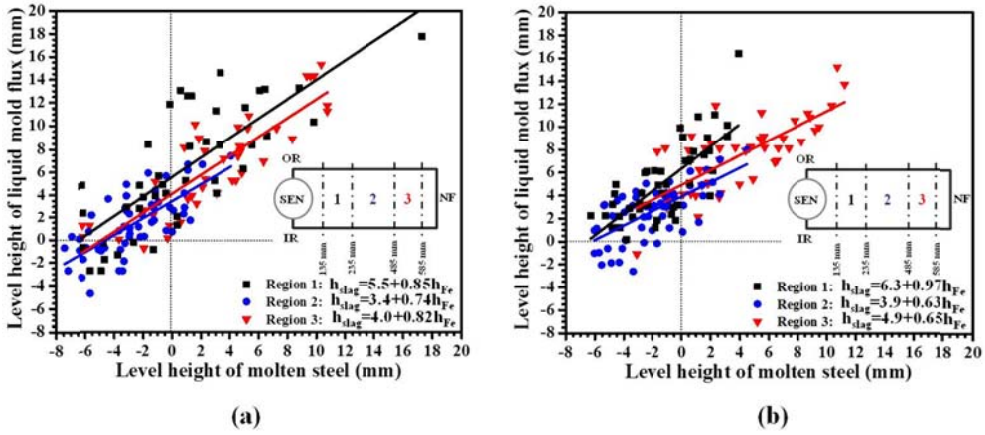

Fig.4.19. Relation between molten steel level and liquid mold flux level (a) without EMBr and (b) with EMBr by the nail board measurements

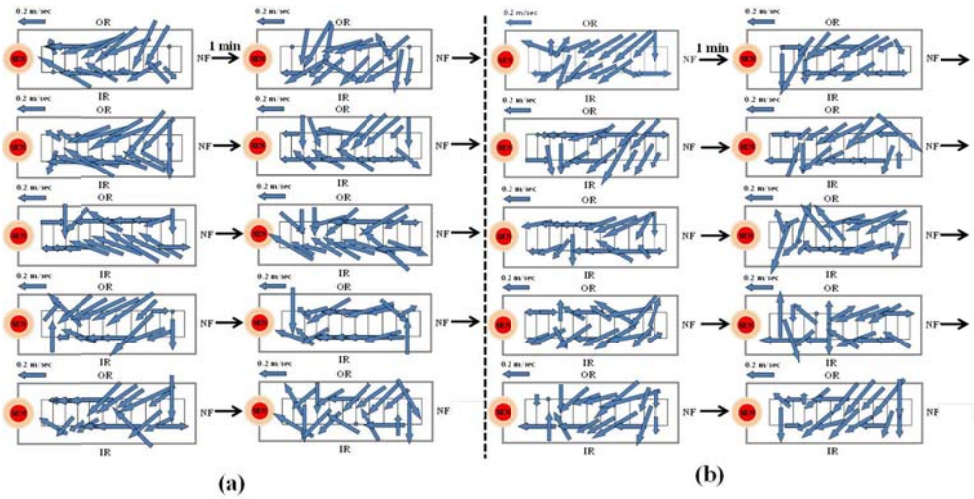

Fig.4.20. Transient variations of surface flow pattern (a) without and (b) with EMBr by the nail board measurements

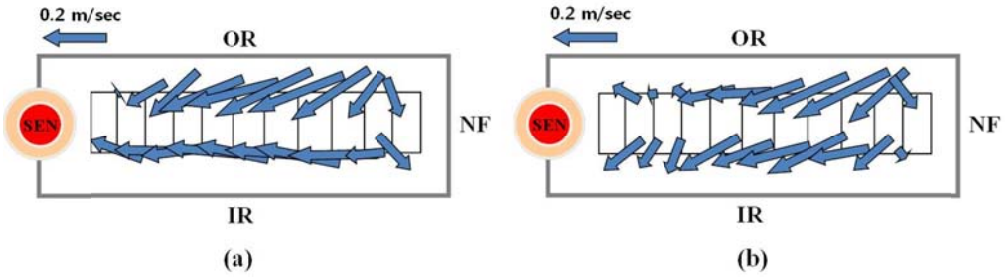

Fig.4.21. Averaged surface flow pattern (a) without and (b) with EMBR by the nail board measurements

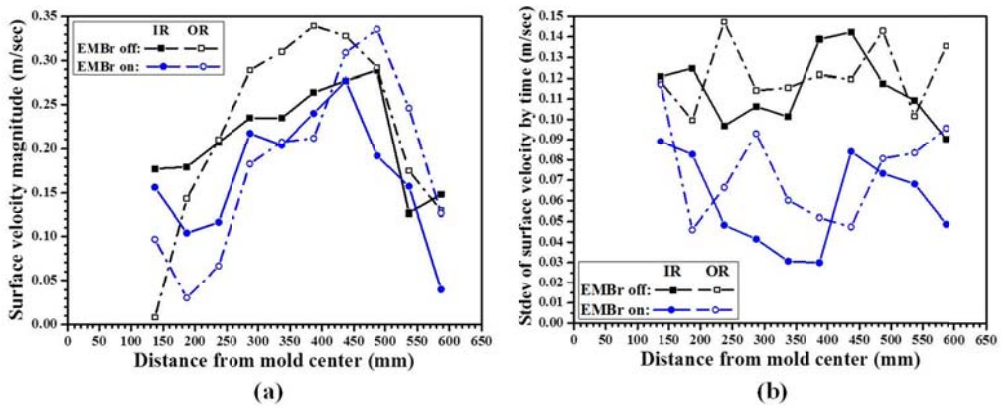

Fig.4.22. EMBR effect on (a) time-averaged surface velocity and (b) surface velocity fluctuation by the nail board measurement

4.9. References

1) K. Takatani, K. Nakai, T. Watanabe, and H. Nakajima: ISIJ Int, Vol. 29 (1989), 1063
2) K. Moon, H. Shin, B. Kim, J. Chung, Y. Hwang, and J. Yoon: ISIJ Int, Vol. 36 (1996), S201
3) Y. Hwang, P. Cha, H. Nam, K. Moon, and J. Yoon: ISIJ Int, Vol. 37 (1997), 659
4) H. Harada, T. Toh, T. Ishii, K. Kaneko, and E. Takeuchi: ISIJ Int, Vol. 41 (2001), 1236
5) B. Li and F. Tsukihashi: ISIJ Int, Vol. 43 (2003), 923
6) Z. Qian and Y. Wu: ISIJ Int, Vol. 44 (2004), 100
7) H. Yu and M. Zhu: ISIJ Int., Vol. 48 (2008), 584
8) K. Cukierski and B. G. Thomas: Metallurgical and Materials Transaction B, Vol. 39B (2008), 94
9) Y. Wang and L. Zhang: Metallurgical and Materials Transaction B, Vol. 42B (2011), 1319
10) B. Li, T. Okane, and T. Umeda: Metallurgical and Materials Transaction B, Vol. 31B (2000), 1491
11) B. Li, T. Okane, and T. Umeda: Metallurgical and Materials Transaction B, Vol. 32B (2001), 1053
12) K. Timmel, S. Eckert, G. Gerbeth, F. Stefani, and T. Wondrak: ISIJ Int., Vol. 50 (2010), 1134

13) K. Timmel, S. Eckert, and G. Gerbeth: Metallurgical and Materials Transaction B, Vol. 42B (2010), 68

14) R. Chaudhary, B. G. Thomas, and S.P. Vanka: Metallurgical and Materials Transaction B, Vol. 43B (2012), 532

15) R. Singh, B.G. Thomas, and S.P. Vanka: Metallurgical and Materials Transaction B, in press (2013)

16) S. Cho, H. Lee, S. Kim, R. Chaudhary, B.G. Thomas, D. Lee, Y. Kim, W. Choi, S. Kim, and H. Kim: Proc. of TMS2011, TMS, Warrendale, PA, USA, 2011, 59

17) R. Singh, B. G. Thomas and S. P. Vanka: CCC Report 201302, University of Illinois, Aug. 14, 2013.

18) S-M. Cho, S-H. Kim, and B.G. Thomas: ISIJ Int., submitted, 2013.

19) X. Huang and B. Thomas: Canadian Metallurgical Quarterly, Vol. 37 (1998), 197

20) T. A. Honeyands and J.Herbertson: 127th ISIJ Meeting, Tokyo, Japan (1994)

21) B.G. Thomas, F. M. Najjar, and L. J. Mika, Proc. of the Weinberg Symposium on Solidification Processing, C.I.M. Conference, Hamilton, Ontario, 1990, 131

22) X. Huang, B.G. Thomas, and F.M. Najjar: Metallurgical and Materials Transaction B, Vol. 23B (1992), 339

23) B. Zhao, S. P. Vanka, and B. G. Thomas.: Int. J. Heat and Fluid Flow, Vol. 26 (2005), 105

Chapter 5: Modeling of Two-Phase Fluid Flow in the Nozzle and Mold of Continuous Steel Slab Casting with Electro-Magnetic Braking (EMBr)

5.1. Introduction

Argon gas injection to prevent nozzle clogging and Electro-Magnetic Braking (EMBr) both greatly influence the transient surface flow in the nozzle and mold, affecting time variation of the fluid flow phenomena, as discussed in Chapters 3 and 4. Two-phase (molten steel-argon) flow shows jet wobbling in the mold, which results in fluctuations in the surface velocity and level. Double-ruler EMBr induces a more stable surface flow by reducing the turbulent kinetic energy and deflecting the jet flow downward in the mold.

Many researchers have investigated the effects of EMBr on single-phase (molten steel) flow in the nozzle and mold[1-8]. Some previous studies considered the effects of EMBr on time-averaged molten steel-argon flow in the mold[9-15]. However, few researchers have addressed the effect of EMBr on transient two-phase flow using plant measurements [16].

Chapter 5 investigates the effect of double-ruler EMBr on transient molten steel-argon flow in the nozzle and mold by applying computational modeling, validated by plant measurements performed at the surface of the mold. A transient two-phase flow field without the double-ruler EMBr is first calculated by Large Eddy

Simulation (LES) coupled with Discrete Phase Model (DPM), as described in Chapter 3. After the prediction of the transient two-phase flow field, the Magneto-Hydro-Dynamics (MHD) model given in Chapter 4 is implemented with the LES-DPM model. The model predictions with and without EMBr are validated by comparing the surface velocity magnitude, the surface level, and the fluctuations with the measurements, using the nail boards discussed in Chapter 4. The validated models are then used to analyze the time-averaged and –dependent results in the nozzle and mold to obtain a deeper insight into the effect of EMBr on the transient two-phase flow.

5.2. Plant Measurements

The external magnetic field induced by the double-ruler EMBr in the mold cavity was measured by a Gauss meter. The nail board dipping test was performed to quantify time-averaged and time-dependent surface flow, including velocity and level phenomena. The details of the measurements were explained in Chapter 4.

The surface velocity magnitude, the surface level, and the fluctuations measured at each location across the mold width were spatially averaged over the Inside Radius (IR) and the Outside Radius (OR) for comparison with the predictions on the centerline of the surface, which is the interface between the molten steel and the liquid flux layer.

5.3. Computational Model

A three-dimensional finite-volume computational model employing the LES, coupled with the DPM and MHD equations, is applied to predict the molten steel flow field influenced by the argon gas motion and the magnetic field in the nozzle and mold. Two cases are considered: two-phase (molten steel-argon gas) flow without EMBr and two-phase flow with EMBr. The steady-state single-phase (molten steel) flow was first predicted by the standard $k-\varepsilon$ model and the LES coupled with the DPM was then applied to calculate the two-phase flow, considering the interaction between the molten steel and the argon bubble motions. The effect of the static magnetic field of the double-ruler EMBr on the two-phase flow was considered by implementing the MHD equations into the LES coupled with DPM. The equations and boundary conditions were solved with the finite-volume method in ANSYS FLUENT.

5.3.1. Governing Equations

Mass conservation of molten steel is as follows:

$$\frac{\partial}{\partial x_i}(\rho u_i) = S_{shell,\ mass} \quad [5.1]$$

where ρ is the molten steel density, u_i is the velocity, and $S_{shell,mass}$ is a mass sink term for solidification, which was given in Eqn. 3.3.

The time-dependent momentum balance equation that considers the effects of argon gas and electromagnetic force induced by EMBr is given by:

$$\frac{\partial}{\partial t}(\rho u_i) + \frac{\partial}{\partial x_j}(\rho u_i u_j) = -\frac{\partial p^*}{\partial x_i} + \frac{\partial}{\partial x_j}\left[(\mu + \mu_t)\left(\frac{\partial u_i}{\partial x_j} + \frac{\partial u_j}{\partial x_i}\right)\right] + S_{shell,mom,i} + S_{Ar,mom,i} + F_{L,i}$$

[5.2]

$S_{shell,mom,i}$, given in Eqn. 3.6, is a momentum sink term in each component direction for consideration of the solidification of the molten steel on the wide faces and the narrow faces. This term is also applied to the cells that consider $S_{shell,mass}$. The mass and momentum sink terms, $S_{shell,mass}$, $S_{shell,mom,i}$, are implemented into ANSYS FLUENT with User-Defined Functions (UDF). $S_{Ar,mom,i}$ is a momentum source term that considers the effect of argon gas bubble motion on molten steel flow. The value of $S_{Ar,mom,i}$, is calculated using the Lagrangian DPM model, which solves a force balance among the drag, buoyancy, virtual mass, and pressure gradient forces on each argon bubble. The equations of the DPM model are given in Eqns. 3.13-3.17. In the DPM

model, a mean bubble size of 0.84 mm (calculated for the molten steel pool in the UTN by coupling the bubble formation model and the active site model, as given in Chapter 2) was chosen as an input data. The details of argon gas injection conditions are given in Table 2.1 of Chapter 2. A Lorentz force source term $F_{L,i}$ is added to the LES model to consider the magnetic field effect on the two-phase flow field. The source term is calculated by considering the interaction between the induced current density and the total magnetic field. The total magnetic field includes measured the external magnetic field and the induced magnetic field, which is calculated by the magnetic induction Eqn 4.3 given in Chapter 4.

5.3.2. Domain, Mesh, Boundary Conditions, and Numerical Methods

The details of the domain, mesh, boundary conditions, and numerical methods for the LES, DPM, and MHD models are given in Chapters 3 and 4.

5.3.3. Computation Details

The steady-state single-phase flow field calculated by the standard $k-\varepsilon$ model was used to initialize the LES model. The transient two-phase LES model was started at time = 0 sec and run for 57.2 sec. The two-phase flow without EMBr was

allowed to develop for 15 sec, and then a further 15.33 sec of data were used for compiling time-average results. After 30.33 sec, for the case of the two-phase flow without EMBr, the magnetic field was imposed on the two-phase flow field by implementing the MHD equations to the LES coupled with DPM. The two-phase flow with EMBr was allowed to develop for 10 sec beyond 30.33 sec, and then a further 16.86 sec of data were used for compiling time-averaged flow affected by EMBr.

5.4. Model Validation

The time-averaged surface velocity magnitude profiles predicted by the LES model are compared in Fig. 5.1 with the nail board measurements. The model predictions are further validated by comparing the surface velocity magnitude fluctuation profiles, given by Root Mean Square (RMS) velocity magnitude $\sqrt{\overline{(u')^2}+\overline{(v')^2}+\overline{(w')^2}}$, in Fig. 5.2 with the measured fluctuations given by the standard deviation of the measured instantaneous surface velocity magnitudes at each location across the mold width. For both the EMBr off and on cases, the LES model shows the remarkable agreements with the measurements. The qualitative and quantitative agreements for the surface velocity magnitude and its fluctuation confirm that the LES model is applicable as a turbulence model that is sufficient to predict reasonable time-averaged and –dependent flow in the nozzle and mold of a continuous steel slab caster.

The model prediction of the molten steel-argon flow shows that double-ruler EMBr reduces the velocity magnitude by ~20% and velocity fluctuation by ~40 % at the surface in the mold. The dominant decrease of the surface velocity magnitude is shown at the region covering 200 ~ 400mm away from the mold center. The EMBr enhances the surface stability by decreasing the surface velocity fluctuations across the mold width. The effects of the EMBr on the surface flow will be discussed in greater detail in Sections 5.5.2, 5.6.1, and 5.6.2.

5.5. Time-Averaged Results

The validated LES model allows evaluation of the predicted velocity, turbulent kinetic energy, and RMS velocity fluctuation for quantification of the effect of double-ruler EMBr on the time-averaged molten steel-argon flow in the nozzle and mold during continuous casting.

5.5.1. Nozzle Flow

The time-averaged velocity vectors with the magnitude contours in the nozzle bottom are shown in Fig. 5.3. The front views show that the predicted nozzle flow with and without EMBr are very similar. The side views show an asymmetric

swirl flow pattern in the nozzle bottom, which is induced by the asymmetric open area in the middle plate of the slide-gate that delivers the molten steel from the UTN to the SEN; this swirl shows a clockwise direction without EMBr and a counter-clockwise direction with EMBr.

Figs. 5.4 and 5.5, respectively, show the turbulence kinetic energy and RMS velocity fluctuations of the nozzle flow. The EMBr slightly decreases the turbulent kinetic energy and moves the high energy region from the Inside Radius (IR) to the Outside Radius (OR) in the nozzle bottom. The RMS velocity fluctuations in each axis direction (x: casting direction, y: mold width direction, z: mold thickness direction) are shown in both front and side views of the nozzle bottom. In both the EMBr off and on cases, the velocity fluctuation increases according to the following sequence: y axis < z axis < x axis. The effect of EMBr on the velocity instability is dominant along the x axis, the casting direction. The EMBr moves the location of high velocity fluctuation in the nozzle bottom from the IR to the OR region, which is similar with the trend seen for the turbulent kinetic energy change. This is related to the directional change of the swirl flow induced by EMBr, as shown in Fig. 5.3.

The EMBr effect on the mean nozzle flow seems to be small, even though the Lorentz force in the nozzle is strong. This means that the maximum magnetic field (~ 0.17 Tesla) of the EMBr is not sufficient to influence the high momentum flow in the nozzle.

5.5.2. Mold Flow

The time-averaged mold flow with and without EMBr was investigated next; the results are shown in Figs. 5.6–5.11. The velocity, flow pattern, turbulent kinetic energy, and RMS velocity fluctuations are analyzed for each case (two-phase flow without EMBr and two-phase flow with EMBr).

The two-phase flow from the nozzle to the mold region is significantly affected by the double-ruler EMBr. The jet flow in the mold without EMBr shows an uprising flow pattern in the upper recirculation region, as shown in Fig. 5.6. This is likely caused by the buoyancy effect of the argon gas on the flow. The lower recirculation region shows a much more chaotic and complex flow pattern for the ~15 sec time averaging. The low frequency fluctuation (long-term variation) might be dominant in the lower region. The jet flow with EMBr is deflected downward by the electromagnetic force. This induces a slower velocity at the surface and slightly enhances the downward flow along the NF, which could be detrimental to floatation of argon bubbles toward to the surface. In the upper region, the EMBr produces a small rotating flow zone near the SEN by braking the surface flow from the NF and increasing the other surface flow—which is induced by the argon gas floating near the SEN—towards to the NF. In the lower roll region, EMBr causes multi-rolls by imposing the electromagnetic force on the mold.

Fig. 5.7 shows the turbulent kinetic energy contours of the mold flow. As expected from the mold flow pattern without EMBr, the steel-argon flow shows high turbulent kinetic energy in the upper-roll region and lower energy in the lower-roll region. An argon gas floating effect on the mold flow seems to be the cause of this phenomenon. With the double-ruler EMBr, turbulent kinetic energy is decreased in both the upper and lower roll regions.

The velocity fluctuations in each axis direction (x: casting direction, y: mold width direction, z: mold thickness direction) in the mold center plane are shown in Fig. 5.8. Both cases show high velocity fluctuations in all directions. Compared with the fluctuations in the nozzle flow, which shows severe instability along casting direction, mold flow shows a different fluctuation trend, as all axes show similar instability in the mold. This is probably caused by dispersion of the rotating swirl when the nozzle flow enters the mold. As expected from the contours of turbulent kinetic energy, the velocity fluctuations with EMBr become smaller in the upper-roll region in all directions. However, even though the electromagnetic force near the nozzle port is the highest in the mold, as shown in Fig. 4.5 of Chapter 4, the force is not sufficient to decrease strongly the velocity fluctuation of the high momentum jet flow. Furthermore, EMBr reduces the velocity fluctuation in the center region of the lower-roll zone.

The velocity magnitude and turbulent kinetic energy at the surface of the mold are reduced in response to EMBr, as shown in Figs. 5.9 and 5.10. Without EMBr, high velocity magnitude and turbulent kinetic energy are induced by the uprising flow pattern in the mold. In addition, the surface flow without EMBr is asymmetric,

showing a biased cross flow from the OR to the IR, which is produced by the rotating asymmetric swirl flow shown in Fig. 5.3. In contrast, EMBr decreases the surface velocity and reduces this asymmetric flow phenomenon by suppressing the upper roll pattern. With EMBr, the turbulent kinetic energy is also decreased at the surface.

The effect of EMBr on surface velocity fluctuations was investigated by comparing the velocity fluctuation profiles in all axes, as shown in Fig.5.11. With EMBr, the velocity fluctuations along all axes are decreased across the mold width. However, the fluctuations with and without EMBr show similar values in the region near the SEN, where two surface flows (one from the NF to the SEN and the other from the SEN to NF, as shown in Fig. 5.9) collide with each other or produce vortices. The slag pool is more likely to be entrained by increasing the instability at the interface between the molten steel and liquid mold flux layers, near the SEN with and without EMBr. Furthermore, Liu et al. introduced the problem of the "exposed eye" of the molten steel near the SEN, which results in serious reoxidation of the molten steel and induces defects in the steel slab[17)].

5.6. Transient Results

The LES coupled with DPM provides insight into the transient flow phenomena, which are more related to defect formation during the continuous casting than is the time-averaged flow field. Snapshots of the velocity magnitude, velocity

vector, and argon gas distribution in the mold are presented to quantify the EMBr effect on the transient flow phenomena. In addition, time variations in velocity in the mold are analyzed.

5.6.1. Transient Mold Flow Pattern

Time-averaged and instantaneous velocity magnitude contours at the center-middle plane in the mold are shown in Fig. 5.12. The instantaneous snapshots are spaced by 1.2 sec for both the EMBr off and on cases. The time for each snapshot of the EMBr off case refers to the period after argon gas injection, while the time for the EMBr on case is the period after EMBr application. The mold flow shows a classic double roll pattern with and without EMBr. The mold flow patterns show upward and downward wobbling in the mold with time, which induces different impinging points of the jet flow on the NF. This produces fluctuations in the upper-roll and lower-roll flow in the mold, resulting in velocity fluctuations. EMBr suppresses these fluctuations and deflects the jet flow downward, deeper into the mold cavity. This downward jet flow results in less wobbling in upper-recirculation zone and induces a slower surface flow with higher stability. The instantaneous velocity vector in the mold, shown in Fig. 5.13, confirms this EMBr effect on the transient mold flow pattern.

Fig. 5.14 shows the transient surface flow patterns separated by 1.2 sec. The strong cross flow between the IR and the OR is suppressed by application of EMBr to the mold. The surface velocity and velocity fluctuations also decrease in response to EMBr.

5.6.2. Time Variation of Velocity in the Mold

Instantaneous velocity histories are presented at seven locations (as shown in Fig. 5.15) in the mold. As shown in Figs. 5.16 and 5.17, point P-1 in the mold inlet has a higher velocity magnitude and fluctuation in all directions (x, y, z direction), compared with P-2. The rotating swirl flow in the well-bottom region shown in Figs. 5.3-5.5 causes severe flow instability, inducing high velocity fluctuations at P-1. Point P-3 in the deeper mold region shows a smaller velocity and fluctuations than seen at P-2. After the jet flow impinges on the NF, the turbulence is suppressed, inducing a lower frequency variation with smaller fluctuations in the low recirculation region along the NF, as shown in Fig. 5.18. At both points P-1 and P-2, the velocity fluctuation along the mold width direction is more severe than in the other directions. On the other hand, point P-3 shows a high velocity fluctuation along the casting direction. These different trends in the fluctuation behavior are caused by different main directions of the flow stream (the jet flow in the mold is towards to the NF, while downward flow along the NF wall is the casting direction). With EMBr, the velocity

fluctuations along all directions are decreased at points P-1 and P-3. However, point P-2 does not show any fluctuation suppression by EMBr because the downward-deflected jet flow slightly increases the instability along mold width and thickness direction at this point.

Fig. 5.19 shows time variation of the velocity magnitude during ~15 sec (0 sec on the x axis of each graph, means the start time for compiling the results after developing the flow) at each point P-3, P-4, P-5, and P-6 at the surface, with and without EMBr. Without EMBr, point P-5 (w/4 region), midway between the SEN and the NF, shows the highest average velocity (~0.31 m/sec) at the surface, with fluctuations of ~0.055 m/sec. On the other hand, point P-4 shows the highest velocity (~0.18 m/sec), with highest its fluctuation (~0.042 m/sec) with EMBr. At all points, EMBr decreases the surface velocity magnitude and its fluctuation by inducing low frequency / long term variation. This might be caused by suppression of small-scale turbulence in the upper-roll zone by EMBr, as shown in Fig. 5.12. The double-ruler EMBr studied in this work is influential in suppressing the turbulence of high frequency in the mold.

5.6.3. Transient Surface Level

The predicted surface level height profile is calculated by Eqn. 5.3 as follows.

$$H_i = \frac{P_i - P_{avg}}{\left(\rho_{steel} - (1-k)\rho_{slag}\right)g} \quad [5.3]$$

where H_i is the surface level height at the location i, P_i is the static pressure at the location i, P_{avg} is the spatial-averaged pressure across mold width, ρ_{steel} is the molten steel density, ρ_{slag} is the slag density, and k is the coefficient of slag motion according to molten steel motion, given in Table 2.1. The coefficient k is obtained from the nail board dipping test results discussed in Chapter 4. The coefficients are given for three regions: SEN region 1 from 135 mm to 235 mm, Quarter-point region 2 from 235 mm to 485 mm, and NF region 3 from 485 mm to 585 mm from the mold center.

As shown in Fig. 5.20, the predicted surface level profiles show reasonable agreement with the measured ones for both the EMBr off and on cases. The time variations of the level profiles predicted by the model are smaller than the measured values. This is likely because the measurements cover 9 minutes but the predictions only cover 15 sec. During the 15 sec, the LES model can capture only the high frequency and low amplitude components of the surface fluctuations. The low frequency and high amplitude wave motions observed in the measurements would require much longer modeling time. Furthermore, the half domain for the modeling is unable to capture surface level fluctuations caused by side-to-side sloshing between

NFs. Thus, consideration of the full domain covering two NFs and a longer flow time are needed.

5.6.4. Argon Bubble Distribution

Transient jet wobbling induces corresponding variations in the argon gas distribution, as shown in Figs. 5.21 and 5.22. Without EMBr, most argon bubbles behave according to the flow in the upper recirculation regions and float up to the surface. On the other hand, a respectable amount of argon bubbles are found in the lower recirculation region, covering 600~1200 mm from the mold top, with EMBr. This is caused by the enhanced downward flow deep into the mold cavity. The recirculation region just below the jet flow, as shown in Fig. 5.6, also gives the bubbles more residence time near the NF. This could increase the possibility that the argon bubbles could be entrapped by the solidifying steel shell near the NF wall, resulting in a greater production of defects in the steel slab. With EMBr, many argon bubbles also sometimes float up to the surface near the SEN wall. This phenomenon could increase the surface instability near the SEN and induce slag entrainments. Fig. 22 shows the transient argon bubble distribution at the surface. Without EMBr, most gas bubbles float up near the OR. With EMBr, most gas bubbles float up near the SEN and IR. This might be related to the rotating direction-changed swirl (from clockwise to counter clockwise) in the nozzle well bottom

5.7. Summary and Conclusions

The current work investigated the effect of double-ruler EMBr on transient molten steel-argon gas flow in the nozzle and mold of continuous steel slab casting by applying a LES model that couples DPM and MHD and validating this model with plant measurements using the nail boards.

- The double-ruler EMBr (studied in Chapters 4 and 5) creates two regions of equally-strong magnetic field (~ 0.17 Tesla) across the mold width: one centered just above the port (~ 250 mm from mold top) and the other centered farther below the nozzle port (~ 750 mm from mold top). Both peaks in the measured field significantly decrease in strength towards the NF.
- The LES coupled with DPM can capture transient two-phase (molten steel-argon gas) flows in all directions (x: casting direction, y: mold width direction, z: mold thickness direction) in the nozzle and mold with and without EMBr, showing great agreement of the surface velocity magnitude and its fluctuation with the nail board measurements.
- The double-ruler EMBr slightly decreases the velocity magnitude and turbulent kinetic energy of two-phase flow, resulting in a smaller velocity fluctuation $\sqrt{\overline{(\mathbf{u}')^2}}$ along the casting direction in the nozzle well region, where the rotating swirl flow is caused by the asymmetric open area at the

slide-gate. The direction of the swirl flow is changed from clockwise to counter-clockwise by the electromagnetic force.

- The EMBr deflects the jet flow downward, resulting in slower surface velocity with less fluctuation. In the upper recirculation region in the mold, the small-scale turbulence induced by transient jet wobbling is suppressed by the EMBr.
- Surface flow with EMBr shows smaller velocity magnitude and its fluctuations in all directions, decreasing the biased asymmetric flow between wide faces. The transient velocity profiles at the surface show lower frequency variation with higher stability .
- The lower-recirculation zone of two-phase flow without EMBr seems to have a low frequency / long period variation and does not show a developed flow pattern with ~15 sec averaging. With EMBr, this chaotic flow pattern is calmed.
- The slightly faster downward flow along the NF with EMBr could take argon bubbles and inclusions deep into the mold cavity, resulting in more internal defects. However, smaller variation with higher frequency of the flow velocity with EMBr could be desirable for uniform solidification of the molten steel near the NF.
- The double-ruler EMBr studied in this work is influential in the suppression of high frequency turbulence in the mold, but the magnetic field strength (maximum: ~ 0.17 Tesla) imposed by the EMBr is not sufficiently strong to

reduce the low frequency variations that have high power.

- The results of the predicted molten steel-argon flow field with and without EMBr indicate that non-metallic inclusion defects induced by surface flow instability could be reduced by imposing an EMBr, as this can suppress velocity fluctuations in all directions in the mold. However, argon gas floatation at the surface near the SEN may increase the interface between the molten steel and slag layers, resulting in slag entrainment.

- Argon gas bubbles influenced by EMBr have longer residence times in the region covering 600~1200 mm from the mold top. This could increase the possibility that the bubbles would be entrapped by the solidifying steel shell beside the NF, resulting in the production of more defects in the steel slab.

5.8. Tables and Figures

Table 5.1. Coefficient of slag motion at the surface regions without and with EMBr

	Region 1 (near SEN)	Region 2 (midway)	Region 3 (near NF)
Without EMBr	0.85	0.74	0.82
With EMBr	0.97	0.63	0.65

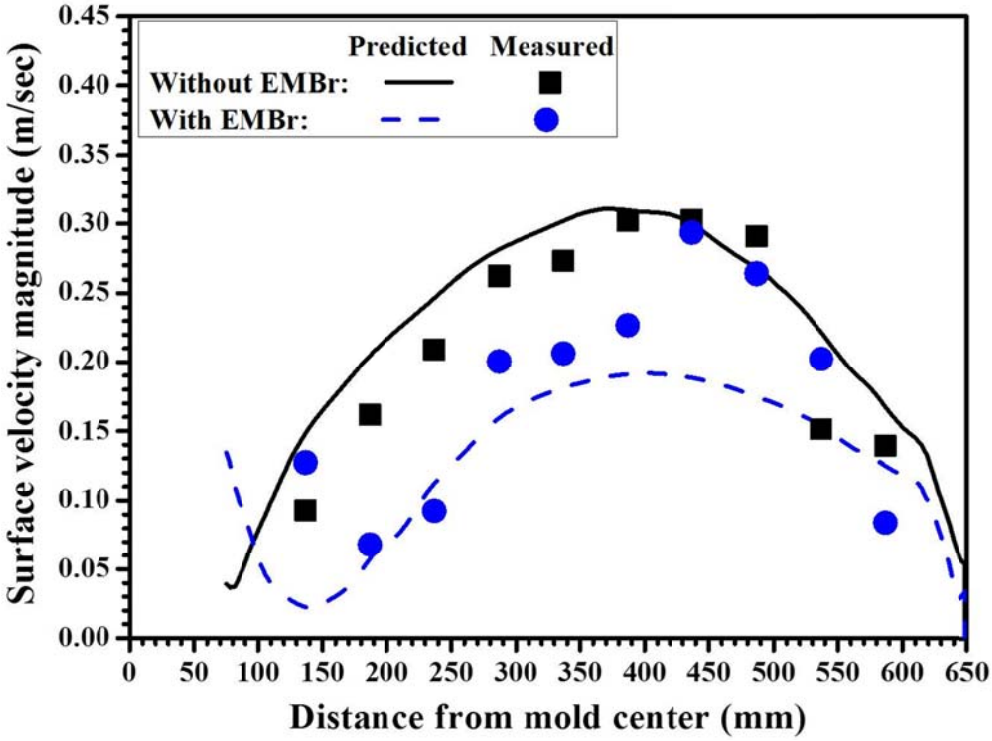

Fig.5.1. Comparison of time-averaged surface velocity magnitude between the model prediction and the plant measurement

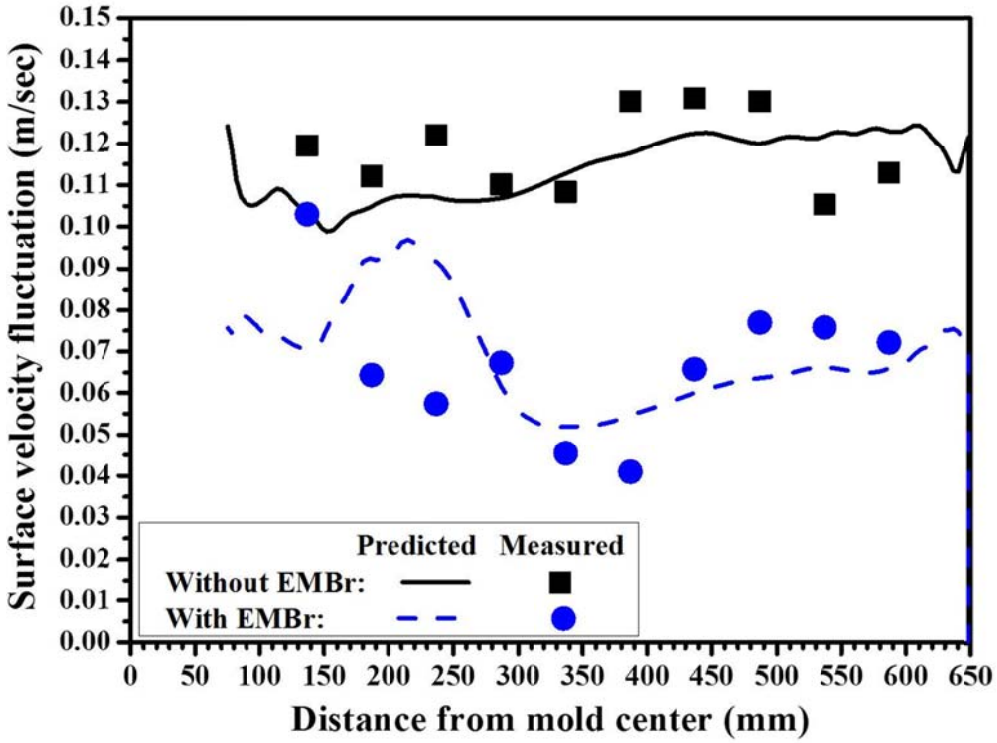

Fig.5.2. Comparison of surface velocity magnitude fluctuation between the model prediction and the plant measurement

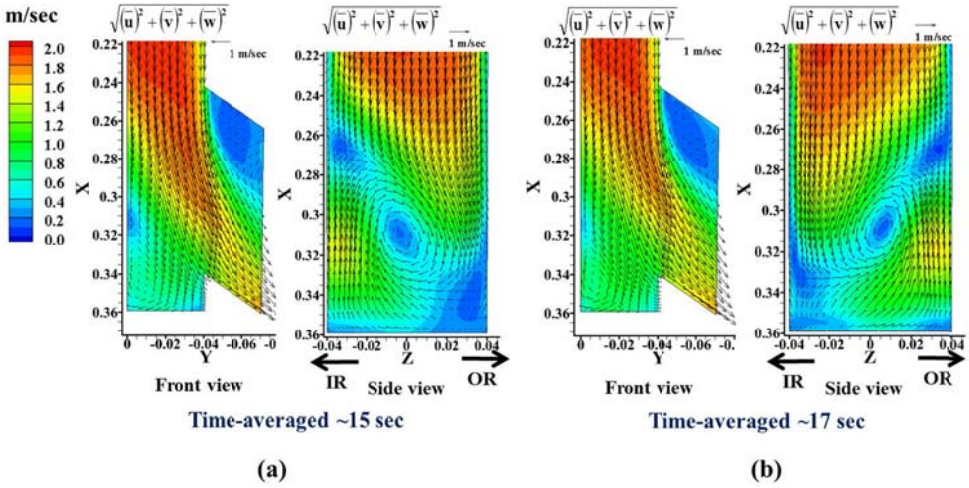

Fig.5.3. Time-averaged velocity vector and velocity magnitude contour in the nozzle bttom: (a) without EMBr and (b) with EMBr

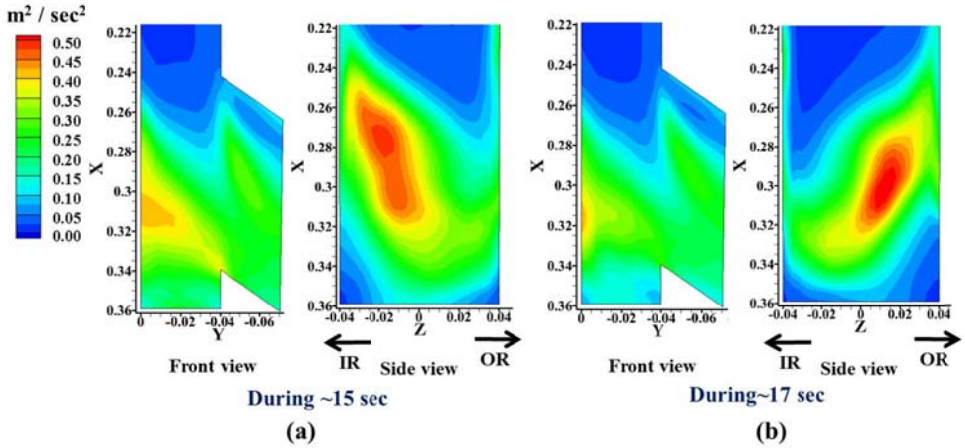

Fig.5.4. Turbulent kinetic energy in the nozzle bottom: (a) without EMBr and (b) with EMBr

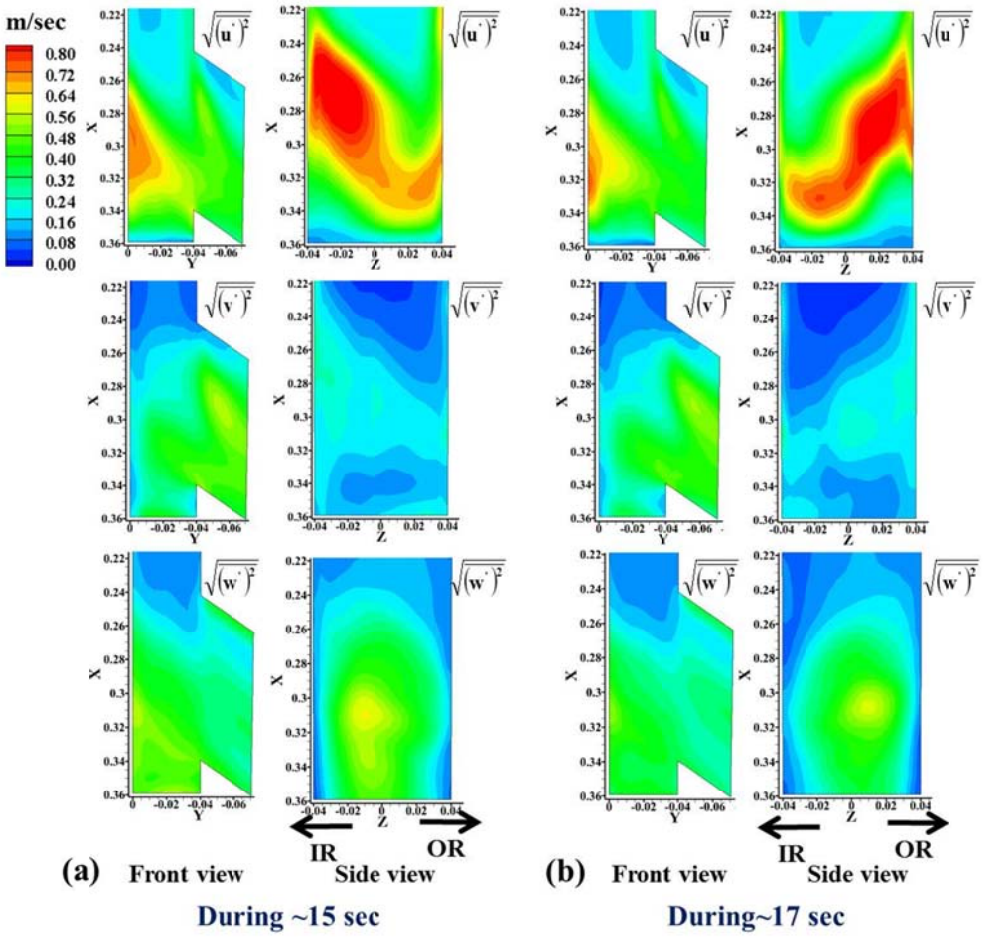

Fig.5.5. RMS velocity fluctuations in the nozzle bottom: (a) without EMBr and (b) with EMBr

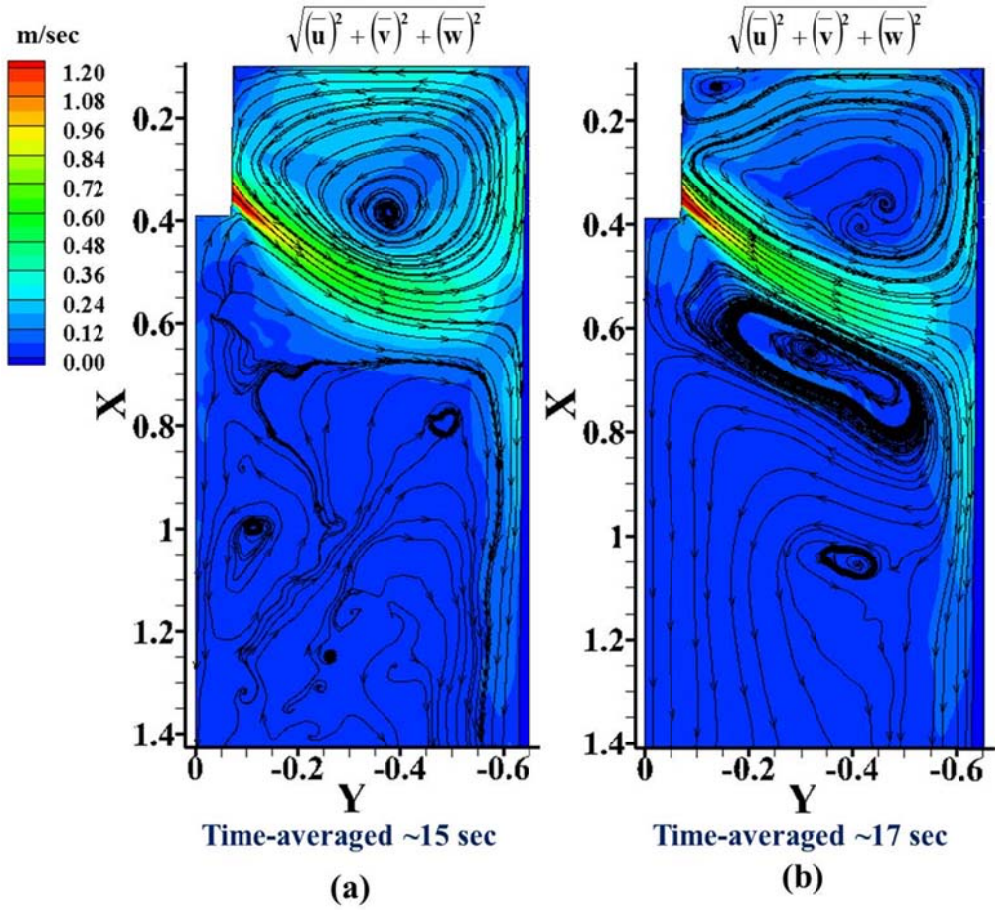

Fig.5.6. Time-averaged velocity contour and streamlines in the mold: (a) without EMBr and (d) with EMBr

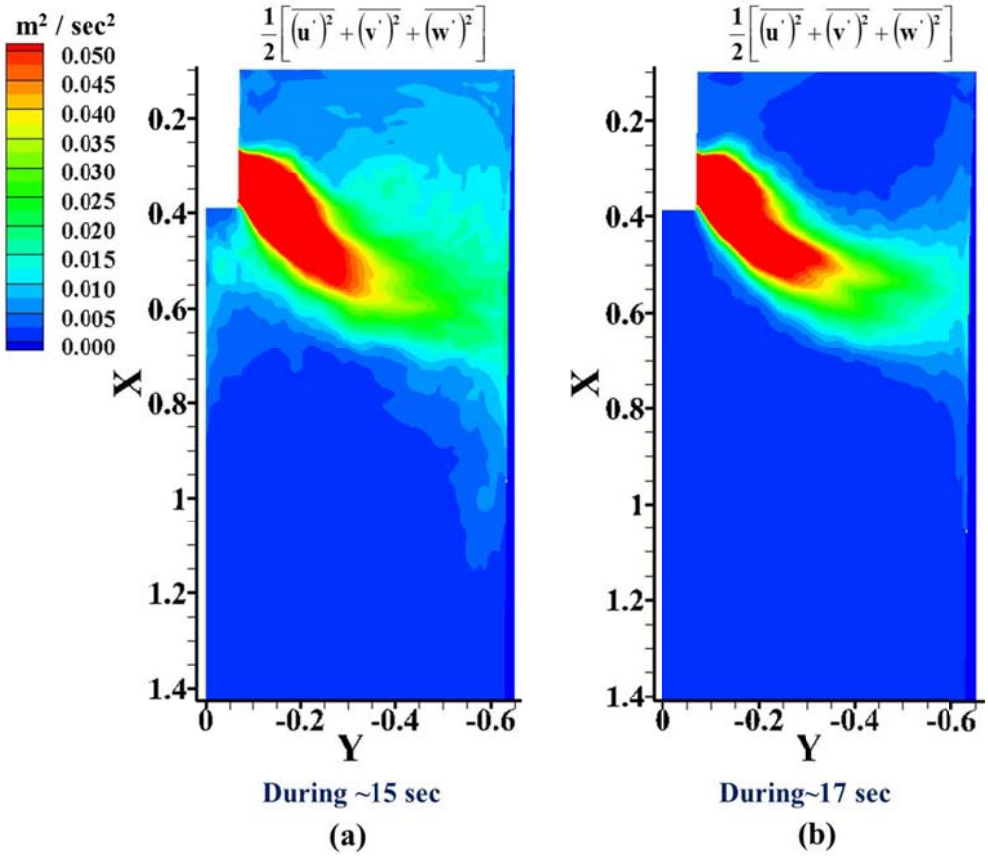

Fig.5.7. Turbulent kinetic energy contour in the mold: (a) without EMBr and (b) with EMBr

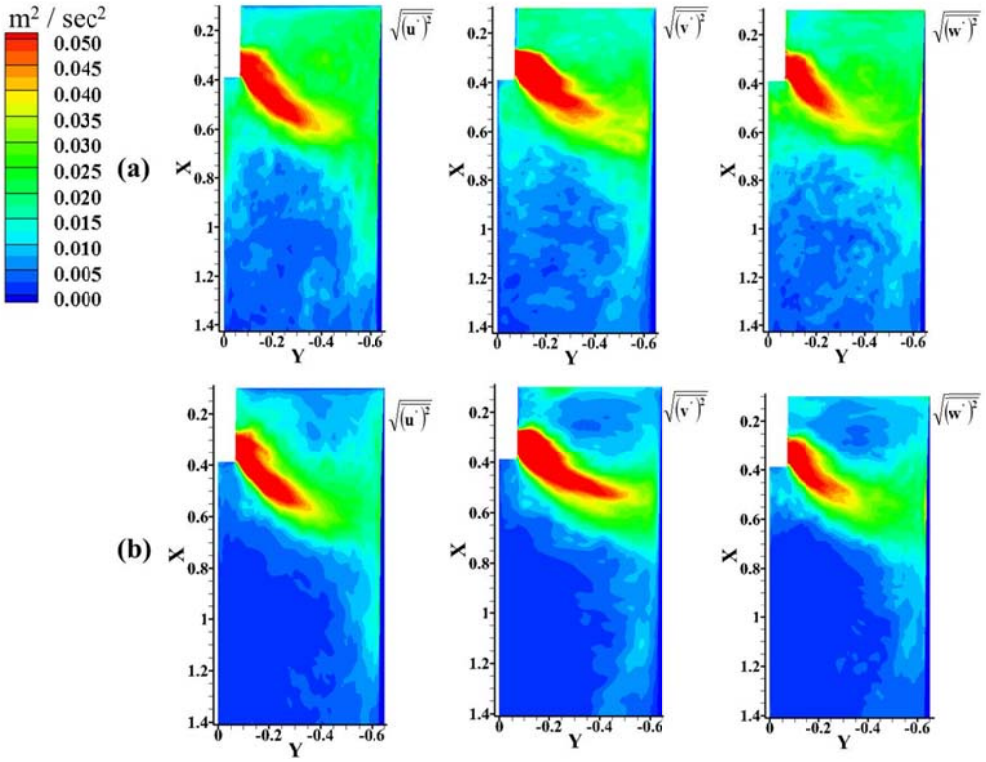

Fig.5.8. RMS velocities in the mold: (a)without EMBr and (b) with EMBr

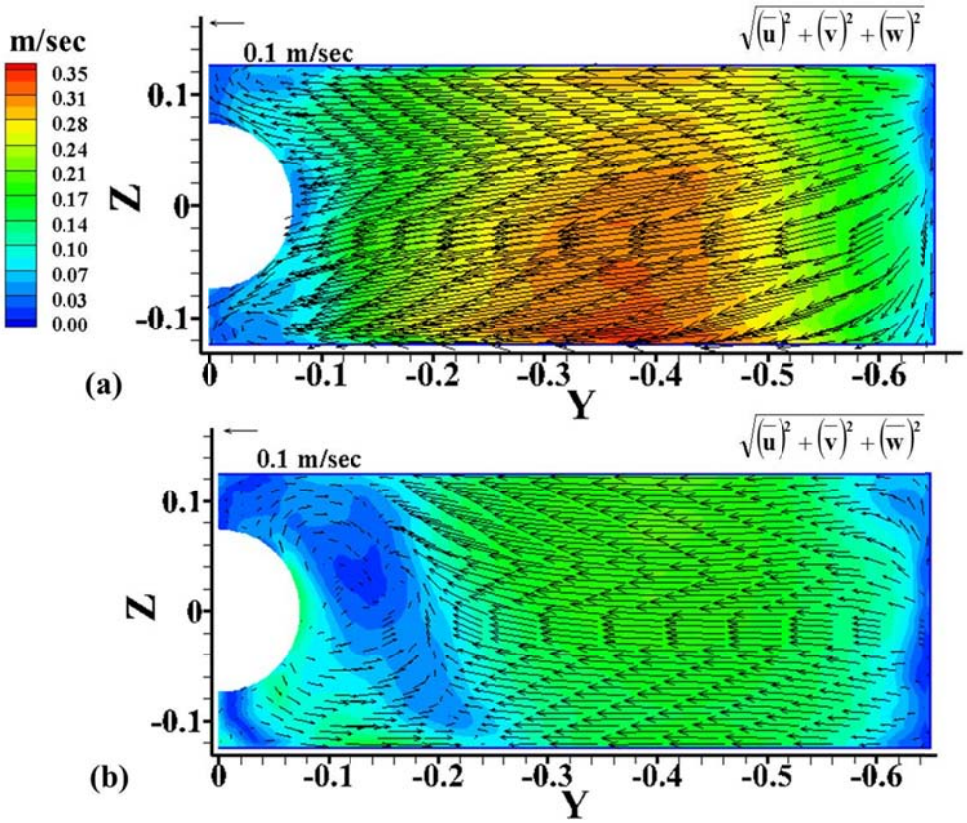

Fig.5.9. Time-averaged velocity magnitude contour and velocity vector at the surface in the mold (a) without EMBr and (b) with EMBr

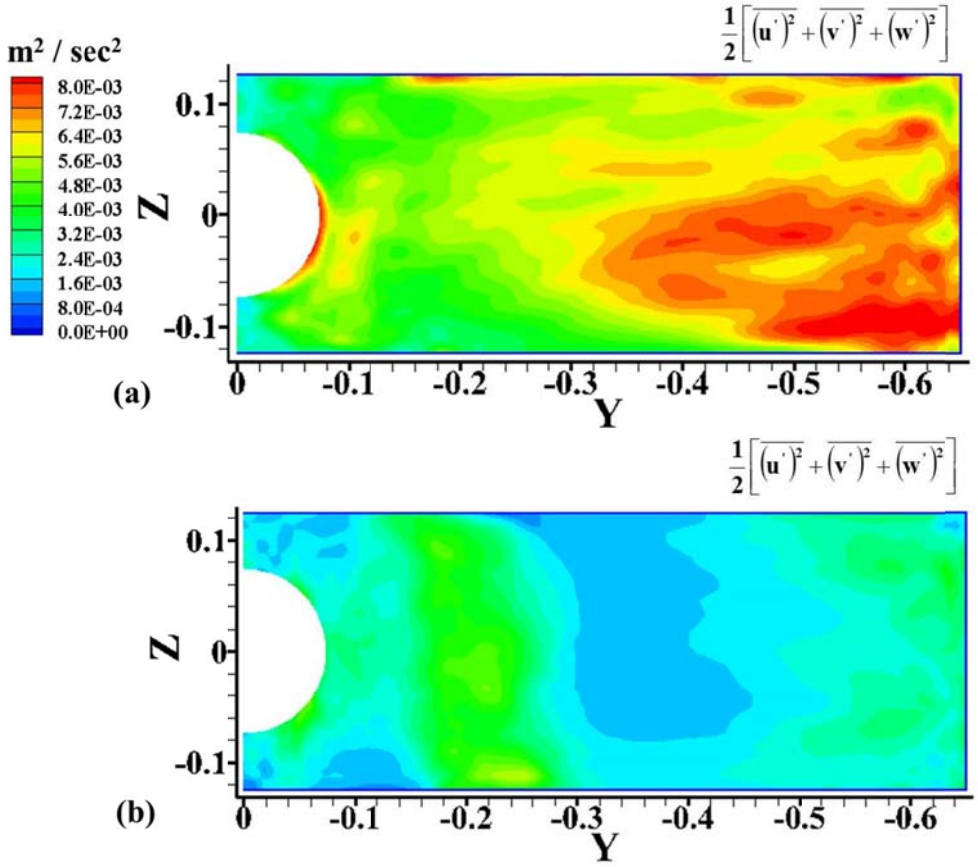

Fig.5.10. Turbulent kinetic energy contour at the surface in the mold (a) without EMBr and (b) with EMBr

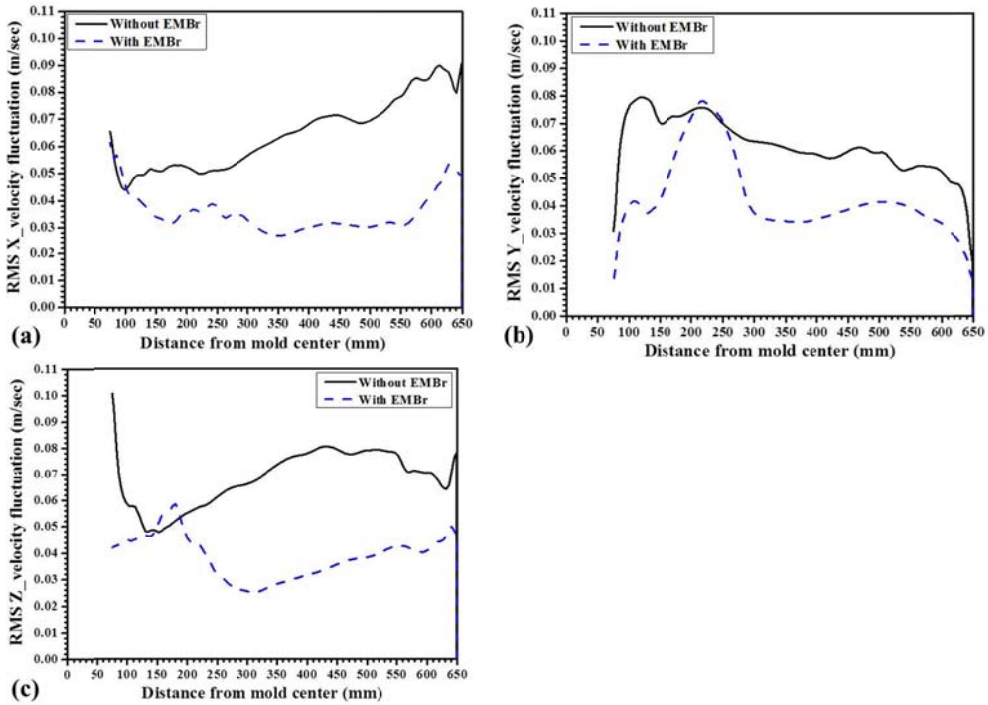

Fig.5.11. RMS velocity fluctuation profiles at the surface in the mold: (a) u', (b) v', and (c) w'

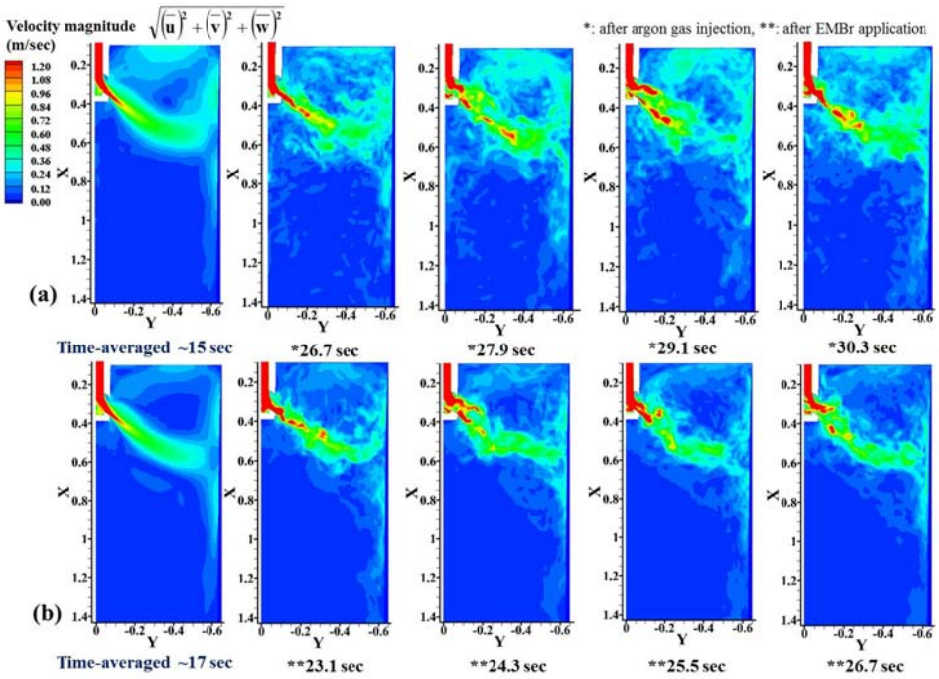

Fig.5.12. Instantaneous velocity vector in the mold (a) without EMBr and (b) with EMBr

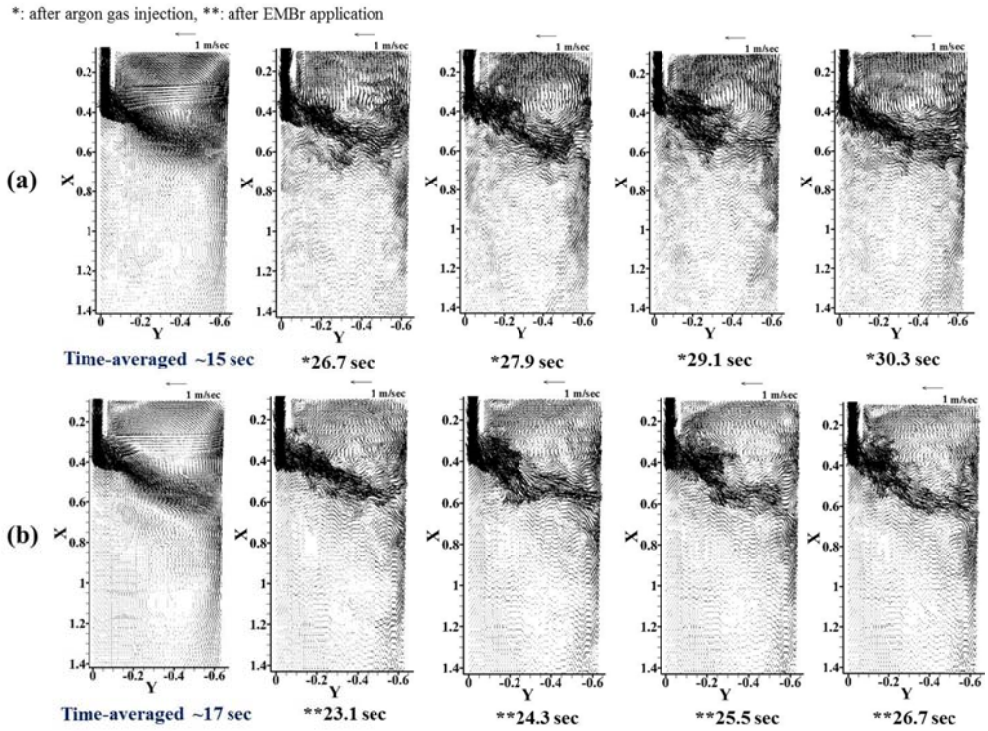

Fig.5.13. Instantaneous velocity vector in the mold (a) without EMBr and (b) with EMBr

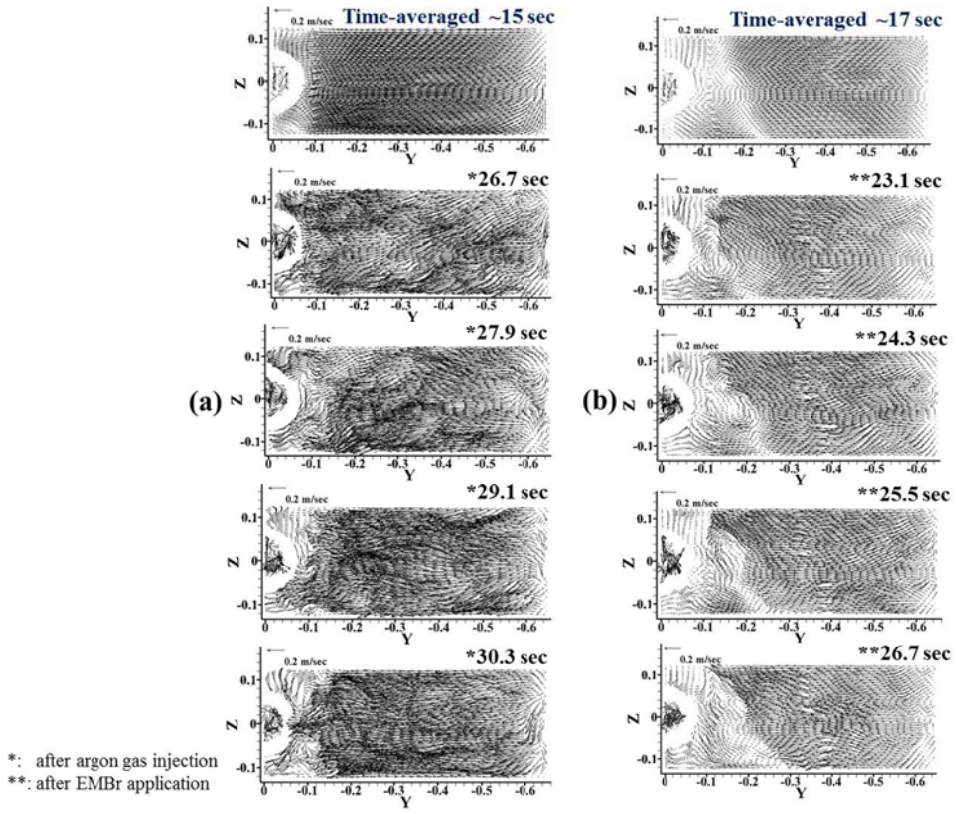

Fig.5.14. Instantaneous velocity vector at the surface (a) without EMBr and (b) with EMBr

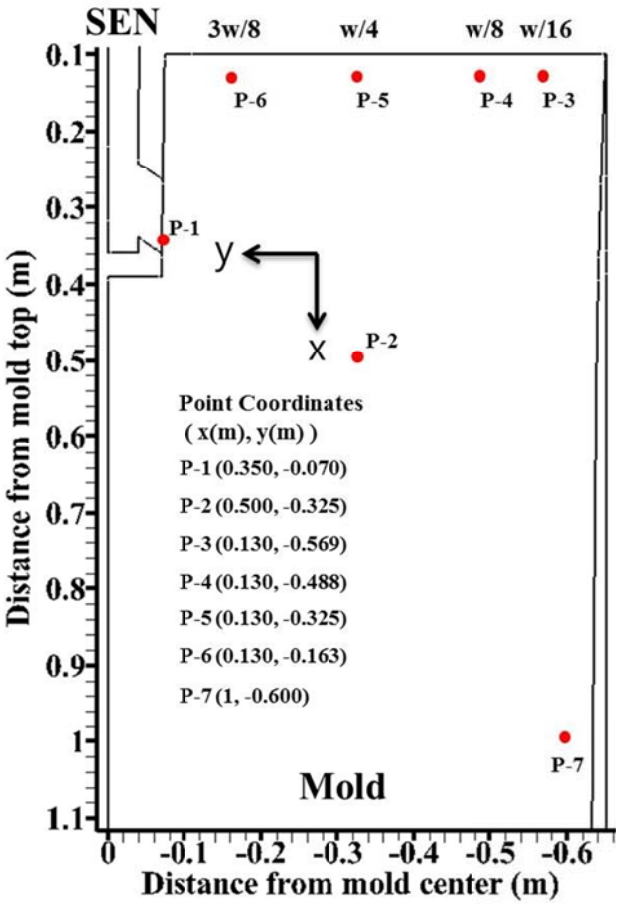

Fig.5.15. Location of points at the center-middle plane in the nozzle and mold

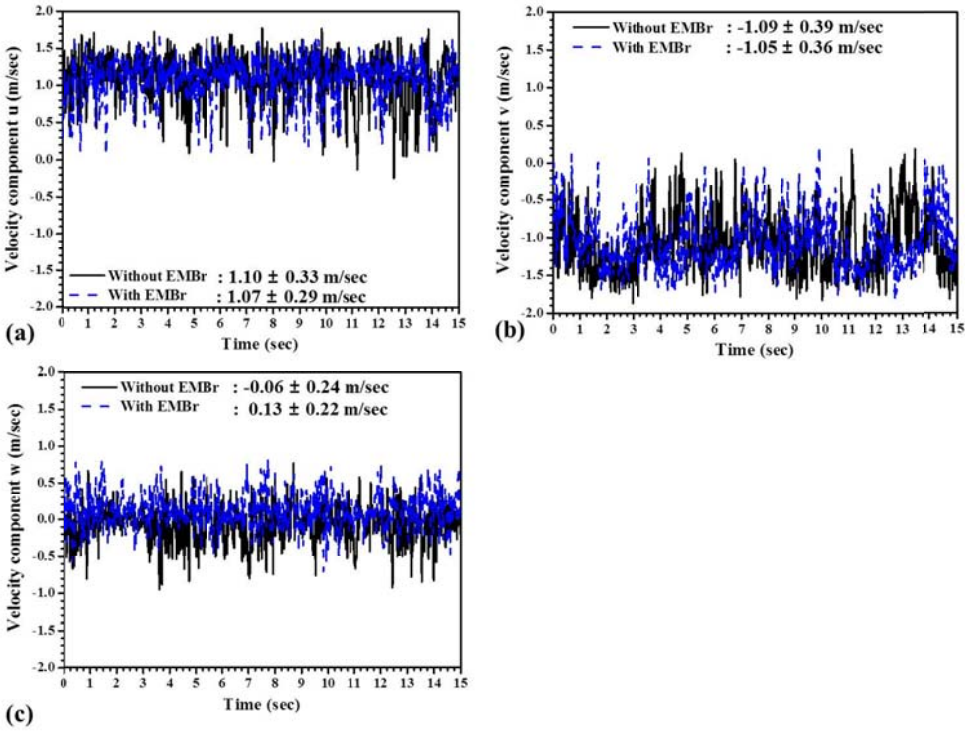

Fig.5.16. Velocity fluctuation histories during 15 sec on Point-1 in the nozzle port: (a) u, (b) v, and (c) w

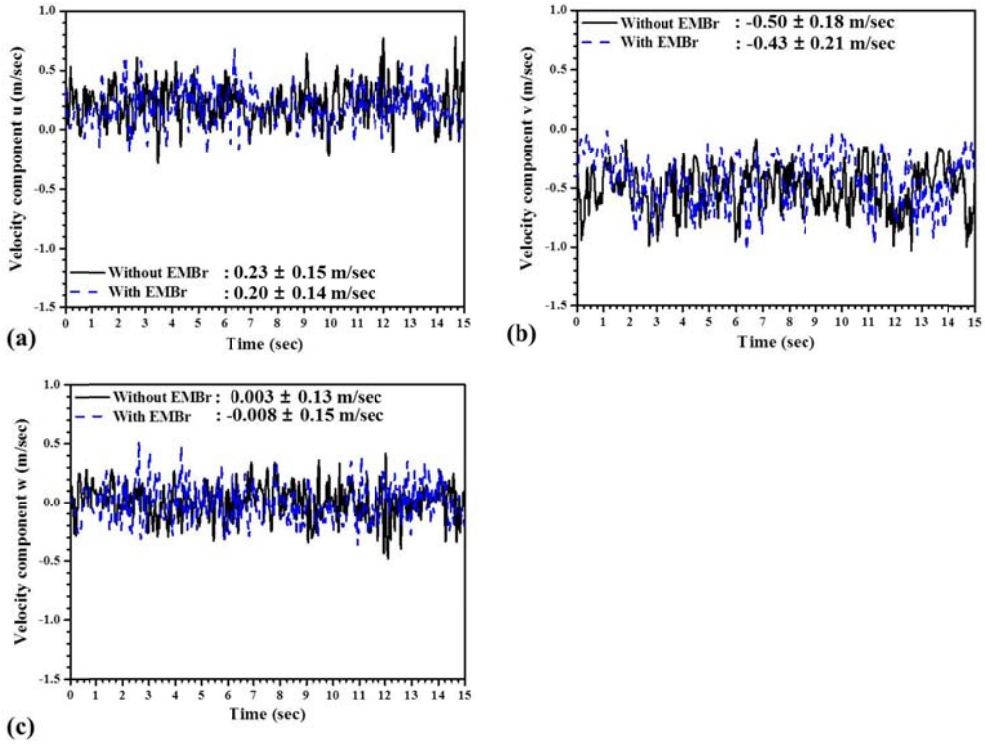

Fig.5.17. Velocity fluctuation histories during 15 sec on Point-2 in the mold: (a) u, (b) v, and (c) w

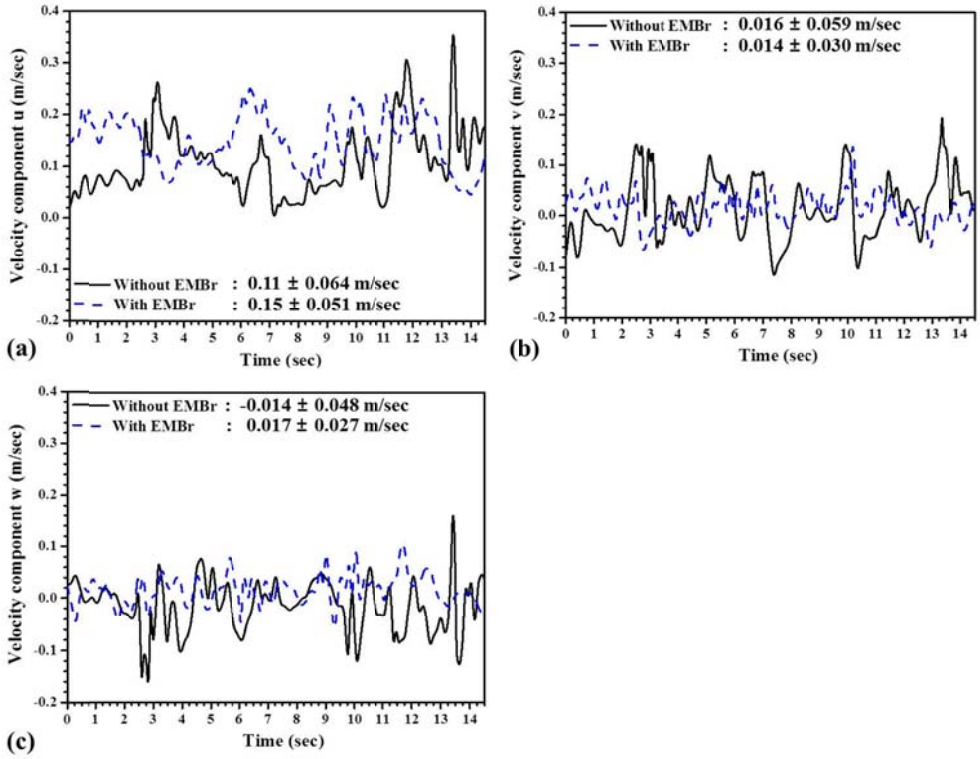

Fig.5.18. Velocity fluctuation histories during 15 sec on Point-7 in the mold: (a) u, (b) v, and (c) w

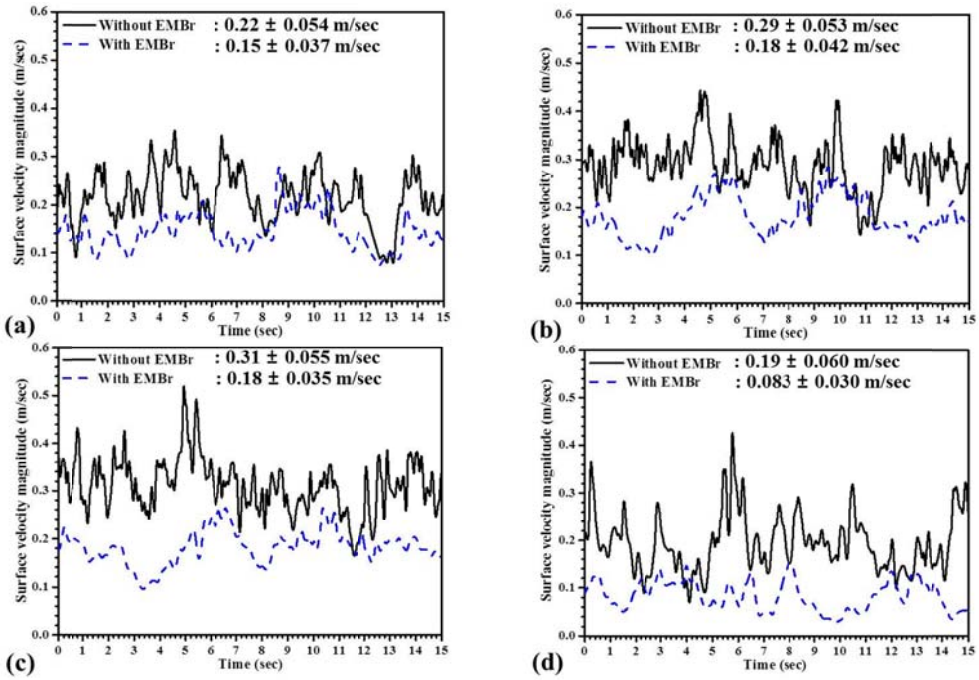

Fig.5.19. Time-variation of velocity magnitude during 15 sec at the surface: (a) P-3, (b) P-4, (c) P-5, and (d) P-6

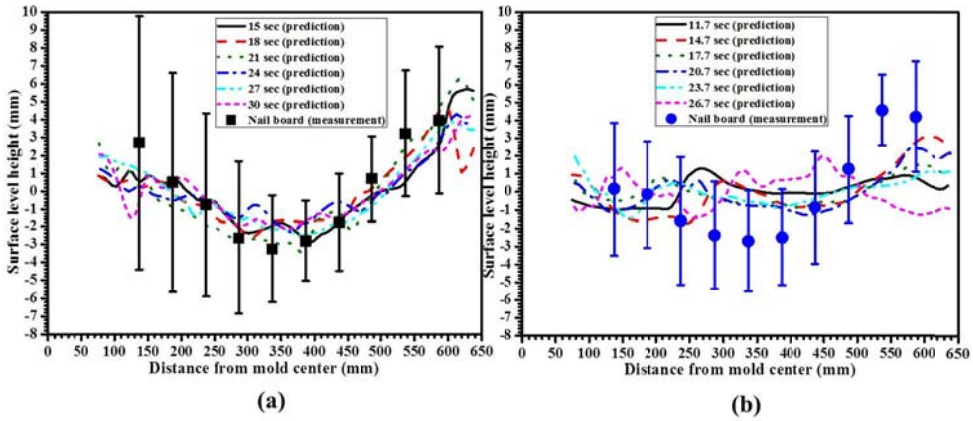

Fig.5.20. Transient surface level profile (a) without EMBr and (b) with EMBr

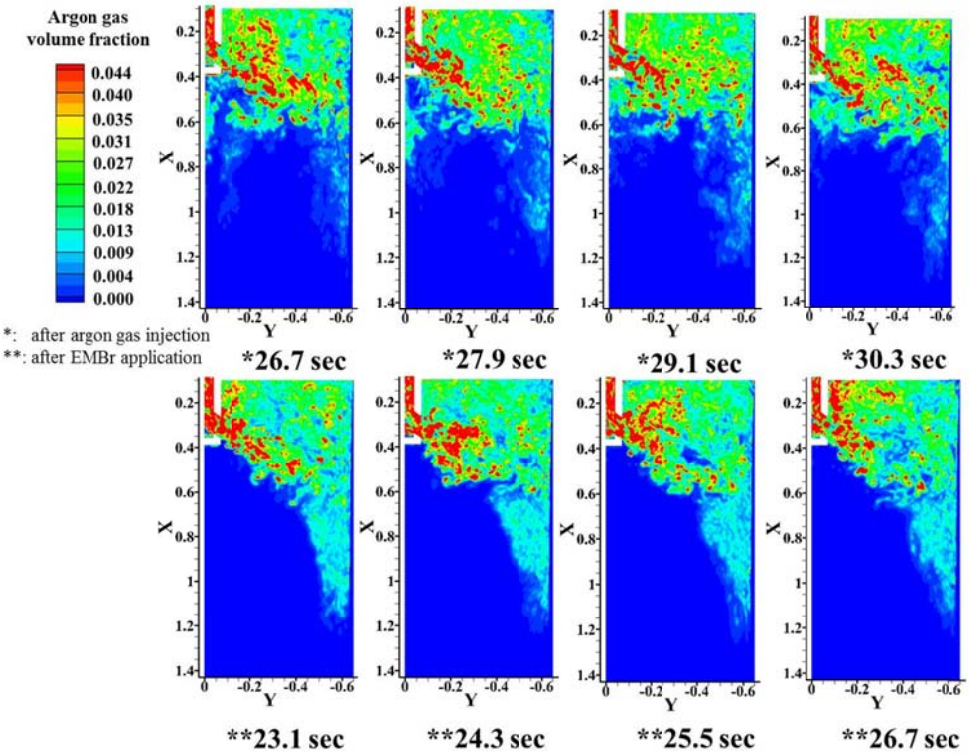

Fig.5.21. Instantaneous argon bubble distribution in the mold center-middle plane: (a) two-phase flow and (b) two-phase flow with EMBr

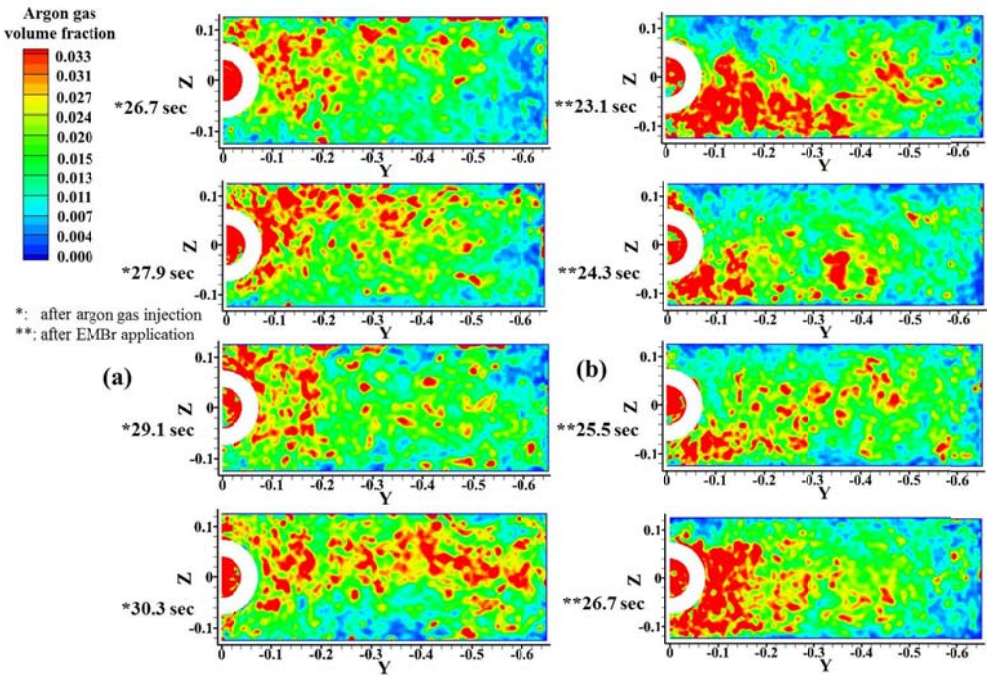

Fig.5.22. Instantaneous argon bubble distribution at the surface: (a) without EMBr and (b) with EMBr

5.9. References

1) K. Takatani, K. Nakai, T. Watanabe, and H. Nakajima: ISIJ Int, Vol. 29 (1989), 1063
2) H. Harada, T. Toh, T. Ishii, K. Kaneko, and E. Takeuchi: ISIJ Int, Vol. 41 (2001), 1236
3) Z. Qian and Y. Wu: ISIJ Int, Vol. 44 (2004), 100
4) K. Cukierski and B. G. Thomas: Metallurgical and Materials Transaction B, Vol. 39B (2008), 94
5) K. Timmel, S. Eckert, G. Gerbeth, F. Stefani, and T. Wondrak: ISIJ Int., Vol. 50 (2010), 1134
6) K. Timmel, S. Eckert, and G. Gerbeth: Metallurgical and Materials Transaction B, Vol. 42B (2010), 68
7) R. Chaudhary, B. G. Thomas, and S.P. Vanka: Metallurgical and Materials Transaction B, Vol. 43B (2012), 532
8) R. Singh, B.G. Thomas, and S.P. Vanka: Metallurgical and Materials Transaction B, in press (2013)
9) K. Moon, H. Shin, B. Kim, J. Chung, Y. Hwang, and J. Yoon: ISIJ Int, Vol. 36 (1996), S201
10) Y. Hwang, P. Cha, H. Nam, K. Moon, and J. Yoon: ISIJ Int, Vol. 37 (1997), 659
11) B. Li and F. Tsukihashi: ISIJ Int, Vol. 43 (2003), 923
12) H. Yu and M. Zhu: ISIJ Int., Vol. 48 (2008), 584

13) Y. Wang and L. Zhang: Metallurgical and Materials Transaction B, Vol. 42B (2011), 1319

14) B. Li, T. Okane, and T. Umeda: Metallurgical and Materials Transaction B, Vol. 31B (2000), 1491

15) B. Li, T. Okane, and T. Umeda: Metallurgical and Materials Transaction B, Vol. 32B (2001), 1053

16) S. Cho, H. Lee, S. Kim, R. Chaudhary, B.G. Thomas, D. Lee, Y. Kim, W. Choi, S. Kim, and H. Kim: Proc. of TMS2011, TMS, Warrendale, PA, USA, 2011, 59

17) Z. Liu, B. Li, M. Jiang, and F. Tsukihashi: ISIJ Int, Vol. 53 (2013), 484

Chapter 6: Conclusions and Future Scope

6.1. Calculation of the Initial Bubble Size of Argon Gas in the Nozzle of Continuous Steel Slab Casting

The initial bubble size of argon in molten steel in the UTN was calculated using the semi-analytical bubble formation model of Bai and Thomas, coupled with the empirical active site equation of Lee et al. The argon volume flow rate was first calculated for molten steel at high temperature and pressure. The volume flow rate in each gas pore at the refractory of the UTN was then obtained from the number of active pore sites by the empirical equation derived from the results of the 1/3 scale water model measurements. Finally, the size of the argon bubble, going through the expansion and elongation stages, was calculated using the two-stage analytical model by considering both the force balance on the bubble and the bubble elongation motion during the formation at the UTN refractory wall. The calculated initial bubble size of argon gas in the steel was used as the input data for the DPM model. The predicted bubble size by the two-stage bubble formation model, shows great agreement with the measurements obtained with the 1/3 water model employing a stopper-rod system. The model can therefore be used to predict the bubble size in future work that considers bubble behavior in the stopper nozzle.

6.2. Modeling of Transient Two-Phase Fluid Flow in the Nozzle and Mold of Continuous Steel Slab Casting & Plant Measurements

The transient molten steel flow with argon gas bubbles during steel continuous casting was investigated by applying the LES coupled with Lagrangian DPM and the nail board dipping test. The nail board dipping test captures transient surface level and velocity variations at the surface in the mold. The LES shows a very good quantitative match of the average surface profile, velocities, and their fluctuations with the nail board measurements. The surface level profile of the molten steel shows sloshing pattern with high level fluctuations near the SEN. On the other hand, surface level is the lowest with the highest stability in the quarter point region located midway between the SEN and the NF. The liquid mold flux level also varies according to the lifting force induced by the molten steel motion below. Surface flow shows a classic double-roll pattern in the mold with mostly going towards to the SEN. There is the transient asymmetric cross-flow between the IR and the OR, which mainly goes towards to the IR at the region near the OR and shows random variations (~200 % of mean horizontal velocity towards the SEN) near the IR. The surface velocity fluctuations are almost 50% of the average surface velocity magnitude across the entire mold width. This finding suggests that surface velocity fluctuations are very important to understand transient surface flow phenomena resulting in defects.

The asymmetric opening area of the middle plate of the slide-gate produces clockwise rotating flow pattern in the nozzle well. Sometimes, the small counter-

clockwise rotating flow is also induced in the nozzle well when the clockwise rotating flow becomes weak. The jet flow with up-and-down wobbling induces variations of velocity magnitude and direction at the surface and changes the jet flow impingement point on the NF. The jet wobbling also influences argon gas distribution by time in the mold.

Nozzle flow shows bigger velocity fluctuation with higher power in the well and port region. Jet flow with high velocity fluctuations becomes slower with increasing stability after impingement on the NF, resulting in slower velocity (~60 % lower) with smaller fluctuations (~70 % less) at the surface. Strong peaks are observed at several different frequencies between 0.1 and 10 Hz (0.1 to 10 sec), including several characteristic frequencies from 0.5-2 Hz (0.5-2 sec) at the nozzle port and jet core.

6.3. Effect of Double-Ruler Electro-Magnetic Braking (EMBr) on Transient Fluid Flow in the Nozzle and Mold of Continuous Steel Slab Casting

The effect of double-ruler EMBr on transient flow during steady continuous casting was quantified by applying a standard $k-\varepsilon$ model coupled with MHD equations and plant measurements using Gauss meter, eddy-current sensor and nail boards. The computational model shows reasonable agreements with the measurements for surface level profile, velocity profile, surface level fluctuations, and velocity fluctuations.

The double-ruler EMBr produces two regions of equally-strong magnetic field across the mold width: one centered just above the port and the other centered farther below the nozzle port. Strength of both peaks in the measured field significantly decreases towards the NF. With EMBr, turbulent kinetic energy of rotating swirl flow caused by the asymmetric open area at the slide-gate is decreased in the nozzle well region. Jet flow affected by electromagnetic force near NF is deflected downward, resulting in flatter surface level and slower surface velocity with less level fluctuations.

Both with and without EMBr, the surface level shows periodic sloshing variations between the SEN and the NF, as indicated by sequences of nail board dipping tests. The sloshing is high amplitude (up to 8mm) and low frequency / long period (up to 1 minute). A characteristic frequency peak of the surface level variations measured by the eddy current sensor is observed at ~0.03 Hz (~35 sec) at the "quarter point" located midway between the SEN and the NF. EMBr decreases the severe level fluctuations near the SEN by ~50%, and lowering the peaks in the level fluctuation power spectrum.

Motion of the steel-slag interface level mainly causes lifting of the slag layers, especially near the SEN. Elsewhere, the slag layers are partially displaced by the steel, due to flow that causes the liquid layer to become slightly thinner, especially near the NF, and with EMBr. The slag pool is slightly thicker with EMBr.

EMBr produced ~20 % lower surface velocities (Without EMBr: 0.22 m/sec , With EMBr: 0.18 m/sec) with ~40 % less velocity variations (Without EMBr: 0.12

m/sec , With EMBr: 0.07 m/sec). It seems that double-ruler EMBr may help to reduce defects caused by surface instability if used properly.

6.4. Modeling of Two-Phase Fluid Flow in the Nozzle and Mold of Continuous Steel Slab Casting with Electro-Magnetic Braking (EMBr)

The effect of double-ruler EMBr on transient molten steel-argon gas flow in the nozzle and mold was investigated using the LES model coupled with DPM and MHD, which was validated with the nail board measurements. This model differed from the standard $k-\varepsilon$ model studied in Chapter 4, as it could capture time variations in the flows in all directions (x: casting direction, y: mold width direction, z: mold thickness direction) in the nozzle and mold.

The double-ruler EMBr slightly decreases the velocity magnitude and turbulent kinetic energy, resulting in smaller velocity fluctuation $\sqrt{\overline{(\mathbf{u}')^2}}$ of the swirl flow (caused by the asymmetric open area at the slide-gate) along the casting direction in the nozzle well region. The EMBr deflects the jet flow downward in the mold, resulting in slower surface velocity with less fluctuation. In the upper-recirculation region of the mold, the small scale turbulence induced by transient jet wobbling is suppressed by the EMBr. The lower-recirculation zone of two-phase flow without EMBr appears to have a low frequency / long period variation, and does not show a developed flow pattern with ~15 sec averaging. With EMBr, this chaotic flow pattern

was stabilized and calmed. However, the slightly faster downward flow along the NF with EMBr could take argon bubbles and inclusions deep into the mold cavity, resulting in more internal defects. On the other hand, the smaller variation with higher frequency of the flow velocity with EMBr could be desirable for uniform solidification of the molten steel near the NF. The double-ruler EMBr studied in this work is influential for suppression of the high frequency turbulence in the mold because the magnetic field strength (maximum: ~ 0.17 Tesla) imposed by the EMBr is not sufficiently strong to reduce the low frequency variations having high power.

The results of the predicted molten steel-argon flow field with and without EMBr suggest that non-metallic inclusion defects induced by surface flow instability could be reduced by application of EMBr, which suppresses velocity fluctuations in all directions in the mold. However, with EMBr, argon gas floatation at the surface near the SEN may increase the interface (between the molten steel and the slag layers) instability, resulting in slag entrainment. Argon gas bubbles influenced by EMBr have longer residence time in the region covering 600~1200 mm from the mold top, near NF. This could increase the possibility that the bubbles can be entrapped by the solidifying steel shell beside the NF, resulting in the production of more defects in the steel slab.

6.5. Overall Conclusions

This thesis studies the effects of double-ruler EMBr on transient molten steel-argon flow phenomena which can cause defects in continuous steel slab casting. The study applies a semi-analytical model using a 1/3 scale water model of the caster, computational modeling, and plant measurements. The mean bubble size of argon gas in the molten steel in the nozzle is predicted with the semi-analytical model (the two-stage bubble formation model coupled with the bubble active site model) and validated by the water model measurements. The LES model, coupled with Lagrangian DPM considering the calculated bubble size, is then applied to predict transient flow phenomena in the nozzle and mold. The model results show good agreement with a nail board dipping test, which quantifies transient surface velocity and surface level. The model gives an insight into the surface flow instability caused by jet wobbling phenomena in the mold. The validated two-phase model is then used to investigate the effects of double-ruler EMBr on transient two-phase flow using the LES coupled with the DPM and MHD models. The model reveals that the EMBr deflects the jet flow downward deep into the mold cavity, and suppresses the small scale, high frequency turbulence, resulting in a smaller surface velocity with higher stability in the mold. From the model, argon gas distributions in the mold with and without EMBr are also quantified to figure out the possibility of defect formation in the slab.

6.6. Future Scope

The LES, coupled with DPM, for a two-phase (molten steel-argon gas) flow may be applicable for parametric studies that consider the effects of volume flow rate and bubble size of argon gas on the mold flow pattern. The LES, coupled with DPM and MHD, for two-phase flow with double-ruler EMBr may be also useful for quantifying the effects of magnetic field strength, magnetic ruler position on transient flow tendency.

In this thesis, the model predicts argon bubble distribution and the possibility of entrapment of bubbles during solidification of the steel shell. A more detailed investigation of bubble defect formation may be obtained by coupling this model with a particle capture model, such as that suggested by Thomas et al [ref. B. G. Thomas, Q. Yuan, S. Mahmood, R. Liu, and R. Chaudhary: Metallurgical and Materials Transactions B, published online, 06 Aug 2013].

The modeling method may also be adopted to quantify the effects of a moving magnetic field, such as the Electro-Magnetic Level Stabilizer (EMLS), Electro-Magnetic Level Accelerator (EMLA), and Electro-Magnetic Rotating Stirrer (EMRS), on transient fluid flow in the nozzle and mold.